SOME EXCURSIONS INTO SATURN'S FAINT RINGS

A Dissertation

Presented to the Faculty of the Graduate School

of Cornell University

in Partial Fulfillment of the Requirements for the Degree of

Doctor of Philosophy

by

Manish Agarwal

January 2014

SOME EXCURSIONS INTO SATURN'S FAINT RINGS

Manish Agarwal, Ph.D.

Cornell University 2014

Saturn's E ring: Saturn's tenuous E ring has a double-banded vertical structure, with the density of particles depleted in the equatorial plane of the rings near Enceladus' orbit. We have conducted numerical simulations, supported by order-of-magnitude analytical calculations, to investigate how particles behave in the vicinity of Enceladus' orbit to form the observed vertical structure. We also show that the the radial double-layered Gaussian core of the E-ring [Hedman et al., 2012] is formed entirely due to gravity. Saturn's gravity, including its J_2, J_4 and J_6, and effects of Enceladus are considered. The other nearby moons of Saturn are included, though our results show that they have negligible effect over the $\sim$ 200-yr integration. We follow the orbits of particles ejected near Enceladus' southern pole with speeds ranging between $\sim$ 0.8 to 2 times the nominal escape speed at the moon's surface (for an isolated spherical moon). We find that the combination of gravitational deceleration on launch plus the first few subsequent encounters with the moon causes many particles starting with 'escapable' velocities (just enough to escape gravitational influence) to assume an orbital inclination corresponding to a maximum height of $4r_E$ (r_E = radius of Enceladus), which gives rise to the double-layered structure. We present the short-term (1-2 days) and longer-term ($\sim$ 200-yr) dynamics of particles in Enceladus' vicinity. We argue that non-gravitational forces have little influence in the initial dynamics and formation of radial Gaussian core.

Ultrafaint rings: Recent Cassini images identified three tenuous rings [Hedman et al., 2009a] along the orbits of Methone, Anthe and Pallene, three small moons whose orbits nest between those of Mimas and Enceladus. A continuous inclined ring lies along Pallene's orbit, whereas the other two satellites are constrained within arcs of limited longitudinal extents. Two of the moons, Anthe and Methone, are in strong resonances with Mimas, whereas Pallene is in a weak near-resonance with Enceladus. We investigate the longitudinal confinement of material along the orbits of the three small satellites. Anthe, Methone and Pallene along with six nearby major moons of Saturn were included in numerical simulations of particles ejected from the surfaces of these three small moons. 1000 particles were integrated with a range of initial velocities from 1 - 2 m/s from the surface of the moon in all directions with respect to the moons. The particles' trajectories were integrated for 22 years. Our simulations show that differences between the first-order resonances of Anthe and Methone, and the third-order near-resonance of Pallene, may explain the confinement of material in formal cases and the lack of confinement in the Pallene ring. We confirm and identify the resonances.

BIOGRAPHICAL SKETCH

I was born in 1983, in Raibarely, UP, India. I grew up in Sultanpur, UP, India from where I did my high school. Growing up was fun as I used to be, and still am, a very curious person. Mathematics was interesting to me, and so was drawing. I used to spend a lot of time copying things on my white sheets with an aim to make them look realistic. Numbers were fun too. It was great to do algebra and finding 'x', the unknown, in the equations. I realized that the solution lied in correctly formulating the problem and how the question, if correctly understood, has half the solution. In high school, I got really fascinated by mechanics. The fact that a simple equation like 'F=ma' could represent almost everything around me, was a shock. The beauty of simplicity of physical laws made me marvel at nature. I learnt calculus while solving physics problems. Concepts of friction, rolling, energy, conservation principles totally mesmerized me.

I enrolled for a Bachelors in Mechanical Engineering at IIT Kharagpur, for the simple fact that the word 'mechanics' appeared in it. Engineering education was a great experience. It made me a problem solver. The structure it imposed upon me was frustrating at times but it made me think of solutions to problems. In my undergrad I worked on stress softening of rubber [Agarwal, 2004, Agarwal et al., 2005] and found that it was time to leave linearity and explore non-linearity. After graduating I still wanted to do more mechanics. Hence, I worked on Chaos theory for some time and analysed friction on moving belt and border collision bifurcations [Agarwal and Banerjee, 2005, Ma et al., 2006]. After some exploration, I decided to pursue a Ph.D. from Theoretical and Applied Mechanics at Cornell University, intending to do some more mechanics.

The U.S. educational system has had a very deep impact on me. I realized that you don't become what the university makes you, rather you become what you make out of the University. I took courses in numerical simulations, fluid mechanics, Dynamical Systems and Theoretical Physics to further explore the unknown. Einstein′s gravity amazed me. The only thing I did not like about that theory was the fact that it made my hero, Newton, look ordinary. But such is life - relative. I obtained a minor in theoretical Physics during the process. All along, my quest to study mechanics was alive. I met my advisor, Joseph Burns, in a class on Dynamics which he was teaching, in my first year at Cornell. The course heightened my interest to explore something further interesting in mechanics. I eventually joined Joe as a student to work on Saturn's rings. I still remember the first meeting with Joe. He showed me the side view of E ring and asked me what did I see? I saw a faint grey line running across the ring. It instantly puzzled me and became one of the subjects I worked on for my Doctorate. It has been tremendous fun and a great learning experience. Astronomy is very data intensive, but I always treated it as a mechanics problem, looking for simple reasons, simple solutions and explanations. Going to conferences was great in terms of listening and meeting some very knowledgeable people.

Apart from studies, Cornell was a great place to meet people from all around the world and get exposed to various ideas and cultures. It was an exciting time to learn with them. As a graduate student, one of my favourite jobs was teaching. I simply loved taking the tutorial classes and attending office hours. Making a student understand a hard concept and eventually looking at them smiling at their triumph gave me immense satisfaction. I, at some point in my life, want to teach at some level and re-explore the fun. Life has come a long way and so has

my understanding of the world. I have always lived in the present moment and have been lucky to have some great friends and teachers around me. I currently reside in New York City where I work for a private firm as a research analyst.

I dedicate this thesis to two very strong and inspirational women in my life - Koiri Di and Dipika.

Errata

ACKNOWLEDGEMENTS

This has been some journey! I became a mechanical engineer because I was smitten by the beauty of mechanics. I came to Theoretical and Applied Mechanics because I still wanted to do more mechanics. Newton has always been my hero after he wrote 'F=ma'. During this process of doing my research, I have been influenced by a few more special people.

Joe Burns, my advisor - this man taught me the importance of keeping things simple. I marvel at how everything in mechanics boils down to pulls, pushes and some basic motion for this man. It is a genuine art, of which he is a master. I have tried to pick up those magic skills on the way. Joe has always been a very comforting guide to me. He has motivated me in hard times and appreciated and encouraged me when others failed to do so. I thank him for all he has taught me and for all the patience he has shown during my work.

Prof. Richard Rand and Prof. Eanna Flanagan have been very kind to serve on my PhD committee. I thank them for their guidance. I have enjoyed Prof. Rand's classes a lot. I will always be thankful to Prof. Flanagan for introducing Einsteins general relativity principle to me. It was one of the most enlightening classes I have ever taken.

I would like to specially thank Mathew Hedman and Mathew Tiscareno for their invaluable suggestions throughout the course of my study. They were patient to help me and their experience and insights played a key role at various junctures of this work.

Special thanks also to Marcia, Cindy and Polly for their kind help whenever it was needed. Kind regard also to Cornell Graduate School office and the international Students office for helping out with various administrative requirements at various points. Thanks to every teacher, TA and class-mates who helped me out with various courses and projects at Cornell.

I would also like to thank everybody who helped me with the editing work - Jenny particularly. I thank my friends - David, Ajeet, Sarabjeet and Anoop for some of the most amazing and thought provoking times I have had at Cornell. Special thanks to all my friends at Cornell who made my social stay in Ithaca such a delight. This has been some journey and it continues!

ACKNOWLEDGEMENTS

This has been some journey! I became a mechanical engineer because I was smitten by the beauty of mechanics. I came to Theoretical and Applied Mechanics because I still wanted to do more mechanics. Newton has always been my hero after he wrote 'F=ma'. During this process of doing my research, I have been influenced by a few more special people.

Joe Burns, my advisor - this man taught me the importance of keeping things simple. I marvel at how everything in mechanics boils down to pulls, pushes and some basic motion for this man. It is a genuine art, of which he is a master. I have tried to pick up those magic skills on the way. Joe has always been a very comforting guide to me. He has motivated me in hard times and appreciated and encouraged me when others failed to do so. I thank him for all he has taught me and for all the patience he has shown during my work.

Prof. Richard Rand and Prof. Eanna Flanagan have been very kind to sever on my PhD committee. I thank them for their guidance. I have enjoyed Prof. Rand's classes a lot. I will always be thankful to Prof. Flanagan for introducing Einsteins general relativity principle to me. It was one of the most enlightening classes I have ever taken.

I would also like to thank everybody who helped me with the editing work - Jenny particularly. I thank my friends - David, Ajeet, Sarabjeet and Anoop for some of the most amazing and thought provoking times I have had at Cornell. Special thanks to all my friends at Cornell who made my social stay in Ithaca such a delight. This has been some journey and it continues!

TABLE OF CONTENTS

LIST OF FIGURES

LIST OF TABLES

CHAPTER 1

SATURN'S FAINT RINGS

Saturn's rings have been a source of amazement since Galileo discovered them in 1610. Their existence as flat rings was established only in 1655 by Christiaan Huygens. In 1675, Giovanni Cassini determined that these rings contained at least one gap amidst them. In 1787, Laplace further suggested that the rings were composed of a large number of solid ringlets. It took until 1859 before the notion that the ring was made out of small particles (rather than being solid) became the accepted theory [Maxwell, 1859]; this was observationally confirmed by Keeler [1895].

Several space missions explored the ring bearer, Saturn, the nearby satellites and the rings themselves. Since 2004 the Cassini spacecraft has provided a plethora of information about Saturn's ring system. Previous knowledge from the Pioneer and Voyager missions has been confirmed and much more has been established. Ground-based observations, along with Hubble telescope images, have added to ring data. Table 1 summarizes the various missions attempted.

Mission	Launch date	Arrival date	Type
Pioneer 11	Apr, 1973	Sep, 1979	Flyby
Voyager 1	Sep, 1977	Nov, 1980	Flyby
Voyager 2	Aug, 1977	Aug, 1981	Flyby
Cassini	Oct, 1997	July, 2004	Orbiter

Table 1.1: Various missions to Saturn

Cassini is the only spacecraft to orbit Saturn. Different sensors (see "Space Science Reviews" issue on Cassini's instrumentation, Volume 114, Numbers 1-4, September 2004) on the spacecraft collect data at various wavelengths and transmit them

to ground-based receiving stations. The findings of the Cassini's first four years in orbit are compiled in the book, "Saturn from Cassini-Huygens" [Dougherty et al., 2009].

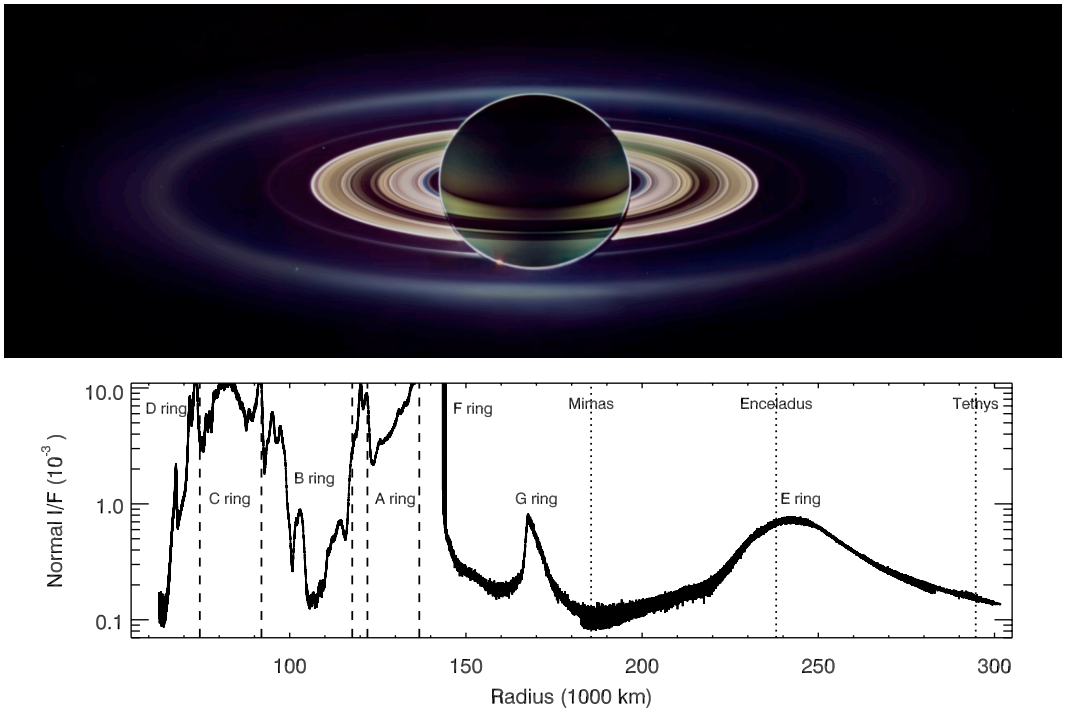

Figure 1.1: *Top*: A mosaic of images taken on September 15, 2006, while Cassini was in the shadow of Saturn (image PIA08329; these numbers identify a NASA press release image). In this geometry, the small particles that mostly comprise the faint rings forward-scatter light very efficiently, so these normally faint rings appear especially bright. *Bottom*: The brightness of the rings as a function of radial distance from Saturn for a constant phase angle of 178.5^o as observed through the camera's clear filter (central wavelength of 635 nm); Saturn (radius of 60,330 km) would lie just off the left side of this diagram. Brightness is plotted in terms of the quantity normal I/F, which is proportional to the fraction of the incoming solar radiation scattered into the camera by the material [Horányi et al., 2009]. For rings of low optical depth, the back-scattered I/F is also similar to the normal optical depth of the ring. Dotted lines are the radial positions of prominent Saturnian moons, while the dashed lines show the inner and outer extend of the bright A, B and C rings of Saturn.

The main rings, A, B and C, have been under the spotlight because of their easier visibility. This chapter will instead survey the fainter rings of Saturn [Burns

et al., 2001, Horányi et al., 2009]. These include: the D ring, the F ring, the Janus/Epimetheus ring, the G ring, the Methone ring arc, the Anthe ring arc, the E ring, the Pallene ring and the Phoebe ring; the positions of these are found in Fig 1.1 (bottom). The main rings also have some dust, primarily the 'spokes' found in the B ring. Since collisions are virtually non-existent in faint rings, the constituent particles act as individual satellites of Saturn. However, most of the faint rings are linked with one or several Saturnian moons, either through resonance [Hedman et al., 2007b], "shepherding" [Murray et al., 2005] or sometimes even feeding them [Porco et al., 2006]. Particles (primarily less than 100 microns in size) in these faint rings interact with the neighboring moons. In addition, owing to their small particle sizes, the faint rings exhibit extremely interesting dynamics and structure due to the wide range of forces these particles are subjected to, including gravitational, electromagnetic and radiation forces. Also, a knowledge of the distribution of such particles helps to plan safer routes for present and future spacecraft. Figure 1.1 gives a bird's-eye view of all the faint rings of Saturn and Table 1.2 briefly summarizes the rings under consideration.

1.1 The D ring

The D ring is the innermost of all the rings of Saturn and, being very near to Saturn, resides in the region where the planetary magnetic field is more important than elsewhere within the ring system [Hedman et al., 2007a, 2011]. The D ring is also close to a newly discovered radiation belt [Krimigis et al., 2005]. Hence, particles in the D ring are subject to an extreme environment.

Figure 1.2 compares the views of the D ring as seen by Voyager 1 and 25 years

Name	Normal Optical Depth	Related Moons	Radial location(km)
D ring	$10^{-4} - 10^{-3}$		65,000-74,500
Maxwell Gap ringlet	10^{-4}		87,420
B ring spokes	$10^{-2} - 10^{-1}$		100,000-117,500
Huygens Gap ringlet	10^{-4}		117,490
Charming ringlet	10^{-3}		119,940
Encke Gap ringlets	10^{-3}	Pan	133,490-133,720
Roche Division	10^{-4}		136,800-139,500
F ring	$10^{-2} - 10^{-1}$	Prometheus/ Pandora	139,500-141,000
J/E ring	10^{-7}	Janus/ Epimetheus	151,450
G ring	10^{-6}	Mimas	165,000-175,000
Methone Ring Arc	10^{-7}	Mimas	194,230
Anthe Ring Arc	10^{-7}	Mimas	197,650
Pallene ring	10^{-7}	Enceladus	212,280
E ring	10^{-5} (Peak)	Enceladus	180,000-700,000
Phoebe Ring	$10^{-7} - 10^{-8}$	Phoebe	4,000,000-13,000,000

Table 1.2: Various faint rings of Saturn and their properties (Table 16.1, p. 513, in Horányi et al. [2009] and Verbiscer et al. [2009])

later by Cassini. Three bright sub-rings, called D68, D72 and D73 were visible in Voyager's observations [Showalter, 1996]. However, D72, which was brighter in the Voyager image, appears to be broader and fainter in the Cassini image. Its center of light has also shifted substantially inwards, relative to the other D-ring features [Hedman et al., 2007a, 2011]. These are some of the largest secular changes in the entire Saturn ring system observed so far. There is also a possibility that the D72 feature has completely vanished and what we see in the Cassini image is a new entity altogether. The photometric properties of the diffuse material interior to

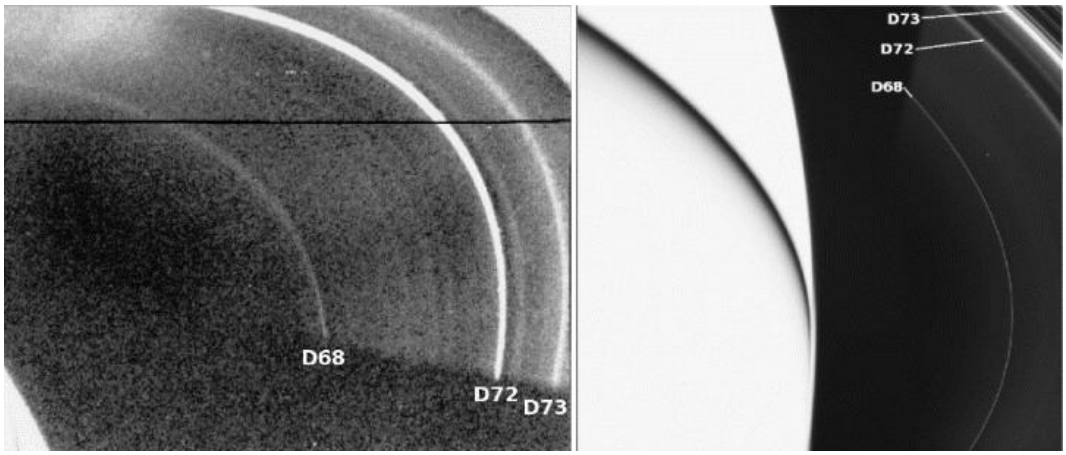

Figure 1.2: D ring (Left) Voyager 1 image (34946.50) taken at a phase angle of 156^o. The three brightest bands were called D68, D72 and D73. The horizontal black line is a data drop-out. (Right) The same region imaged by Cassini (W1500088644), at a phase angle of 171^o; an over-exposed Saturn fills the image's left half [Hedman et al., 2007a].

D72 are consistent with a population of small particles. These grains may have been derived from D72 and then spiralled inward towards the planet under the influence of Poynting-Robertson or other drag forces [Burns et al., 2001]. The Cassini data also indicate that the peaks of all three sub-rings have moved from the previously reported Voyager observations. The shifts are +70, -150 and +120 km, respectively. All three ringlets have, therefore, apparently moved relative to each other during the last twenty-five years.

Voyager observations also detected a diffuse sheet of material between D68 and D73, which has quasi-sinusoidal brightness variations with a typical wavelength of $\sim$ 500 km. Cassini images show the same but with the periodic brightness oscillations much more muted. The region surrounding D73 is more complex. Between D73 and the inner C ring lies a sheet of material with a series of dips, or notches. The $\sim$ 30-km pattern can be understood as produced by vertical corrugations in the ring material. Figure 2.33 shows how changes in the local slope of a warped

ring lead to differences in the amount of material seen along different lines of sight. This explains the observations in the outer part of the D ring [Hedman et al., 2007a].

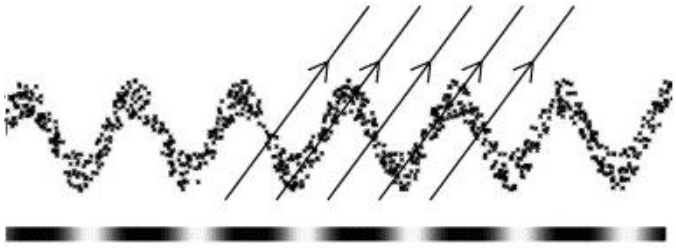

Figure 1.3: A vertical corrugation in a diaphanous ring can give rise to brightness variations. The diagonal lines correspond to lines of sight through the corrugated ring. The gray-scale at the bottom shows the ring's total optical depth and brightness as they would be seen by an observer [Hedman et al., 2007a].

The most remarkable thing about this periodic structure is that it is not a static feature, but has instead undergone significant evolution over the last decade. This can be explained assuming that it was initially a flat inclined sheet that is undergoing spiral winding [Hedman et al., 2007a, 2011] due to the planet's oblateness. Finally, if this process is extrapolated backward in time to unwind the spiral, it suggests that the ring was flat in June 1983 at which time some type of disruption occurred across the D ring. Hedman et al. [2007a, 2011] suggest that a comet-cloud might have collided with the inner ring system.

1.2 The F ring

Discovered by Pioneer 11 [Gehrels et al., 1980], the F ring is Saturn's outermost narrow ring and its most active ring; it changes on a time-scale of hours [Murray et al., 2008]. The ring is located 3000 km beyond the outer edge of the A ring and

is just a few hundred kilometers wide. The ring seems to be comprised of three to four separate, but possibly intertwined, strands of material [Charnoz et al., 2005, Charnoz, 2009, Murray et al., 2008, Beurle et al., 2010], confined radially by two nearby small satellites, Prometheus and Pandora (Figs. 1.4 - 1.6), which orbit interior and exterior to it [Colwell et al., 2009].

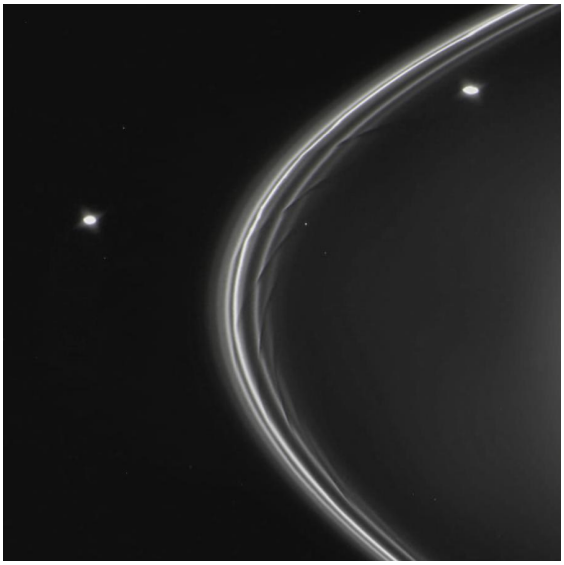

Figure 1.4: The F ring being shepherded by Prometheus and Pandora as shown in Cassini image PIA07712.

If the distance of the moon from the ring is taken as x, it can be proven that the moon initiates a wave of wavelength $\lambda = 3\pi x$ [Dermott, 1981] (Fig. 1.6). Thus the perturbations of Prometheus, and also those of the smaller and more distant Pandora, are imprinted on the F ring [Kolvoord et al., 1990, Colwell et al., 2009]. Showalter and Burns [1982], Borderies and Goldreich [1983], Kolvoord et al. [1990] and Murray and Giuliatti-Winter [1996] have shown that the moon creates periodic features via simple gravitational pulls. The perturbing effect of Prometheus also seems to introduce channels through the F ring and a "streamer" - a line of

Figure 1.5: Multi-banded F ring with the braided structure (Image PIA06143). Prometheus is shown to the left.

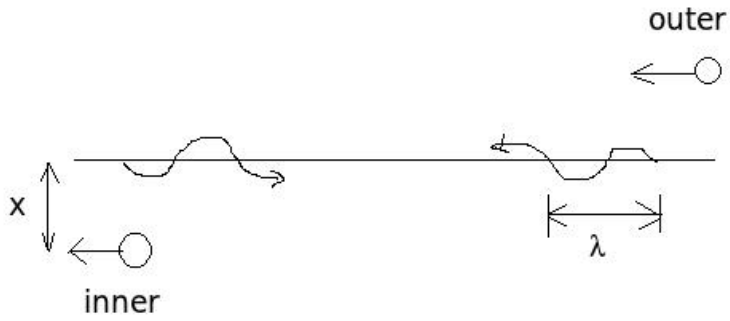

Figure 1.6: Schematic showing the perturbing effect on a narrow ring by two small satellites as viewed in the frame of each satellite.

particles that link the ring to the satellite. The moon makes regular forays into the inner dusty edge of the F ring with each 14.7 hours orbit around Saturn [Murray et al., 2005]. Beurle et al. [2010] and Murray et al. [2008] show that when Prometheus encounters the ring at its apoapsis, its gravitational attraction creates kinks and knots in the F ring as the moon 'steals' material from it, leaving a dark channel in the inner part of the ring. Since Prometheus orbits Saturn more rapidly than the material in the F ring, each new channel is carved about 3.2 degrees (the synodic drift during one orbit) in front of the previous one. The periodic spacing

of these features fits the wavelength prediction of $\lambda = 3\pi x$. Beurle et al. [2010] and Murray et al. [2008] further suggested that small unseen moons orbiting within the F Ring are continually passing through its narrow core, because of the perturbations from Prometheus.

Another interesting structure in the F ring is its spirally wound geometry (Fig. 1.7). Charnoz [2009] shows that dissipative physical collisions of kilometer-size moonlets (or clumps) with the F-ring core is a viable and efficient mechanism for producing spirals and jets, provided that massive moonlets are embedded in the F-ring core [Murray et al., 2008, Beurle et al., 2010] and that they are impacted by loose clumps orbiting in the F-ring region. They also show that coefficients of restitution as low as $\sim$0.1 are needed to reproduce the radial extent of the visible spirals and jets, suggesting that collisions are very dissipative in the F-ring region.

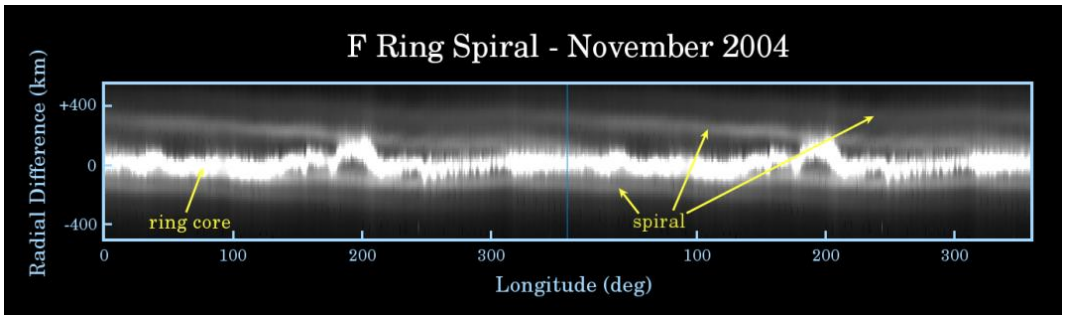

Figure 1.7: Spiral of the F ring running around Saturn (image PIA07717). This shows more than the full circumference of the ring, straightened out to make features visible.

1.3 The G ring

The G ring is a very thin, faint ring about halfway between the F ring and the inner edge of the E ring (Fig. 1.1). Cassini obtained its most comprehensive view of the G ring in Sep 2006 revealing a localized brightness enhancement near the ring's inner edge around 167,500 km from Saturn's center (Fig. 1.8). This feature extends across $\sim 60^o$ in longitude and has a radial full width at half-maximum of $\sim$250 km, much less than the $\sim$6000 km radial extent of the entire G ring. More images have demonstrated that it is a persistent feature of the ring. Hedman et al. [2007b, 2010] found the half-km diameter moonlet Aegaeon in this arc, that is held in place by a 7:6 co-rotation eccentricity resonance with Mimas. The particles in the arc are also in the same resonance with Mimas [Hedman et al., 2007b, 2010], producing a longitudinally confined structure $\sim 60^o$ wide.

During one of Cassini's passages a strong, $\sim$ 50% depletion in the energetic electrons was detected (Fig. 1.9). Such a deep depletion was not present in previous passages near the G ring [van Allen, 1983], implying that the absorption was due to large particles trapped in the arc [Hedman et al., 2007b]. The G-ring's absorption is displaced radially (Fig. 1.9) [Thomsen and van Allen, 1980, Roussos et al., 2007]. The magnitude of the absorption indicates that the arc contains a total mass between 10^8 and 10^{10} kg, equivalent to a 100-meter-wide ice-rock moonlet [Hedman et al., 2007b]. Given the breadth of the absorption feature observed, and the fact that the cross-section of this object is much less than the total cross-section of large particles computed by van Allen [1987], it is unlikely that Aegaeon is the only absorbing object in the G-ring arc. Hence other particles between 1 and 100 m in diameter reside in the arc, with the rest of the G ring consisting of dust released from within the arc [Hedman et al., 2007b].

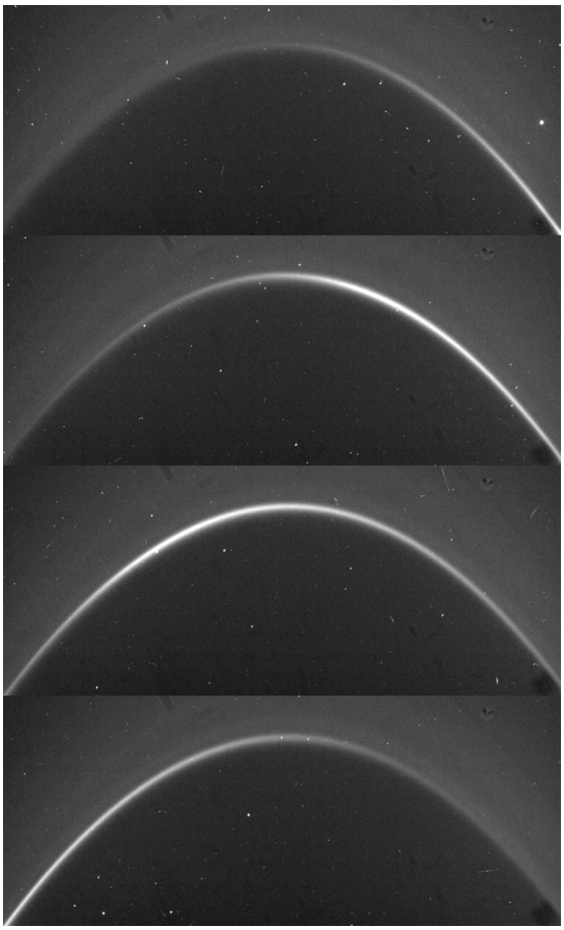

Figure 1.8: Images of the G-ring arc obtained by Cassini (N1537362584 through N1537431998 at phase angle 162.5^o and ring opening angle of 10^o, radial resolution of 15 km/pixel). Images were obtained on 19 September 2006 at 12:37, 13:11, 13:44 and 14:18 UTC (from top to bottom). A bright arc moves from right to left through the field of view [Hedman et al., 2007b].

The G ring's radial structure can be explained by dust released by micro-meteoroid impacts into Aegaeon and other source bodies within the arc which then drifts outward from the arc because of interaction with Saturn's magnetosphere (whose plasma corotates with Saturn's magnetic field, i.e., more rapidly than the orbital motion of the G ring's particles [Burns et al., 2001]). These tiny ejecta are steadily eroded away by further impacts and dispersed outward by plasma drag. Over the course of thousands of years, the ring gradually loses mass, which is replenished

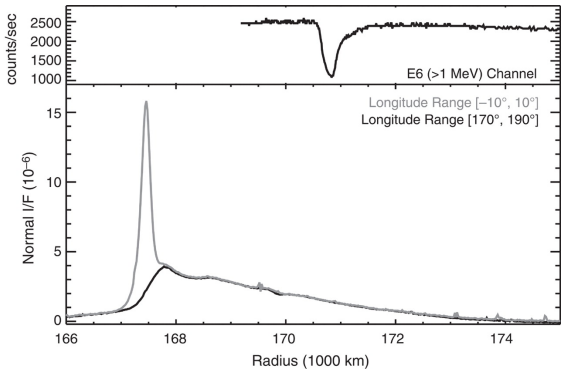

Figure 1.9: (Top) The charged-particle flux detected during Cassini's passage over the arc region. The radial scale here corresponds to the equatorial distance of the unperturbed magnetic field lines that threaded Cassini at the time of the observation [Hedman et al., 2007b]. (Bottom) Average (offset-subtracted) radial brightness profiles of the G ring at different longitudes relative to the arc's peak. The profiles through the arc (gray) and elsewhere (black) are essentially identical outside 168,000 km, whereas the arc is the sharp peak at 167,500 km in the gray profile. The absorption feature's radial width is comparable to the visible arc's. The 3000-km radial offset between the two signatures may be caused by magnetospheric effects [Hedman et al., 2007b].

by further impacts into Aegaeon.

1.4 The Janus/Epimetheus ring

Figure 1.10 shows the faint dust ring present around the region occupied by the orbits of the co-orbital satellites Janus and Epimetheus. The ring has a radial extent of about 5,000 km. Williams and Murray [2011] describe an analytical model for the evolution of ring particles that are co-orbital with the two larger bodies. They show numerically and analytically that the ring associated with Janus and Epimetheus must be continually fed with material, probably by meteoroid impacts on the two satellites.

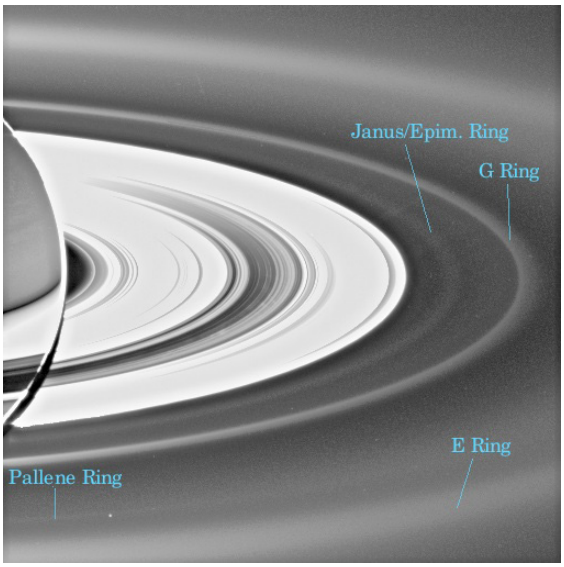

Figure 1.10: The outer faint rings seen back-illuminated by the Sun, showing the Janus/Epimetheus and Pallene rings (Image PIA08322).

1.5 The Anthe and Methone arcs and Pallene ring

Cassini images identified tenuous arcs [Hedman et al., 2009a] along the orbits of Methone and Anthe and a ring surrounding the orbit of Pallene. The resonances of Anthe and Methone with Mimas are first-order, which may explain the longitudinal confinement of material in the Anthe and Methone arcs [Cooper et al., 2008, Spitale et al., 2006]. We analyze these arcs in Ch. 4, where the images of these features and subsequent analysis will be found. Figure 1.10 also shows a faint dust ring sharing Pallene's orbit. The ring has a radial extent of about ∼100 km at medium phase angles and about ∼2500 km at higher phases [Hedman et al., 2009a]. As we discuss in Ch. 4, Pallene is near a third-order resonance with Enceladus.

1.6 The E ring

Saturn's tenuous E ring commences abruptly at 3 Saturn radii, to peak sharply near the orbit of the satellite Enceladus (at about 4 Saturn radii), orbiting between Mimas and Tethys (Fig. 1.11); it then spreads out thinly to beyond 8 Saturn radii [Horányi et al., 2009]. A narrow distribution of slightly non-spherical particles of radius 1.0 (± 0.3) μm provides a good fit to the ground-based and spacecraft imaging observations [Showalter et al., 1991]. In-situ detectors (Horányi et al. [2009]; S. Kempf, private communications, 2011; Hedman et al. [2012]) implicate more small particles. This highly peculiar size distribution clearly indicates that the ring does not originate from collisional or disruptive processes, and is therefore unlike any other ring. Hence, strong credence can be given to the possibility that the ring is associated with Enceladus and that it is the material ejected from Enceladus [Baum et al., 1981, Porco et al., 2006].

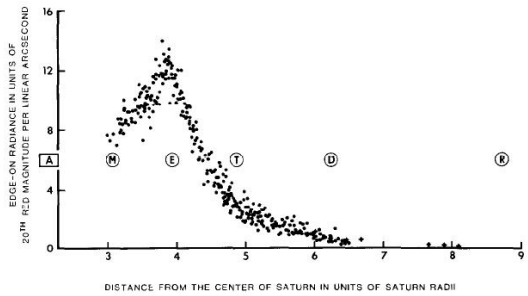

Figure 1.11: Mean edge-on brightness profile of the E ring in March 1980. Orbital radii of the A ring, Mimas, Enceladus, Tethys, Dione, and Rhea are included [Baum et al., 1981].

Earlier images taken by the Voyager space probe revealed that Enceladus' surface is icy; somewhat cratered and complex [Smith et al., 1982]. Cassini flybys detected a faint localized atmosphere around Enceladus distorting Saturn's magnetic field

lines [Dougherty et al., 2006]. Data have also confirmed a surface dominated by water, with simple organics and carbon-dioxide along with fractures seen across the satellite's southern hemisphere [Porco et al., 2006, Brown et al., 2006]. Flybys also revealed that the southern polar regions are generally free of impact craters, and therefore recently resurfaced [Porco et al., 2006]. But several prominent, ∼130 km long fractures, called "tiger stripes," were seen in the neighborhood of the South pole. This and subsequent encounters produced confirming evidence of plumes of water vapor and small ice particles spewing from the South pole [Porco et al., 2006, Hedman et al., 2009b]. These images show that many narrow jets of fine icy particles emanate from the south polar terrain (SPT) and feed large plumes towering over the south polar region by at least 435 km [Porco et al., 2006](Fig. 1.12). The interior of the SPT is characterized by a complex network of cross-cutting fractures. The ISS broadband spectra of the surface indicate the presence of pure water ice particles with a characteristic size of a few microns. Enceladus' bright surface is thought to be a direct outcome of a covering of fine-grained snow that has fallen out of the plume, then accumulated over time as a result of impact comminution by high-velocity E-ring particles [Porco et al., 2006]. Observing these plumes at high, rather than low, phase angles indicates that they consist of fine, forward-scattering particles [Porco et al., 2006, Hedman et al., 2009b].

Having accepted that these plumes feed the E ring, we come to the dynamics of the ring particles. The ring's side view (Fig. 1.13) shows a faint grey line running through the equatorial plane, indicating a double-layered structure, in which fewer particles lie at the equator than on either side. This thesis suggests a possible explanation for the origin of this double-banded structure (Ch. 2).

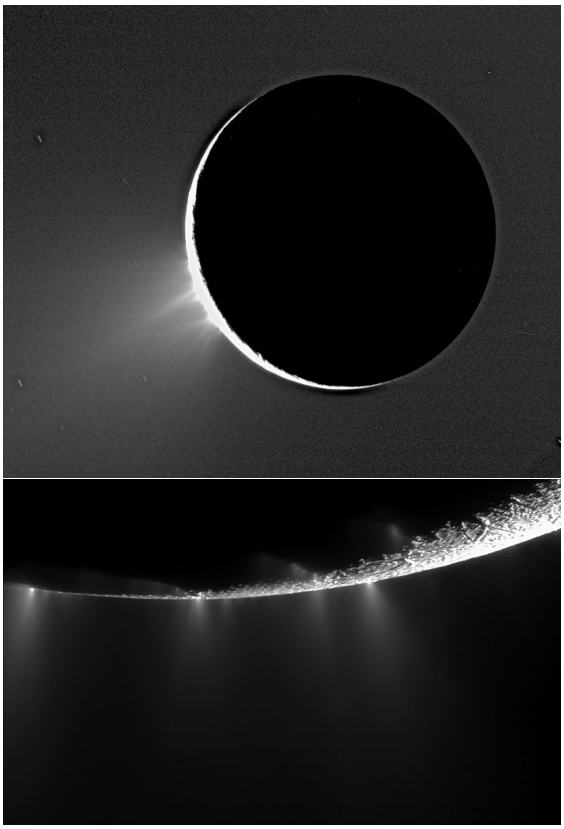

Figure 1.12: Plumes of ice particles and water vapor emanating from the South pole of Enceladus (top: image PIA07758 bottom: image PIA11688). These images are rotated slightly relative to one another.

In addition to Saturn's gravity field (including its oblateness) and nearby moons, electromagnetic forces, plasma drag, and solar radiation pressure also play a role in the evolution of the small ring particles [Horanyi et al., 1992]. Over long times, these non-gravitational forces cause the micron-sized particles to spread significantly radially. Highly eccentric orbits allow collisions with nearby moons and produce further ejecta [Hamilton and Burns, 1994]. Juhász and Horányi [2004] analyticaly explored the seasonal variations in the density and spatial distribution of dust in Saturn's E ring. Using Cassini data, Horányi et al. [2008] further investigated the radial extent of the E ring. The Gaussian core of the double-layered ring extends radially about 30,000 km around Enceladus [Hedman et al., 2012].

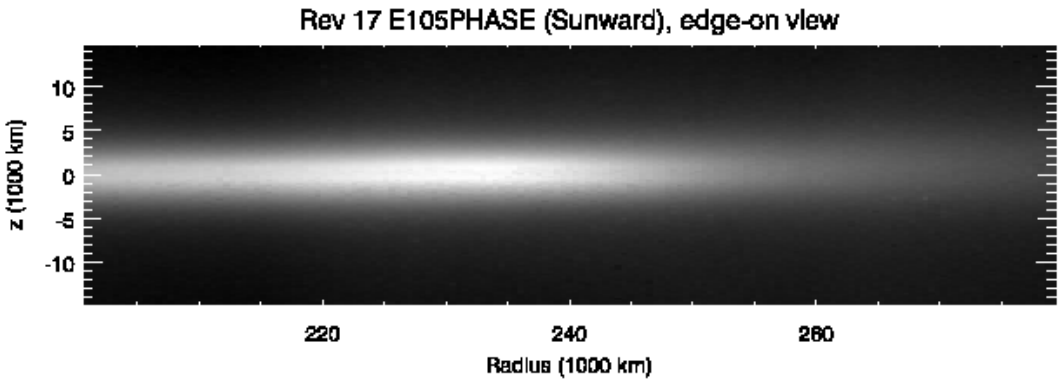

Figure 1.13: Edge-on view of Saturn's E ring at a phase angle of 105^o showing the double-layered vertical structure (Image PIA07803). The faint grey line bifurcating the ring at the equatorial plane (z $\sim$ 0, 205,000 km to 250,000 km) indicates a relative scarcity of particles in the equatorial region. The vertical distance between the two layers is about $\sim$ 2000 km. See Fig. 2.1.

Kempf et al. [2008, 2010] studied the dynamics of E-ring particles just as they leave Enceladus using dust impact data and simulations under gravitational and non-gravitational forces. Their simulations show that particles with sizes greater than $0.7\mu m$ can escape to the E ring only if their initial speeds are higher than 207 m/sec. Tiny particles are scarcely affected by the moon's gravity but instead are dragged by Saturn's rotating magnetic field. The effective escape speed of a jet particle depends on its size as well as location [Kempf et al., 2010]. Kempf et al. [2010] also describe the gradual loss of the imprint of the plume in the long-term dynamical evolution of E-ring grains. The short-term and moderate-term dynamics of E-ring particles near Enceladus' orbit under gravitational forces are further explored in Ch. 2.

1.7 Phoebe Ring

The Phoebe ring is a tenuous disk of material just interior to Phoebe's orbit at 215 Saturn radii [Verbiscer et al., 2009]. Observations [Verbiscer et al., 2009] indicate that the ring extends inwards from $\sim$ 200 Saturn radii and calculations suggest that it halts at the orbit of Iapetus at 59 Saturn radii [Tamayo et al., 2011]. Since it is symmetric about Saturn's heliocentric plane, the ring is tilted 27^o from Saturn's equatorial plane and the other rings. Phoebe's orbit is retrograde and inclined 5^o with respect to Saturn's orbit plane, and its resulting vertical excursions above and below the ring plane agree closely with the ring's observed thickness at Phoebe's distance of $\sim$40 Saturnian radii. Repeated impacts on Phoebe, from interplanetary particle populations, may keep the ring populated with material. Ring particles smaller than centimetres in size slowly migrate inward, with many of them ultimately striking the dark leading face of Iapetus [Burns et al., 1996, Verbiscer et al., 2009, Tamayo et al., 2011].

1.8 Further Thoughts

The survey of Saturn's more notable faint rings in this chapter gives a glimpse of the striking dynamics that these rings undergo and play host to. The D ring shows significant change in its exterior part. The G ring arc is an outcome of a resonance with Mimas. The F ring owes a lot to the two shepherd moons, especially to Prometheus, for creating its structure and dynamics. The E ring is unique in its double-layered structure and vast extent. These rings will continue to marvel and surprise observers and modelers as more features are uncovered in the future.

The following chapters will concentrate on the structures in the immediate vicinity of E-ring (Ch. 2), and the dynamics of particles associated with the arcs of Anthe and Methone and the Pallene ring (Ch. 4).

CHAPTER 2

A SHORT HISTORY OF PARTICLES LAUNCHED FROM ENCELADUS INTO SATURN'S E RING

2.1 Introduction

In Cassini and ground-based images, Saturn's E ring first appears at $3R_S$ (R_S = 1 Saturn radius = 60,330 km), peaks sharply near the orbit of the satellite Enceladus (about 4 R_S), and slowly fades into the background at about 8 R_S. A narrow size distribution of particles, having a typical radius 1.0 ± 0.3 μm, provided the best fit to the pre-Cassini data [Showalter et al., 1991]. This peculiar size distribution indicates that the ring particles do not originate from collisional or disruptive processes, and are unlike most other rings.

Instruments on Cassini, like the dust detector (CDA) and the radio and plasma wave science instrument(RPWS), provided data on the size distribution of E ring particles greater than a micron [Kurth et al., 2006, Kempf et al., 2008]. The brightness variations of images obtained by the Cassini imaging science subsystem (ISS) allow, by scattering theory a determination of the particle sizes. They indicate, for smaller particles (about half a micron to a micron); a distribution of particle size using scattering images Hedman et al. [2012].

Even prior to Cassini observations, many believed that particles ejected from Enceladus populated the E ring [Baum et al., 1981]. Images from the Voyager space probes revealed that Enceladus' surface is complex with some youthful areas [Smith et al., 1982]. Very high-phase-angle images were taken in November 2005 specifically to examine the region over the South pole [Porco et al., 2006]. Several

prominent, almost 130-km long fractures, called 'tiger stripes' were seen near the South pole [Porco et al., 2006] in Cassini flybys. These images provided striking evidence of many narrow jets of fine icy particles emanating from the South polar terrain (SPT) in various directions to supply a much bigger, fainter plume towering over the South polar region by at least 435 km [Porco et al., 2006]. Eight hot-spots have been located as the primary sources of these jets [Spitale and Porco, 2007]. Most grains are ejected from these spots at speeds much smaller than Enceladus' escape speed of 240 m/s [Hedman et al., 2007b]. Models have been proposed on how these grains are formed in the vents that feed these cracks from beneath [Schmidt et al., 2008, Ingersoll and Ewald, 2011, Kieffer et al., 2009, Postberg et al., 2011]. They have also suggested extreme geologic youth for the SPT. The VIMS spectra too indicates the presence of pure water ice with a characteristic size for plume particles of a few microns [Hedman et al., 2007b].

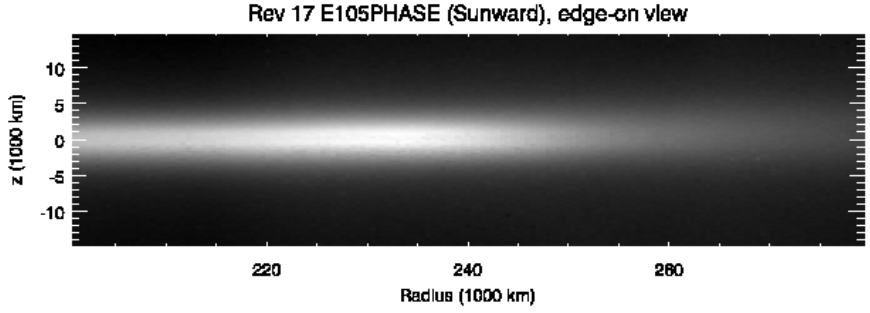

Figure 2.1: Edge-on view of Saturn's E ring showing double-layered vertical structure at a phase angle of 105^o. The faint grey line bifurcating the ring at the equatorial plane (z $\sim$ 0) indicates a relative scarcity of particles in the equatorial region. The vertical distance between the two layers is about $\sim$ 2000 km [Hedman et al., 2012]. Same as Fig. 1.13.

Cassini images presented herein show that the spatial density of the E-ring particles is not maximum at the ring's equatorial plane (Fig. 2.2). Rather, it attains its maximum density $\sim$1000 km above and below Enceladus' orbital plane, forming a double-layered structure (Fig. 2.1). This dip ($\sim$ few percent from the

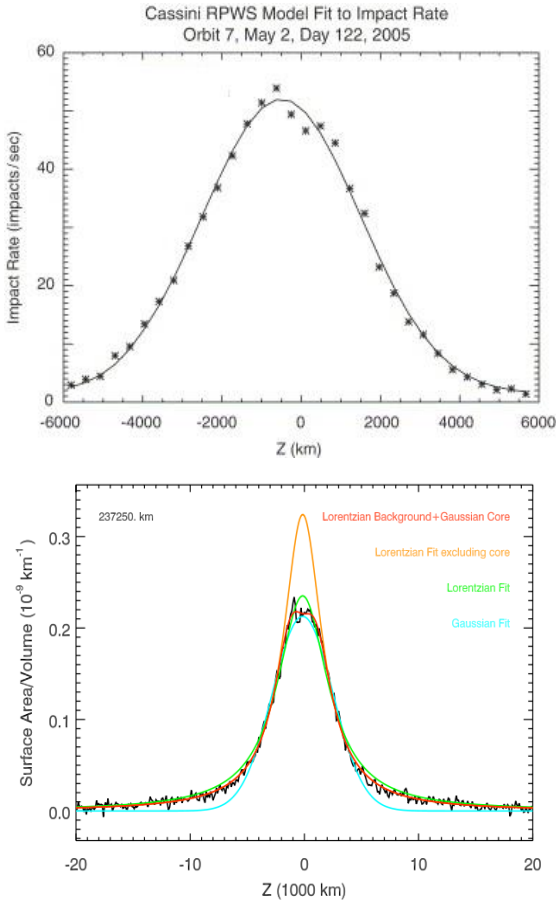

Figure 2.2: Top: Number of particles as detected by the Radio and Plasma Wave Science Instrument (RPWS) in the vertical direction off the E ring [Kurth et al., 2006]. The curve is a gaussian fit to the impact rate data. The dip at the equatorial plane is apparent. Bottom: Surface area/volume as obtained from the edge-on image of the E ring showing a dip at the equatorial plane (Fig. 2.1). Lorentzian and Gaussian fits are shown, making the dip apparent [Hedman et al., 2012]. The dip is almost twice the size of Enceladus' Hill radius, r_H ($\sim$1000 km).

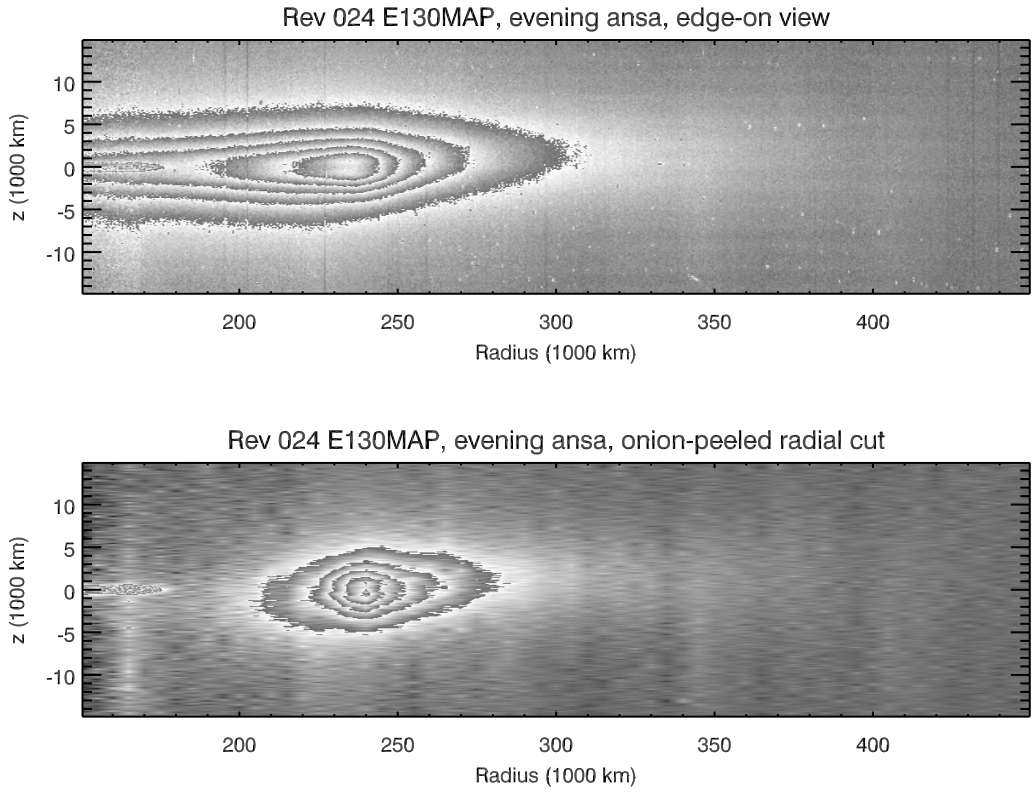

Figure 2.3: Edge-on views of the E ring derived from the Rev 024 E130MAP observations. The top image shows the ring's observed brightness as a function of radius ρ and z, while the bottom image shows the onion-peeled data (as explained below), which represent the local brightness density as a function of ρ and z. For clarity, the vertical scale is enhanced by a factor of $\sim$3 relative to the horizontal axis. Both images use a cyclic stretch (where the displayed brightness equals the intrinsic ring brightness modulo some number) in order to illustrate both the brighter and fainter parts of the ring. A faint dip in brightness near the midplane can be seen near the core of the ring around 240,000 km from Saturn center. Also note that the ring's peak brightness seems to occur at slightly positive values of z outside 240,000 km and slightly negative values of z inside 240,000 km in the onion-peeled image [Hedman et al., 2012].

peak) is apparent in the density profile obtained from the image (Bottom: Fig. 2.2). A similar observation was made by the RPWS instrument, which measured the dust-impact rate while moving vertically through the ring plane (Top: Fig. 2.2) [Kurth et al., 2006]. The distance between the two layers is approximately twice Enceladus' Hill's radius. Hill's radius (r_H) is the sphere of gravitational influence of the moon (versus that of Saturn's gravity), and for Enceladus, is about 4 times its physical radius (r_E),

$$r_H = a_E \left(\frac{M_E}{3M_S} \right)^{1/3} = 3.8 r_E, \tag{2.1}$$

where a_E is moon's semi-major axis, M_E is moon's mass and M_S is Saturn's mass.

The dynamics of the E ring has been investigated by many authors. Horanyi et al. [1992] described the evolution of particles from Enceladus under the effect of Saturn's gravity including its oblateness, electromagnetic forces and solar radiation pressure. They found that micron-sized particles spread significantly radially. Motivated in part by this study (well before the Cassini flyby), Hamilton and Burns [1994] suggested that highly eccentric orbits introduced high-speed collisions that produced further ejecta to provide a continuing source for ring material. Possible seasonal variations in the density and spatial distributions of dust in Saturn's E ring were also explored by Juhász and Horányi [2004]. The radial extent of the E ring was further investigated using Cassini data [Horányi et al., 2008]. In an analysis of the E-ring images Hedman et al. [2012] find that the gaussian core ('halo') of the double-layered ring radially extends about 30,000 km (Fig. 2.3). Kempf et al. [2008, 2010] studied the dynamics of E-ring particles just as they leave Enceladus using dust impact data and simulations under gravitational and non-gravitational forces (electromagnetic and radiation forces). Their simulations show that particles with sizes greater than $0.7 \mu m$ can escape to the E ring only if

the initial speed is higher than 222 m/sec, which produces a minimum inclination of 0.2^o. Also, tiny particles are not only affected by this moon's gravity, but also dragged by Saturn's rotating magnetic field. Hence, the effective escape speed of a jet particle depends on its size as well as its launch location. They show that for sizes greater than 5 μm non-gravitational forces are negligible. It is also critical to note that in these studies [Kempf et al., 2008, 2010] the cut-off speeds (minimum speed required for launch to escape collision with the moon) are very similar for sizes 0.5 μm to 5 μm. The authors go on to describe the gradual disappearance of the imprint of the plume in the long-term dynamical evolution of E-ring grains. We show in this work how gravitation alone is capable to produce the double layered structure, hence making the need of non-gravitation force to explain this structure unnecessary.

It is worthwhile to contrast the E-ring's double-layered structure against Jupiter's gossamer rings. The latter have a curious rectangular structure with the top and bottom of the ring brighter than the interior, giving it a double-layered structure too [Burns et al., 1999, Ockert-Bell et al., 1999]. The maximum thickness of the gossamer rings from the central planet's equatorial plane is the same as the height of their corresponding source satellites, Amalthea and Thebe. If the particles are on approximately circular orbits with semimajor axes and inclination equal to, or smaller than, the satellites' but randomly oriented nodes, the double-layered rectangular structure can be explained. Such an array of particles (presumably starting from the surface of the ring-moons and evolved inwards due to Poynting-Robertson drag [Burns et al., 1984], and nodes recessed due to Saturn's oblateness), will be concentrated (and hence be preferentially seen) as they are the slowest at the top and bottom of their epicyclic vertical oscillations. The case of E ring is different in

two ways. Firstly, Enceladus is not inclined significantly and the vertical extent of the E ring goes way beyond the vertical oscillation of Endeladus. Secondly, Enceladus is much bigger and massive than Jupiter's moons and hence we expect to see more effect of Enceladus in the E ring. We will see in the subsequent analysis how the double layer of E ring is fundamentally different from that of Gossamer ring.

In this study, we concentrate on the structure of the E ring near Enceladus under gravitational forces, including Saturn's oblateness and other nearby moons. Electromagnetic forces have not been included to isolate the effect of gravity. In fact, we will show in our simulations and analysis that gravitational forces alone can explain the double-layered vertical and radial core structure near the moon. Though the sizes of the particles have a significant effect on cut-off speeds [Kempf et al., 2008, 2010], the double layer is a result of gravitational effects, i.e., the first few close encounters with the moon. The short-term (1-2 days) and longer-term ($\sim$200 yrs) evolution will be discussed to explain the E-ring's equilibrium form. We aim at providing a deeper understanding into the formation of the double-layered structure in the E ring near Enceladus' orbit, by detailing the fundamental role Saturn's and Enceladus' gravities play in the initial life span of the particles.

The organization of this chapter follows: in the next section we present the numerical set-up and initial conditions employed for our simulations. In section 3 we outline some of the analytical arguments that provide relevant time scales. Section 4 presents the analysis of particles for shorter time-scales (1-2 days) whereas section 5 considers longer time-scales ($\sim$ 200 yrs). We present the model of E-ring core in section 6 and summarize our results and conclusions in section 7.

2.2 Numerical Setup

Simulations presented here were carried out using the SWIFT multi-body integrator [Levison and Duncan, 1994b]. In a Saturn-centric coordinate system, Enceladus moves on a nearly circular orbit. In most of our simulations particles are emitted from the South polar region, normal to the surface of the moon, with a uniform speed distribution from $0.8v_{esc}$ to $1.9v_{esc}$, where v_{esc} is the nominal escape velocity (see immediately below for definition) at the surface of Enceladus. Anything below $0.8v_{esc}$ collides with the moon in its first orbit and is uninteresting for our studies. Similarly, anything above $1.9v_{esc}$ escapes to space far way from our region of interest around Enceladus, and is not included in our simulations. We define a nominal escape velocity, v_{esc}, as the escape speed needed from an isolated spherical moon; it is given by

$$v_{esc} = \sqrt{\frac{2GM_E}{r_E}}, \tag{2.2}$$

where G is the gravitational constant, M_E is Enceladus' mass and r_E is Enceladus' radius. The nominal escape velocity for Enceladus is 240 m/s. Notice that particles in the Saturnian system may still be able to escape Enceladus' gravitational field at velocities lower than v_{esc} depending on the direction of launch and location [Dobrovolskis and Burns, 1980]. We also define the cutoff velocity (v_{cutoff}) as the minimum speed of launch, normal to the surface, required to escape collision with the moon in the first few orbits of the particle. In some of our simulations, a Gaussian probability distribution was used instead of uniform distribution for velocities of particles launched perpendicular to the surface. We will give details in later sections.

A particle's launch velocity as seen from Saturn is the vector sum of the velocity

of Enceladus plus some velocity in the normal (v_N), radial (v_R) and tangential direction (v_T) to the orbital plane. We also carried out some simulations with an additional velocity added along radial and tangential directions to the moon's orbit ranging between $-0.5v_{esc}$ to $0.5v_{esc}$. Negative velocities mean directions opposite to the tangential motion of the moon and radially inward components. In most simulations we launch 10000 particles normal to the surface from near the South pole, all at once. Particles are terminated if they return to the surface of the moon.

The system is evolved for ∼200 years. Units are chosen to keep G = 1. The time unit (T) is 1 Earth day and the unit of length (L) is the orbital distance from Saturn's center to Enceladus' center, a_E. This scaling gives the unit of mass (M) as $M = L^3G^{-1}T^{-2} = 2.70702 \times 10^{25}$ kg. Table 4.1 lists the various units used in the simulations.

2.3 Time Scales

We will now discuss the time-scales over which the orbital properties of E-ring particles evolve in the Saturn-Enceladus system. These range from Enceladus' orbital period around Saturn to the time of collision of particles with the moon.

The percentage of particles that avoid impacting into Enceladus, as a function of time, is shown in Fig. 2.4. These particles were started from the South pole (details in the caption of Fig. 2.4). At time 0 the percentage of particles remaining is 100%. We see a sharp drop (within 1-2 day) in the number of particles, followed by a slow decay. There are, thus, two primary time scales in the system - the shorter initial transient-state time-scale and the longer equilibrium-state time-scale. The

Parameter	**SI units**	**SWIFT units**
Unit of mass	1 kg	2.71×10^{25} kg
Unit of length	1 m	2.38×10^{8} m
Unit of time	1 sec	8.64×10^{4} sec
Gravitational constant (G)	$6.67 \times 10^{-11}\ Nm^2/kg^2$	1
Mass of Saturn (M_S)	5.68×10^{26} kg	21.00
Mass of Enceladus (M_E)	1.08×10^{20} kg	3.99×10^{-6}
Radius of Saturn (R_S)	6.0268×10^{7} m	0.25323
Semimajor axis of Enceladus' orbit (a_E)	2.38×10^{8} m	1
Radius of Enceladus (r_E)	2.5×10^{5} m	1.05×10^{-3}
Orbital velocity of Enceladus (v_{orb})	1.26×10^{4} m/s	4.58
Nominal escape velocity from Enceladus (v_{esc})	240 m/s	0.087
Hill radius of Enceladus (r_H)	9.49×10^{5} m	3.99×10^{-3}
Saturn's gravity dipolar coefficient (J_2)	0.016298	0.016298
Saturn's gravity quadrupole coefficient (J_4)	-0.000915	-0.000915

Table 2.1: Physical properties in terms of SI and SWIFT units [Murray and Dermott, 1999, pp.∼526-538].

time scale of the initial drop from 100% to 60% corresponds to the order of orbital period of Enceladus around Saturn (1.37 days). Since all the particles start from the moon's surface, they are under the strong influence of the moon's gravity to begin with. All the particles that do not exceed the cutoff speed collide with the moon within less than one orbital period. This cutoff speed (speed just enough to escape a collision with the moon on return which depends on direction and position of launch) for the case of Enceladus-Saturn system is $1.34v_{esc}$ (for particles launched normally from the South pole). Fig. 2.5 shows the time at which particles collide for a given start velocity from the South pole. The graph ends abruptly at $1.34v_{esc}$ showing that particles with initial velocity greater than the cutoff value escape the moon's gravitational field to join the E ring. The time scale associated with this graph is about half the moon's orbital period around Saturn. This shows

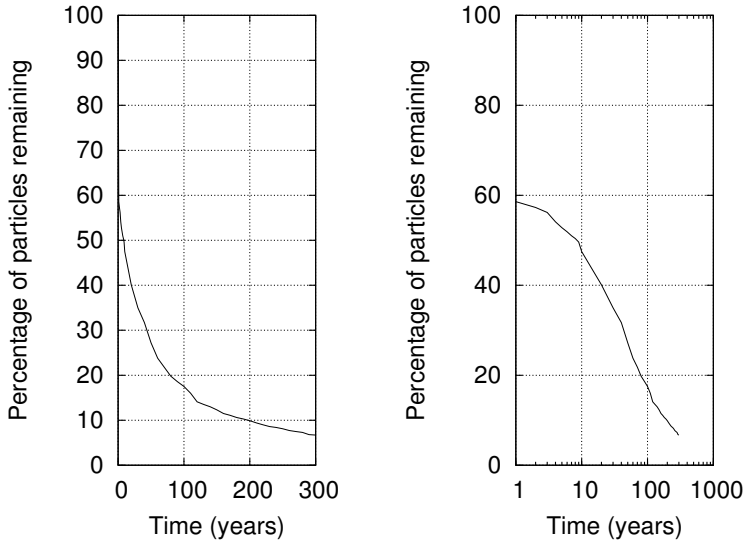

Figure 2.4: Percentage of 10000 test particles surviving as a function of time (left - linear scale, right - semi-log scale), starting from Enceladus' South pole, with their velocities uniformly distributed between 0.9 - 1.9 times v_{esc}, where v_{esc} is the nominal escape speed from the surface of an isolated moon. These particles have evolved under the gravitation of Saturn (J_2 and J_4 included) and Enceladus.

that particles lacking enough speed are eliminated quickly, never going into an independent orbit around Saturn. Kempf et al. [2010] also arrive at the same conclusion stating that the slow particles emanating from the moon collide after one orbit.

The second characteristic time for the dynamics of E-ring particles, shown in Fig. 2.4, is the ring's decay time, due to a typical E-ring particles colliding with the moon once they escape the initial transient phase. This decay appears to be a classical exponential loss. In the real model of the ring, if no other processes (e.g., non-gravitational forces) intervened, this time would correspond to the interval over which particles are supplied to the E ring by the observed plumes, if the ring is to remain in a steady state. From Fig. 2.4, the population of the ring particles fall to half of the particles left after initial phase in ~ 50 years. This collision time matches well with the following particle-in-a-box argument: if we imagine a torus

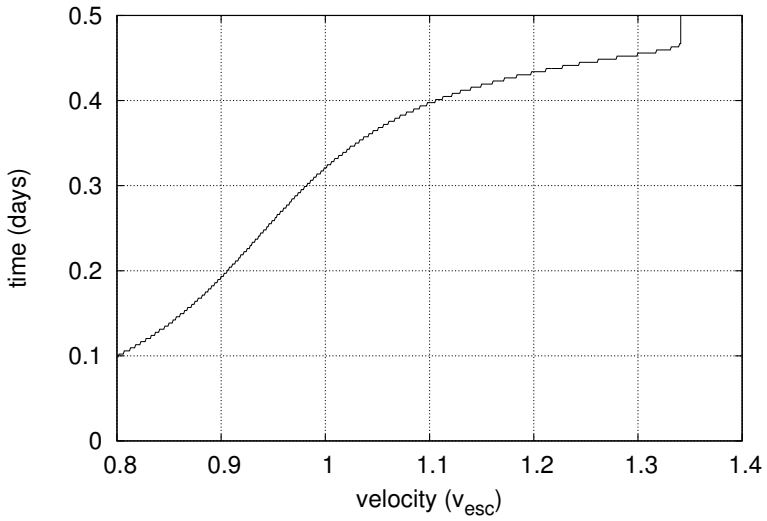

Figure 2.5: Time at which particles collide for a given initial speed launched normal from the South pole. The cutoff value is $1.34 v_{esc}$.

around Saturn produced by the sweeping of space by Enceladus and calculate the time it takes for the satellite to completely traverse the entire torus, we can get an average time scale for collisions of ring particles with the moon. The volume of the torus is the orbital circumference multiplied by Enceladus' cross-sectional area. The orbit circumference is $2\pi a$, where a is Enceladus' semi-major axis. The height is $a\times$ total inclination of the particle and the width is the radial speed $\times$ half an orbit period. The sweeping rate is $\pi R_m^2 \times$ radial speed. Following this idea, the expected time scale for sweeping up particles on crossing orbits can be calculated as

$$T_{coll} = \pi \sqrt{sin^2 i_m + sin^2 i_{tp}} \left(\frac{a}{R_m}\right)^2 \frac{U_r}{U} T_{orb}, \tag{2.3}$$

where i_m and i_{tp} are the orbital inclinations of the moon and the test particle, respectively, and a, R_m, and T_{orb} are the semimajor axis, radius, and orbital period of the moon (Hamilton and Burns, 1994). U is the random speed of the particle with respect to the moon, and U_r is the radial (with respect to a line through the center of the planet) component of this velocity; U_r/U should be about 0.5 for

particles that are on orbits similar to that of Enceladus. Using this, we estimate a collision-timescale for the particles with the moon. Using $i_m \approx 0$, $i_{tp} \approx \frac{v_N}{v_{orb}}$ we find $T_{coll} \sim 100$ years. So in a century about half the particles near the moon collide with it, as seen in Fig. 2.4. Presumably, the visible ring does not decay because it is fed continuously by the plumes.

Other significant time-scales in the system are the precession time-scale of test particles and the time-scale of close encounters with the moon. We can estimate the typical time for close encounters of the particles with the moon using the above formula if we employ r_H (Hill radius of Enceladus) instead of R_E (Enceladus' radius). This assumes that close encounters occur only when a particle comes inside Enceladus' Hill sphere. This gives $T_{enc} \sim 7$ years.

Saturn's oblateness causes particles' nodes to precess at a rate

$$\frac{d\Omega}{dt} = -\frac{3}{2} n_0 J_2 \left(\frac{R_S}{a_E}\right)^2, \tag{2.4}$$

[Murray and Dermott, 1999], where Ω is the longitude of nodes, n_0 is the mean motion of test particles and R_S is Saturn's radius. From Table 4.1, for Enceladus $\dot{\Omega} = 8.3 \times 10^{-8}$ rad/sec. Thus, the orbit of a typical test particle near Enceladus will precess by 2π radians in ~ 2.34 years. However, here we are interested in the differential precession of the particle with respect to the precession of Enceladus' orbit. This is because we wish to calculate how long it takes for the orbit of particles starting from Enceladus to drift away from the moon's orbit. Differentiating the above equation, we have

$$\frac{\triangle\dot{\Omega}}{\dot{\Omega}} = -\frac{7}{2}\frac{\triangle a}{a}. \tag{2.5}$$

We will see in a later section that a close encounter with the moon introduces a typical change in semimajor axis of the order of $\frac{\triangle a}{a} = 0.02$, corresponding to

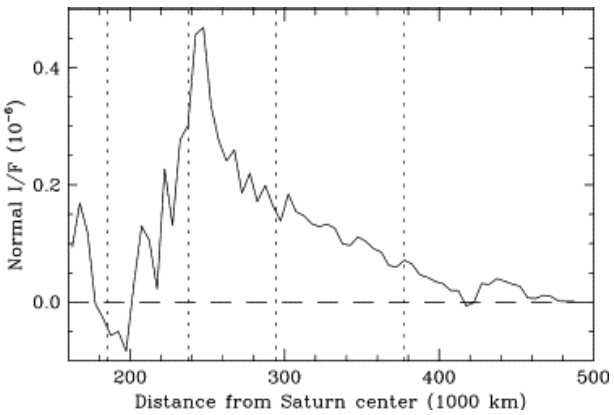

Figure 2.6: Vertical normal optical depth of the E ring as a function of radial distance [Nicholson et al., 1996].

$\triangle\dot{\Omega} \approx 5.8 \times 10^{-9}$ rad/sec. Therefore, an orbit of a typical test particle will differentially precess with respect to the moon by 2π radian in ~ 34 years. Over this time the vertical structure becomes azimuthally symmetric.

The last of the time-scales significant for our analysis is the time during which the E ring was formed or fed to an equilibrium state. An upper limit on this can be calculated approximately if we assume that the entire E ring is fed by the South pole plumes of Enceladus and that collision with the moon is the only loss mechanism. Other loss mechanisms (e.g., non-gravitational forces causing particles to move to "safe" orbits, or the sublimation/ sputtering of ring particles) would require more time to supply the current ring. We claim that the time in which a typical particle collides with the moon is of the order 100 years. Hence, if collisions with the moon are the only sink of the particles in the E ring, the time it would have taken for the whole E ring to emanate out of Enceladus should also be around 100 years. We show a calculation here to justify this claim.

Fig. 2.6 shows the normal optical depth profile of E ring. Assuming that the E ring extends from 2×10^8 m (R_1) to 5×10^8 m (R_2) from Saturn, we can estimate an average optical depth τ of the order of $\sim 0.1 \times 10^{-6}$ [Nicholson et al., 1996]. Such a low optical depth implies that the ring has very few particles per unit volume. This validates the assumption that almost no collisions happen between the particles (for $\tau << 1$). The optical depth roughly equals the fraction of surface area occupied by the ring particles. Further, we assume that the particles have $r_{par} = 10^{-6}$ m [Showalter et al., 1991]. In this scenario, the number of particles per unit area, n, would be $\tau/(\pi r_{par}^2) \sim 10^5$. This means that the total number of particles in the ring, N, is $\pi(R_2^2 - R_1^2)n \sim 6 \times 10^{22}$. Assuming each particle is a sphere of radius 10^{-6} m, made of ice with density 10^3 kg/m^3, we get the total mass of the ring $\sim 2.5 \times 10^8$ kg. Porco et al. [2006] suggest that 0.04 kg/sec departs Enceladus' gravitational field from the plumes. This number is only 4% of the suggested required escape rate [Juhász and Horányi, 2002]. But more recently, Ingersoll and Ewald [2011] have claimed the mass of the ring to be $(12 \pm 5.5) \times 10^8$ kg. In this work, we use the rate calculated from the plumes after observations [Porco et al., 2006]. Dividing the mass escape rate by the total mass gives the time during which the ring has reached equilibrium, $\sim$ 100 years, or about the lifetime of a particle to collide with the moon. This could indicate that the ring is in dynamic equilibrium, with Enceladus acting as the dominant source and sink of the particles that comprise the ring. Ingersoll and Ewald [2011] also calculate the lifetime of particles as $\sim$ 8 yrs. Considering this claim and because the mass escape rate we have used is uncertain, the time to supply the ring could vary by an order of magnitude, weakening our conclusion. But, nevertheless, $\sim$ 100 yrs can serve as the absolute upper limit on the time of feeding the ring.

The prominent timescales calculated in this section are compiled in Table 2.2.

Process	Timescale
Initial collision time	~ 1 day
Close encounter with the moon	~ 7 years
Differential precession of the orbit	~ 34 years
Decay of the ring	~ 100 years
Ring life (time to feed)	~ 100 years

Table 2.2: Prominent timescales playing a role in the dynamics of E-ring particles near the orbit of Enceladus.

2.4 Analysis of orbits for short time-scales

The motion of particles in Enceladus' vicinity is complex. For a similar example near other moons, see Dobrovolskis and Burns [1980], who show that the behavior of ejecta from the satellites of Mars depends dramatically on the longitude of the primary impact, as well as on the speed and direction of ejection. Kempf et al. [2008, 2010] have described such orbits around Enceladus based on dust impact data and simulations. They compute the distribution of particles around the moon including gravitational and electromagnetic forces. Our studies are similar, except that we determine that the E-ring's double-layered structure and gaussian core (Fig.2.1) result from gravitational effects alone. Thus we are treating all particles as uncharged point masses in our simulations.

We first present the dynamics of E-ring particles emanating from the Southern hemisphere of Enceladus during one day. These particles originate in the plumes of water vapor and ice (dust) near the South pole of the moon [Porco et al., 2006].

Most of these grains are ejected at speeds (mean speed of 106 m/s) much lower than the nominal escape speed from Enceladus' surface (240 m/s) [Porco et al., 2006]. These particles move nearly vertically, perpendicular to the orbit plane, in the gravitational field of Enceladus; the tidal field of Saturn does not affect the motions in this direction, so close to the moon. It is, hence, natural to assume that only the particles with relatively high speeds (near and above the escape speed), escape the moon.

2.4.1 Trajectories from the South pole

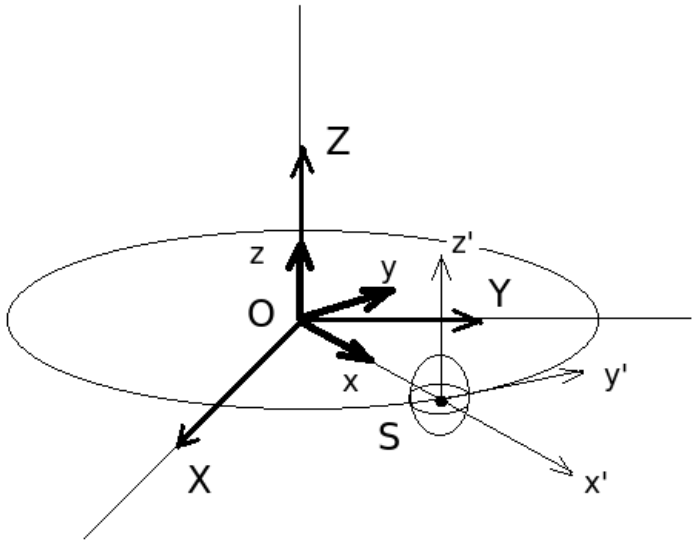

Figure 2.7: The coordinate system used in the simulations. The coordinate system XYZ (assumed intertial) is centered at Saturn (origin O), while x'y'z' rotates with the moon (at S) which orbits in the XY plane with a radius of a_E; they are aligned with XYZ when the moon passes through the X axis. We do our simulations in the xyz coordinate system, which is centered at origin O but rotates with the moon. At any general point of time, x points in the radially outward direction while y points in the direction of motion of the moon.

We first start with particles that leave exactly at the South pole. We are particularly interested in the minimum velocities ('cutoff' velocities) that permit a

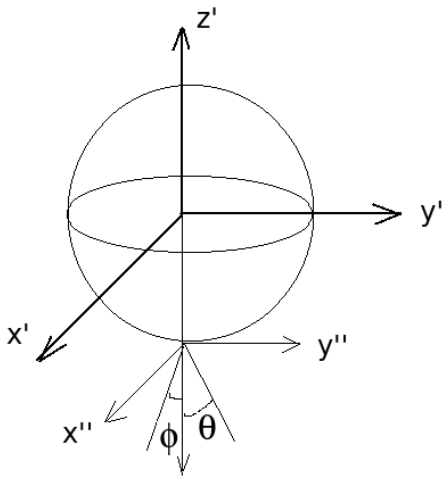

Figure 2.8: The velocity for inclined launch from South pole is determined by two angles: θ, the longitude from the negative z axis in the tangential direction and ϕ, the latitude from the negative z axis towards the outward radial direction.

particle to just escape the moon's gravitational influence and thus join the general E-ring population. We borrow the typical rotating reference frame (Figure 3.1) of the circular restricted three-body problem (Saturn, Enceladus, particle) to analyze the evolution of various orbits in the vicinity of Enceladus. In the rotating frame (xyz), Saturn is at the origin and Enceladus lies at a unit distance along the x axis (at t = 0, x and X are parallel). The x axis while rotating about the z axis, points radially outward, and the y axis is in the tangential direction (as given by the moon's velocity). Since the moon's rotation is tidally locked with its revolution around Saturn, the moon's spin will not complicate the initial conditions of launch and subsequent collisions. For the present case, where the launch is only from the South pole, the launch velocity's direction is specified by two angles: θ, the longitude from the negative z' axis in the tangential direction and ϕ, the latitude from the negative z' axis towards the outward radial direction (Fig. 2.8).

Enceladus' orbit has a negligible inclination (0.02^o, Murray and Dermott [1999]).

Hence, any initial vertical velocity of a test particle, ignoring the gravitational effect of the moon, should cause a vertical excursion (we define h to be the hypothetical height ignoring any interaction with the moon) of $\sim 18\gamma r_E$, where $\gamma = v_N/v_{esc}$.

$$h \approx ai = a_E \frac{v_N}{v_{orb}} \approx 18\gamma r_E. \tag{2.6}$$

The presence of Enceladus reduces the vertical excursion because every particle must climb out through the satellite's gravitational well, which slows them, giving them a smaller, and the true, vertical excursion (h'). Thus higher velocities are needed to reach a given vertical height than Eq. 2.6 prescribes. Conservation of energy (in the inertial frame centered at Saturn) can be utilized to derive the effect of initial slowing (assuming vertical launch from South pole and no significant x or y displacement):

$$\frac{v_N^2}{2} + \frac{n_o^2 r_E^2}{2} - G\left[\frac{m_S}{\sqrt{a_E^2 + r_E^2}} + \frac{m_E}{r_E}\right] = -\frac{n_o^2 r_E^2}{2} - G\left[\frac{m_S}{\sqrt{a_E^2 + h'^2}} + \frac{m_E}{h}\right], \tag{2.7}$$

where v_N is the normal launch velocity from the South pole, n_o is the mean motion of Enceladus around Saturn and h' is the maximum true vertical excursion. The term $\frac{n_o^2 r_E^2}{2}$ is the particle's kinetic energy, because of motion along the orbit; this appears on both sides and gets cancelled. Introducing four (non-dimensional) constants ($\mu = \frac{m_E}{m_S}$, $\beta = \frac{h'}{r_E}$, $\alpha = \frac{v_{esc}}{v_{orb}}$, $\delta = \frac{r_E}{a_E}$), we get

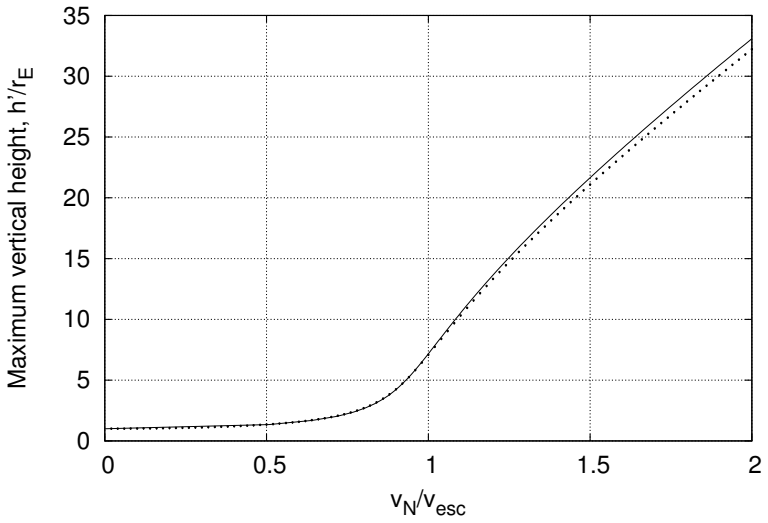

Figure 2.9: Enceladus' effect on the maximum vertical excursion of particles starting from the South pole of Enceladus. Dots are the simulation results, whereas the thin line is the theoretical prediction (Eq. 2.8). The curve starts to bend at around the Hill radius of the moon ($\sim 4r_E$).

$$\gamma = \sqrt{\left(1 - \frac{1}{\beta}\right) + \frac{\delta^2}{\alpha^2}(1-\mu)(\beta^2 - 1)} \tag{2.8}$$

from Eq. 2.7.

For our situation $\mu = 2 \times 10^{-7}$, $\alpha = 0.019$ and $\delta = 0.001$. Figure 2.9 shows the vertical excursions obtained using this expression (solid line) and verified against the simulation results (dotted line). At higher velocities the orbits deviate in the x-y plane due to the gravitational effect of Saturn and the theoretical and simulation curves diverge slightly.

The bend in the plot at $v_N/v_{esc} \sim 1$ happens when the second term in Eq. 2.8 overtakes the first. It occurs at values of h' roughly equal to moon's Hill radius, r_H. The close match of our simulation results to the analytical equation also shows that particles on vertical paths remain practically vertical inside the Hill sphere. Once they are outside, we start to see deviations from the analytical result as the

tidal forces from Saturn become important. It is valuable to note that this result is valid only for vertical launch from the South pole. We will see quantitatively similar behavior for other initial conditions in the next section.

We will now describe the path of a typical test particle. This particle is launched vertically from the South pole, normal to the surface with a velocity of $1.4v_{esc}$. Figure 2.10 shows the two-dimensional projection of the orbit onto xz and yz planes, as seen from Enceladus. Naturally, the particle slows down as it withdraws from Enceladus. On its return, it may possibly experience a close encounter with the moon. Such close approaches (departure and return) give gravitational kicks and specify the initial conditions on particles that enter the E ring and thus dictate the ring's vertical extent. The x-z projection (Fig. 2.10a) shows that, upon returning, the particle has experienced an outward radial drift. But more important is the y-z projection (Fig. 2.10b) which demonstrates that the close encounter occurs behind the moon and thus should increase the particle's energy (as in a gravity assist, Burns [1976]). The fact that the encounter happens orbitally behind the moon occurs because the particle's orbital period is slightly more than the moon's orbital period, owing to the extra energy that the particles start with relative to the moon; the semi-major axis and hence the orbital period are, accordingly, increased by this interaction.

Figure 2.11 shows the same event, but now as viewed in terms of dynamically significant quantities. We have plotted the instantaneous osculating semi-major axis and inclination (i.e., the orbital elements derived from the particle's radius and velocity vectors if the moon suddenly vanished) versus time in Fig 2.11a,b. It is clear that the inclination, which would have remained constant in the absence of

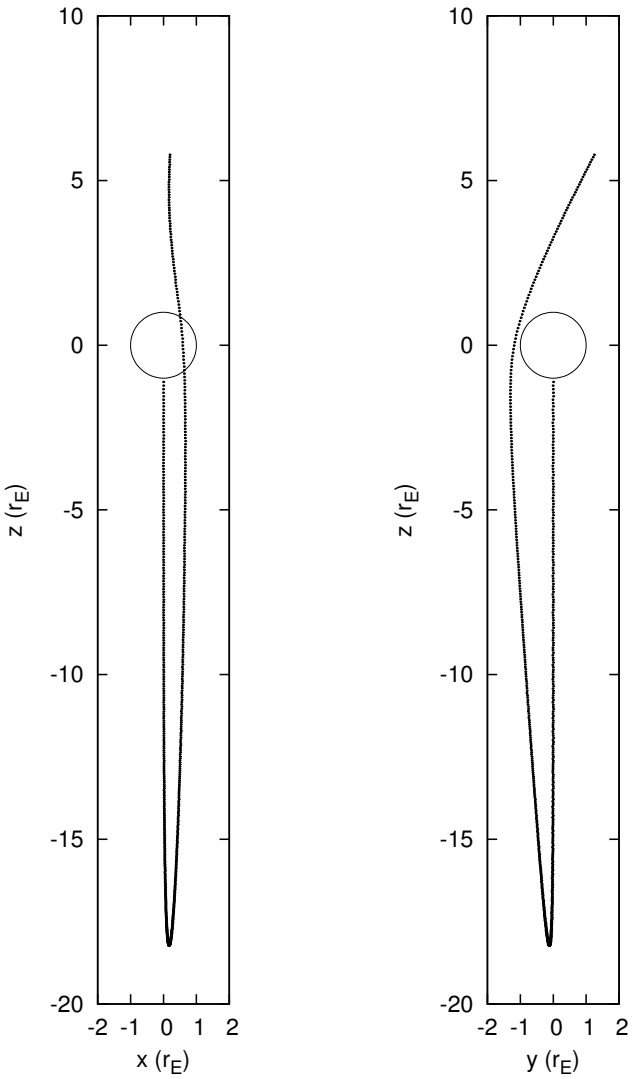

Figure 2.10: The 3-D trajectory for half a Saturnian orbit of a test particle as seen from a frame attached to Enceladus, with xyz defined in Fig. 3.1. The initial launch velocity is $1.4v_{esc}$. Since the close encounter occurs behind the moving moon, net energy is gained Burns [1976]. Left: radial-vertical cut. Right: tangential-vertical cut. Positive x corresponds to the radial outward direction and positive y corresponds to the direction of Enceladus' tangential velocity. The motion is a simple linear oscillator (epicycle) in z until the particle re-encounters Enceladus after a half-orbit of Saturn.

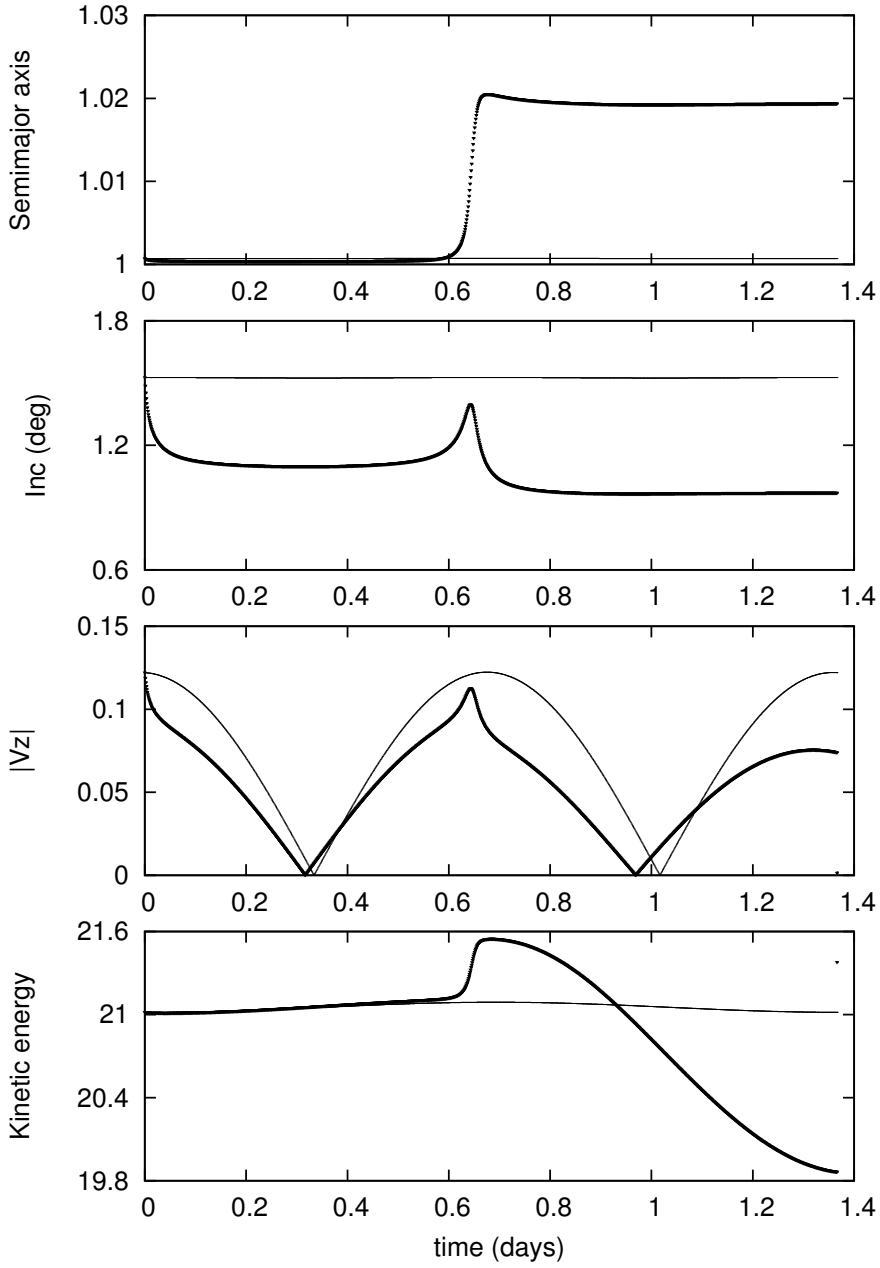

Figure 2.11: The effect of moon's presence on particles starting from the moon's South pole with a normal velocity of $1.4v_{esc}$ (Fig. 2.10). Notice how the osculating inclination and vertical speed decrease for this particle but the total energy increases due to the close encounter. Thin lines show the case with Enceladus absent while darker lines include the moon's effect. The units are given in Table 4.1.

the moon (Enceladus), decreases due to the gravitational deceleration caused by the moon. Enceladus' orbital period is 1.37 days, and so re-encounter happens at 0.69 days, just after half the period because of the slightly longer orbital periods of particles starting with 'extra' energy. As the particle returns, it gains vertical velocity and, hence, the osculating inclination increases. However, once the particle passes the moon, its inclination starts to decrease again due to slowing down. The point to note here is that the subsequent drop in inclination is more than the gain in inclination during the encounter. This produces a particle with a much lower inclination than expected for launch velocities in the absence of the moon. Overall, the massive moon slows down the particle's vertical movement and reduces its final inclination. Effectively, the moon damps the signatures of the initial launch velocity, and re-sets it to a new velocity after the close encounter.

Figure 2.11(c) provides the particle's vertical speed as a function of time. Without the moon present (thin line), the vertical motion is a simple harmonic epicyclic oscillation. The effect of the moon's presence (dark lines) decreases the vertical velocity and thus the osculating inclination. The particle's orbital period around Saturn also changes. This simply corresponds to the increase in semi-major axis. Fig. 2.11(d) shows how the total kinetic energy varies. The second encounter is critical; it increases the kinetic energy due to the "back-side" close encounter, as also shown by the growth in semi-major axis. After the close encounter, the kinetic energy oscillates, as it does for any particle on any elliptical path (cf. the vis-viva equation). Hence, these close encounters reduce the inclination but increase the overall energy and the semi-major axis of the test particle. If the particle has enough initial speed to escape, it feeds the E ring. It may eventually return and collide with the moon according to the probabilities of collisions on a longer time

scale.

Further, we can demonstrate that this 'cutoff' particle will avoid the moon using Kepler's third law. Let's consider the particle launched from the South pole almost vertically down in Fig. 2.12. We show the radial distance of this particle, its vertical height and its semi-major axis with respect to time. We also show, using solid vertical lines, the instances when the particle is at the equatorial plane. The particle is launched with a relative velocity of $1.34v_{esc}$ in the vertically down direction.

We start with an estimate of the change in the particle's orbital period. Since $T \propto a^{\frac{3}{2}}$, where T is the orbital period, we have

$$\triangle T = \frac{3T}{2a}\triangle a. \tag{2.9}$$

From Fig. 2.12 we see that, before undergoing the first close encounter, the change of semi-major axis is given by $\frac{\triangle a}{a} \sim 0.0002$, whereas after the second encounter the same ratio changes to $\frac{\triangle a}{a} \sim 0.02$. Using these two values, we get $\triangle T \approx 0.0003T$ and $\approx 0.03T$, respectively. Hence, the first time (after a little more than (i.e., 0.635) half the orbit period of Enceladus) when the test particle crosses the equatorial plane, it is about $\pi a_E \frac{\triangle T}{T} \sim 2r_E$ away from the moon, and hence misses the moon. In simulations we notice the particle just missing the moon. This can be seen in the top plot of Fig. 2.12. After this first close encounter when the particle approaches the moon again, it is about $\pi a_E \frac{\triangle T}{T} \sim 200r_E$ distance (i.e., after 1.306 days) away from moon. In simulations we see a distance of $\sim 100r_E$ (Fig. 2.12

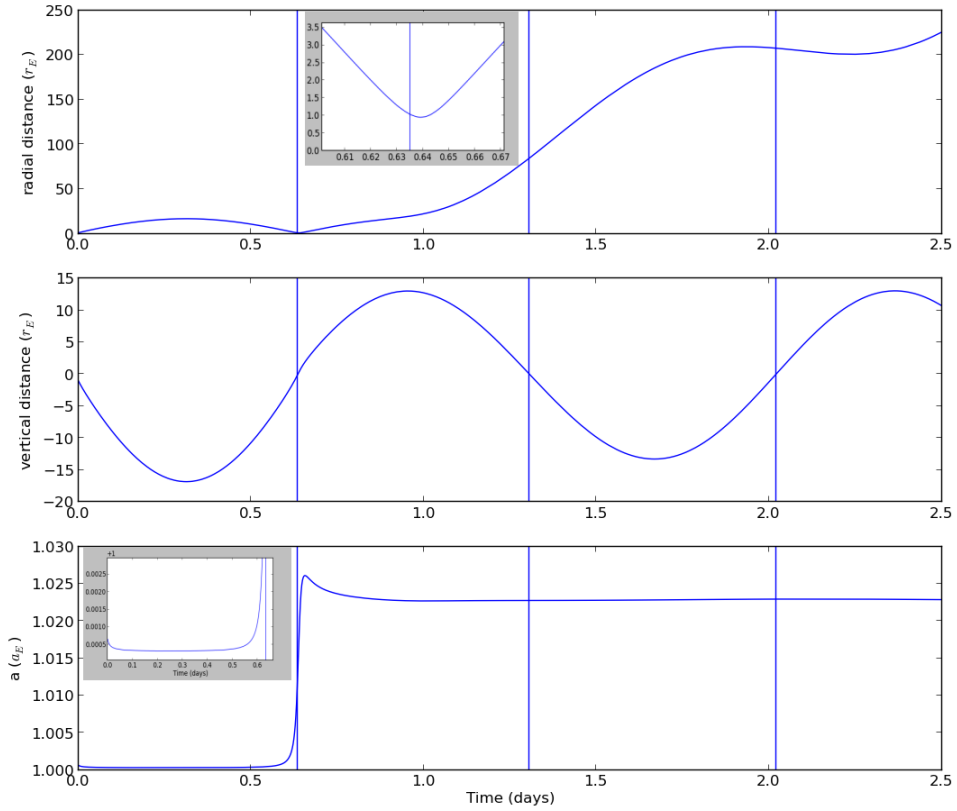

Figure 2.12: Radial distance between the moon and particle, vertical distance and semimajor axis for a particle launched from the South pole vertically down with a relative speed of $1.34v_{esc}$. The solid vertical lines show the instances when the particle is at the equatorial plane. Some areas are blown up to show them clearly.

top).

Let us now explore the effect of different launch speeds. We start with a perfectly normal launch with θ (longitude from the negative z axis along tangential direction) and ϕ (co-latitude from the negative z axis towards the outward radial direction) equal to zero. We observe that all the launches below 1.34 v_{esc} fall back upon the moon within the first orbit, most of them colliding in first half of the orbit. Anything above that speed undergoes a close encounter, is scattered and proceeds to join the E ring, as seen in Fig. 2.13. The inclination vs time plot (Fig. 2.13 top) shows that the particle with initial launch velocity of 1.2 v_{esc} returns and collides. Figure 2.13 (bottom) provides the two-dimensional projection (onto yz plane) of these orbits where the close encounters occur behind the moving moon, and hence increase the energy of the particle. Fig. 2.13 (bottom) also shows the moon's gravitational focusing effect (towards the end of the trajectory the moon attracts particles passing close to the surface). The particle whose velocity is slightly less than 1.34 v_{esc} grazes just past the surface and collides. The vertical elevations of these trajectories are determined by the formula in Eq. 2.8.

We now introduce tangential speeds to the projectiles by inclining them along the tangential direction (Enceladus' path). We keep ϕ zero throughout. Figure 2.14a shows the cutoff speeds for different angles of projection along the tangential direction. Even for a non-normal launch, we define cutoff speed as the minimum speed below which all the particles launched from the same position and with the same θ and ϕ collide with the moon. We can similarly introduce radial velocities (Fig. 2.14b). We observe that introducing a component of tangential, or radial velocity, reduces the cutoff velocities. This happens because these components

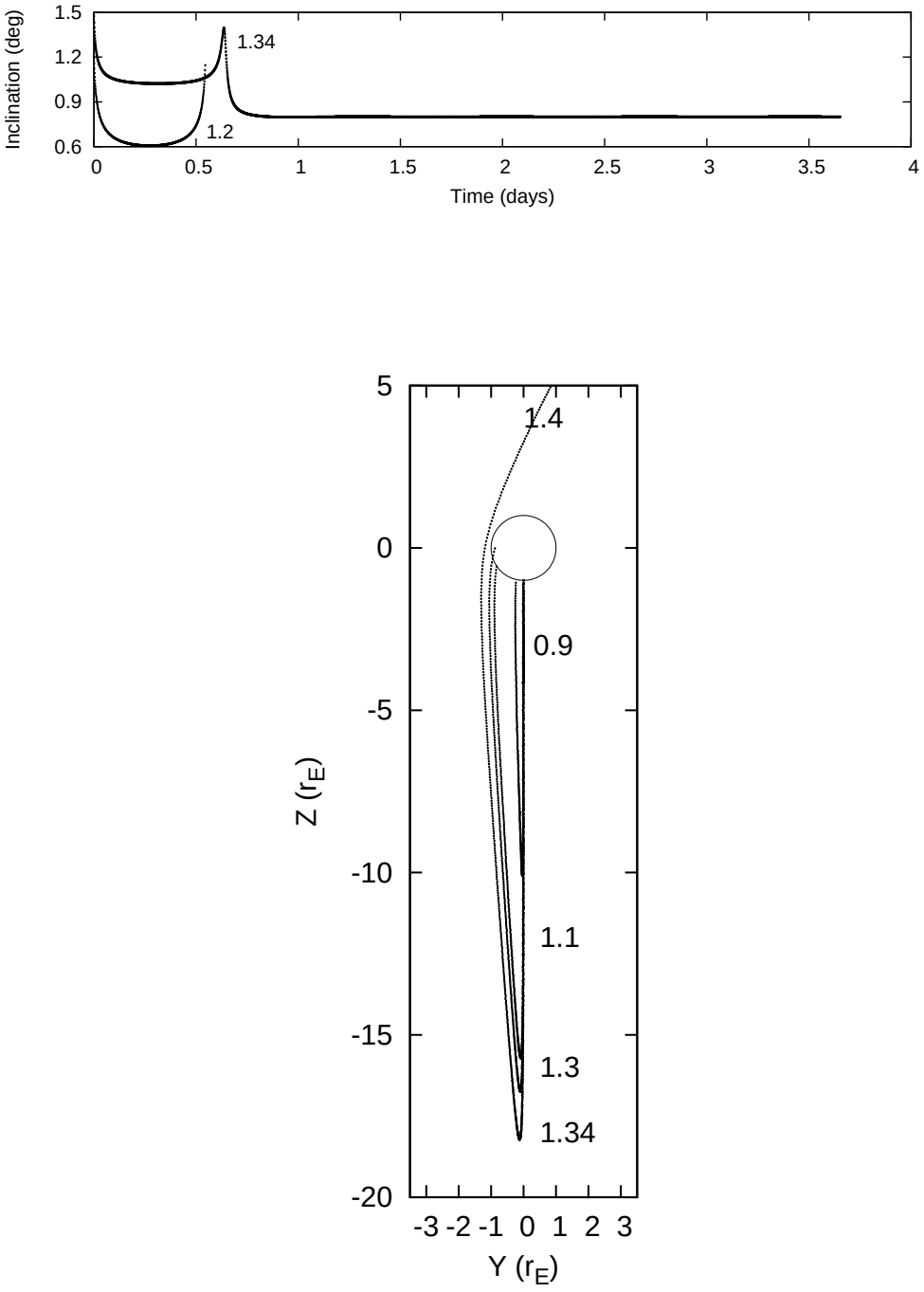

Figure 2.13: Escapes occur at speeds above 1.34 v_{esc} for normal launches from the South pole. Top: Inclination versus time: Notice that the overall effect of the two close encounters is to decrease the particle's inclination. Bottom: Two-dimensional projection of the orbit in the yz plane. All the encounters occur behind the moving moon. The numbers on the path are in units of v_{esc}.

change the orbital period considerably. Hence, such particles miss the moon when they return to the equatorial plane.

When launched in the direction of the moon's motion, an additional velocity ($v_{||}$) is gained in the direction of motion, which directly affects the orbital period of the grains. The Gauss' perturbation equations [Burns, 1976] give

$$\frac{dT}{dv_{||}} = 6\pi a_E^{\frac{5}{2}} \mu^{-\frac{3}{2}} v, \tag{2.10}$$

where T is the orbital period and v is the particle's speed, which is $\sim v_{orb}$. Because $T = 2\pi\sqrt{\frac{a^3}{\mu}}$ and $v = \sqrt{\frac{\mu}{a}}$, we obtain

$$\frac{\triangle T}{T} = 3\frac{\triangle v_{||}}{v}. \tag{2.11}$$

We can see these effects again from a simulation with a test particle launched from the Southern hemisphere as shown in Fig. 2.15. Now, for $v_{||} \sim v_{esc}$, after substituting the values ($\frac{\triangle v_{||}}{v} \sim 0.02$), we get $\frac{\triangle T}{T} \approx 0.06$. This means that when the particle next crosses the equatorial plane, it is $\pi a_E \frac{\triangle T}{T} \approx 400 r_E$ away from the moon, and hence misses it. We see a lower separation (100 R_E) in our simulations due to the effect of vertical velocity and the geometry of the launch. But these numbers still serve as an upper limit. The effect of radial velocity is different as follows: an additional radial velocity is perpendicular to the orbital velocity, hence the change in velocity is $\sqrt{v^2 + v_\perp^2} - v \sim 0.0002v$, for $v_\perp = v_{esc}$. This will make the particle miss by $\frac{T\triangle v}{2} \approx 3r_E$. The possibility of an immediate close encounter is much higher here.

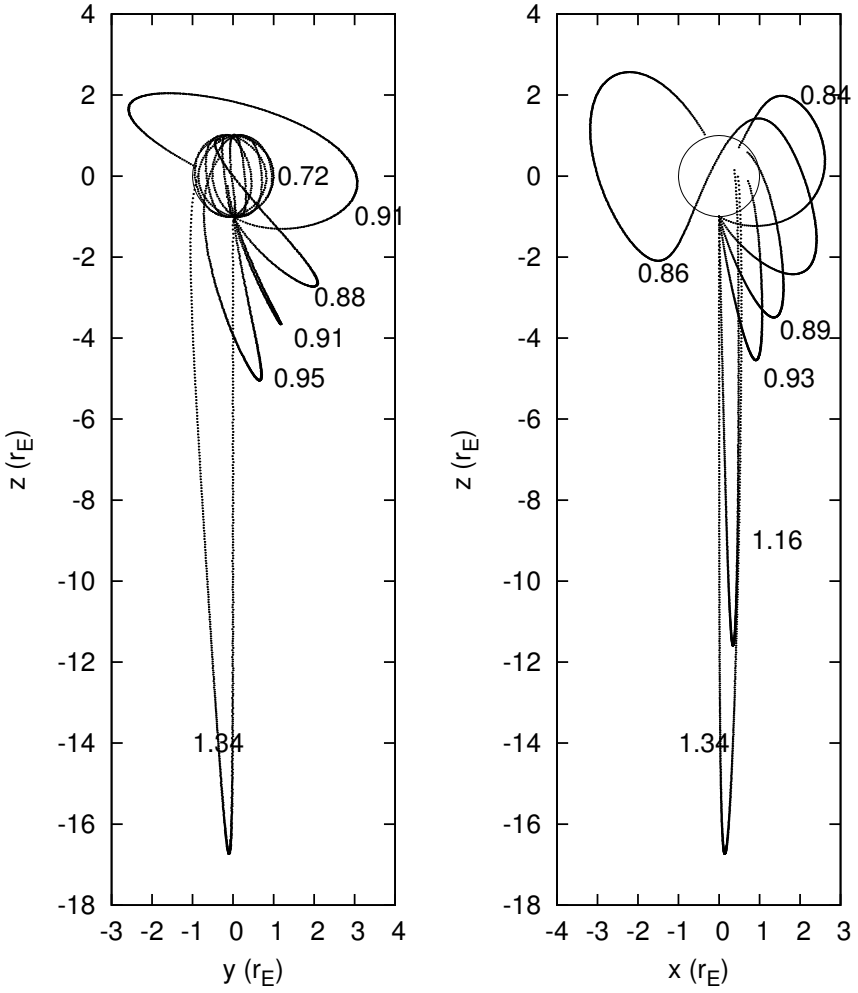

Figure 2.14: The values associated with each curve (in units of v_{esc}) are the corresponding cut-off velocities for launches from the South pole with different tangential and radial angles. All the particles in the plots graze past the moon's surface. Left: the cut-off speed decreases as the tangential component increases (we sequentially show $0^o, 15^o, 30^o, 45^o, 60^o, 90^o$). Right: the cut-off speed decreases as the radial component increases (in order $0^o, 5^o, 15^o, 30^o, 45^o, 60^o$). The orbits show that the close encounter happens behind the moving moon and in the radially outward direction. This increases the particle's orbital energy, semi-major axis, and orbital period.

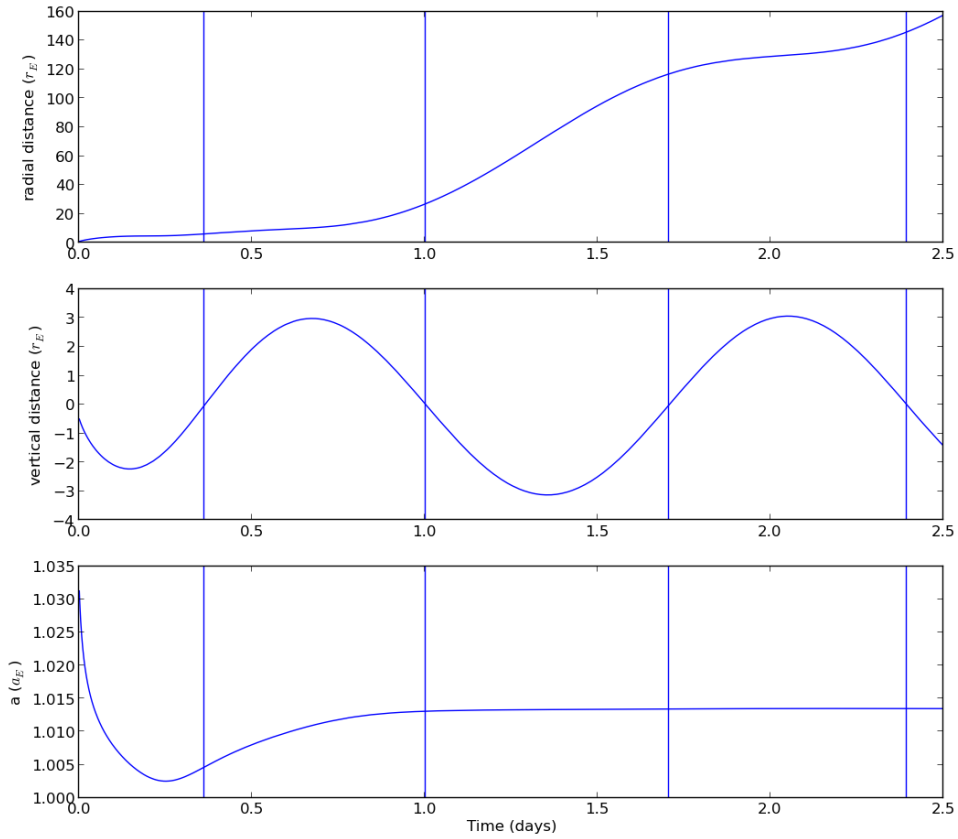

Figure 2.15: Distance between moon and particle (radial distance), vertical distance and semimajor axis for a particle launched from the southern hemisphere from position (60^o,90^0) with a cutoff velocity of $\sim 0.8 v_{esc}$ in the tangential direction and $\sim 0.5 v_{esc}$ in vertically down direction. The vertical lines are the times when the particle passes through the equatorial plane.

2.4.2 The fundamental role of Enceladus

Before describing the trajectories that start from other positions in the southern hemisphere, let us look at Enceladus' fundamental role in the early dynamics of E-ring particles. As we have seen in the previous section, Enceladus, apart from being the source of all these grains, plays an important role in the time evolution of the particles. We illustrate this by considering the case where particles are launched normal to the surface at the South pole all at once with speeds 1.4 - 1.5 v_{esc}. Recall that an orbit of a typical test particle differentially precesses with respect to the moon by 2π radian in $\sim$ 34 years (for $\frac{\Delta a}{a} \sim 0.02$) and the time between close encounters was calculated to be $\sim$ 7 years in the previous section. Figure 2.16 displays the vertical height plotted versus azimuthal launch angle (angle in the orbital plane from the reference X axis), for two time instants - after 1 year (dark dots) and 10 years (light dots). The sinusoidal shape (dark dots) signifies an inclined ring, which subsequently smears out to generate an axially symmetric cylinder. The 10-year snapshot shows the smearing effect, though it is still not completely axially symmetric. The fact that the time-scale for close encounters is less than the time of differential precession has an important consequence. The 'inclined ring' does not wait for 34 years to get smeared out because of differential precession. Instead, close encounters of the particles with the moon play an equally important, if not more important, role than the differential precession time-scale, in making the ring homogeneous.

In reality, the plumes from Enceladus are continuously putting particles all around the orbit. Effectively, the moon's motion continually re-positions the line of nodes for the orbits of the various particles and thus brings axial symmetry to

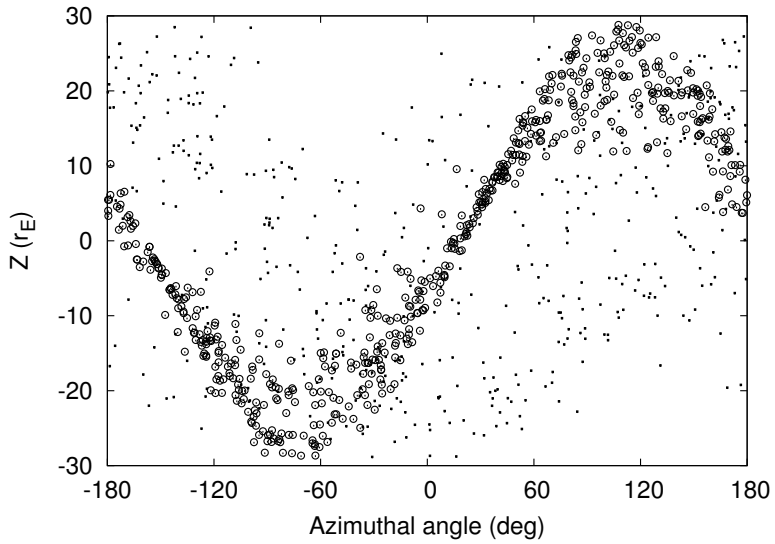

Figure 2.16: Vertical height plotted vs azimuthal angle (longitude in the ring plane relative to Enceladus) after 1 year (dark dots) and after 10 years (lighter dots). Particles were started simultaneously from the South pole all at once with speeds 1.4 - 1.5 v_{esc}. Subsequent close encounters and differential precession cause the 'ring' to smear out such that it moves towards becoming an axially symmetric cylinder. The light dots show the intermediate stage to the axially symmetric state. The sinusoidal shape after the original 1-year data signifies an inclined ring, with an inclination of $\sim z/a_E \approx v_{esc}/\sqrt{\mu/a_E}$.

the system within an orbital period (and makes the previous argument a heuristic exercise). The vertical motion of these particles, when away from Enceladus, is approximately that of a simple harmonic oscillator. In the absence of a moon, once given the initial vertical velocity, these particles will forever oscillate in the z direction. The moon plays three roles. Firstly, since the particles start near the moon, they are slowed as they escape and the elevations (or inclinations) reached by these particles are less than in the 'free' case (with no moon), as described in the last sub-section. Secondly, the moon acts as a mixer and agitator because of its close encounters with many particles. In the absence of a moon, the bunch of particles starting from the South pole of the moon have very similar initial conditions and hence will stay very close to each other. The moon gives 'random' energies to these simple harmonic oscillators due to close encounters, thereby mixing their phases. The end result is a more homogeneous ring in which the signatures of the initial velocities are wiped out. The fact that there is a continuous outflow of particles from the moon all around the orbit of Enceladus hastens the axial homogenization within one orbit (except for particles briefly trapped around Enceladus).

The third and final role of the moon is to act as an absorber of the ring material. Since the moon moves through the ring, it sweeps up particles on its way.

2.4.3 Trajectories from the southern hemisphere

We now delve into the significance and the role of the initial launch positions. To do this, we present results about the dynamics of particles emanating from different positions on Enceladus' southern hemisphere. The paths are similar to what happens for the launch from the South pole. We start the particles normal to the

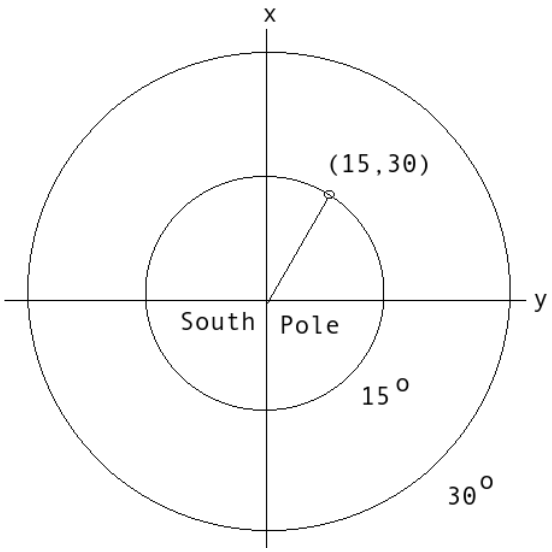

Figure 2.17: Positions in the southern hemisphere of Enceladus are given by a pair of angles, the co-latitude (as measured from the South pole) and the longitude (as measured from the x axis, which is the radial outward direction from Enceladus' orbit). The vertical upward, z axis points into the paper. Saturn lies in the negative x direction. For example, (15,30) denotes 15^o co-latitude from the South pole and 30^o longitude from the radially outward direction.

surface at all positions. We do not study the effect of launches tilted relative to the surface as we did for the South pole. But slightly inclined particles should have dynamics similar to particles with normal launch from nearby positions. What really matters is the direction and magnitude of a particle's absolute velocity vector; these depend on launch positions and launch angles. The positions on the southern hemisphere are denoted by co-latitudes (as measured from the South pole) and longitudes (as measured from the y axis; i.e., from the direction of Enceladus' velocity vector); see Fig. 2.17.

While launching the particles normal to the surface, we increase the particle's speed until the 'cutoff' value is reached. Again, the 'cutoff velocity' refers to the minimum speed below which all the particles collide immediately (i.e., within an

orbital period) with the moon, and above which all the particles join the E ring. We assume that the velocity distribution of the particles in the plume (i.e., before launch) peaks around a slow mean with only a small tail escaping the moon's gravitational field [Porco et al., 2006, Hedman et al., 2009b]. In such a model, the particles with speeds just above the cutoff values are the most abundant in the ring, and generate the ring's prominent features. We, henceforth, talk about the particles with these cutoff values, corresponding to different positions on the moon's surface. We find that higher-velocity particles are less susceptible to the effects of close encounters with the moon and reach much higher vertical heights, because with greater speeds, they get further from the moon and experience less of its gravitational effects. We will elaborate on this subtle, but important, point in the following paragraphs and, further, when we present the overall model of the E-ring's core, near Enceladus' orbit.

Figure 2.18 shows the contour of cutoff speeds for normal launch from different positions on Enceladus' southern hemisphere. Around 3601 particles were launched from the southern hemisphere within 60^o co-latitude from the South pole (uniformly distributed over the area) with a mesh grid of 2^o along co-latitude and 3^o along longitudes. The South pole corresponds to the position where the particle needs the maximum speed to escape Enceladus' gravitational attraction. As we increase the co-latitude away from the South pole, the 'cutoff' velocity decreases and finally settles down to about $0.84v_{esc}$ away from the pole. This has a significant implication: vents near the pole need to push out particles at higher velocities if they are to feed the E ring. As the co-latitude off the South pole increases, the requirement decreases. We will see later in this section how some of the hot spots in "tiger stripes" are 'fortunate' to be located away from the South pole. The

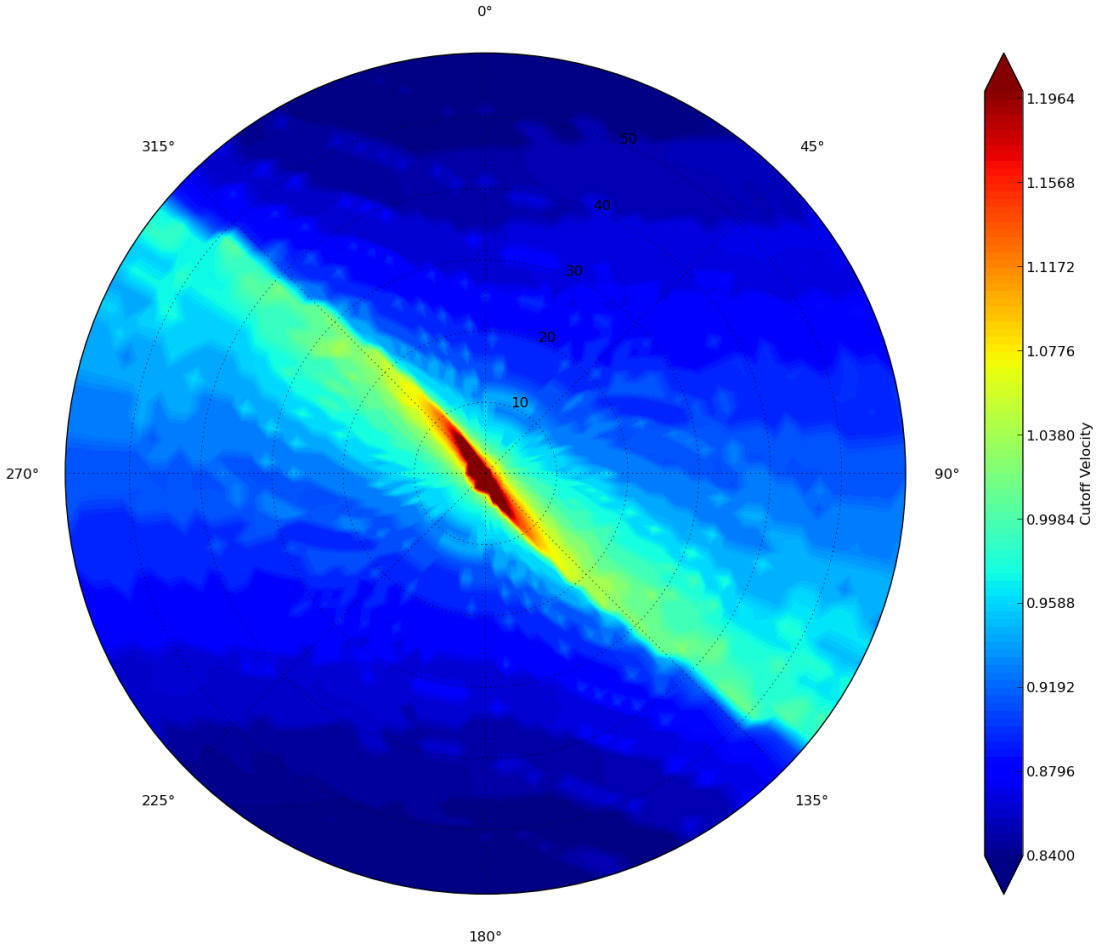

Figure 2.18: Contours of cutoff speed (given in v_{esc}) for normal launch from various positions in the southern hemisphere of Enceladus out to 60^o co-latitude. Notice the peak at the pole and how it settles down to about $0.85v_{esc}$ away from the pole. The non-smoothness of the curves is a result of the grid structure, which was plotted with a mesh of 2^o along latitude and 3^o along longitude (corresponding to 3601 points). The concentric circles correspond to the co-latitudes of 1^o, 20^o, 30^o, 40^o, 50^o and 60^o, respectively. The positive x axis (radial outward) is upwards (longitude = 0^o) and positive y axis (direction of moon's motion) is to the right (longitude = 90^o)in this and subsequent views.

patterns in this and subsequent contours (Fig. 2.18 - 2.22) will be discussed in some detail in a later subsection, where we will qualitatively explain these structures. Meanwhile, we can see similar contours for the eventual semi-major axis, inclination, eccentricity and direction of drift in Fig. 2.19 - 2.22, respectively. For details look at their captions.

Let us now venture into some of these trajectories. Figure 2.23 shows the trajectories in the vertical and radial plane when particles are launched with 'cutoff' speeds from different co-latitudes, at a fixed starting longitude of 10^o. Notice how the characters of these orbits gradually change when the co-latitudes are varied. Also notice the complicated two-knoted nature versus single bends in some of these orbits in both the vertical and horizontal planes. These patterns get reflected in the contours in Figs. 2.18 - 2.22. We will closely examine these patterns in the next subsection. These trajectories eventually settle into orbits around Saturn once the particles escape the moon. Depending on their initial positions, the particles either encounter the moon towards its leading side or its trailing side and hence either gain or lose energy. In general, we can observe that, if the number of encounters is odd the particle gains energy; but it will lose energy if the number of encounters is even. This is because the first encounter almost always occurs on the back-side (energy-increasing encounter). The 'cutoff' speeds also decrease moving away from the South pole as shown in Fig. 2.18.

Similarly the effect of launching from different longitudes from the surface of the moon can be seen from Fig. 2.24; these correspond to a fixed co-latitude of 30^o. We will elaborate on this effect in the next subsection.

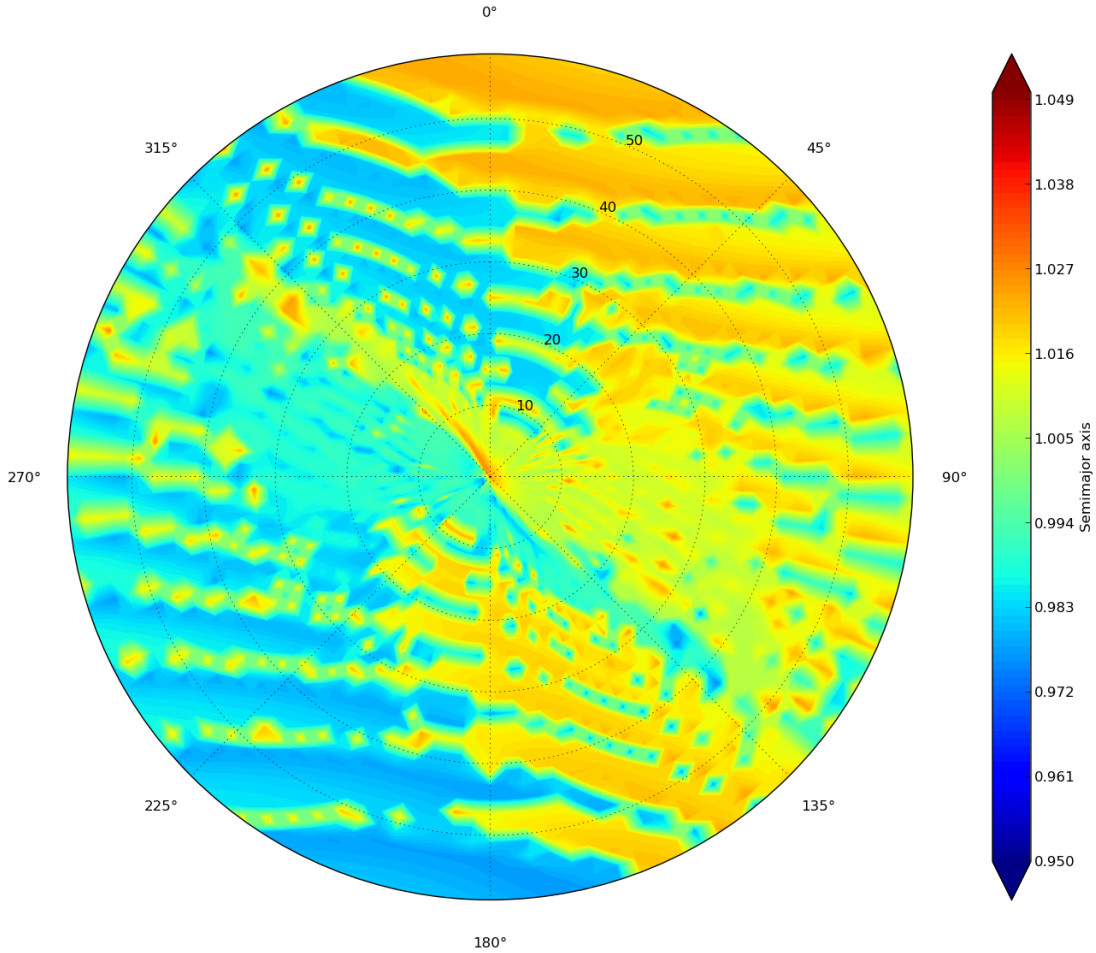

Figure 2.19: Contours of the eventual semi-major axis of orbits(given in unit of a_E) for normal launch from various positions in the southern hemisphere of Enceladus out to 60^o co-latitude. The non-smoothness of the curves is a result of the grid structure, which was plotted with a mesh of 2^o along latitude and 3^o along longitude (corresponding to 3601 points). The concentric circles correspond to the co-latitudes of 1^o, 20^o, 30^o, 40^o, 50^o and 60^o, respectively. The positive x axis (radial outward) is upwards (longitude = 0^o) and positive y axis (direction of moon's motion) is to the right (longitude = 90^o). The patterns here are similar to the ones seen in other contours.

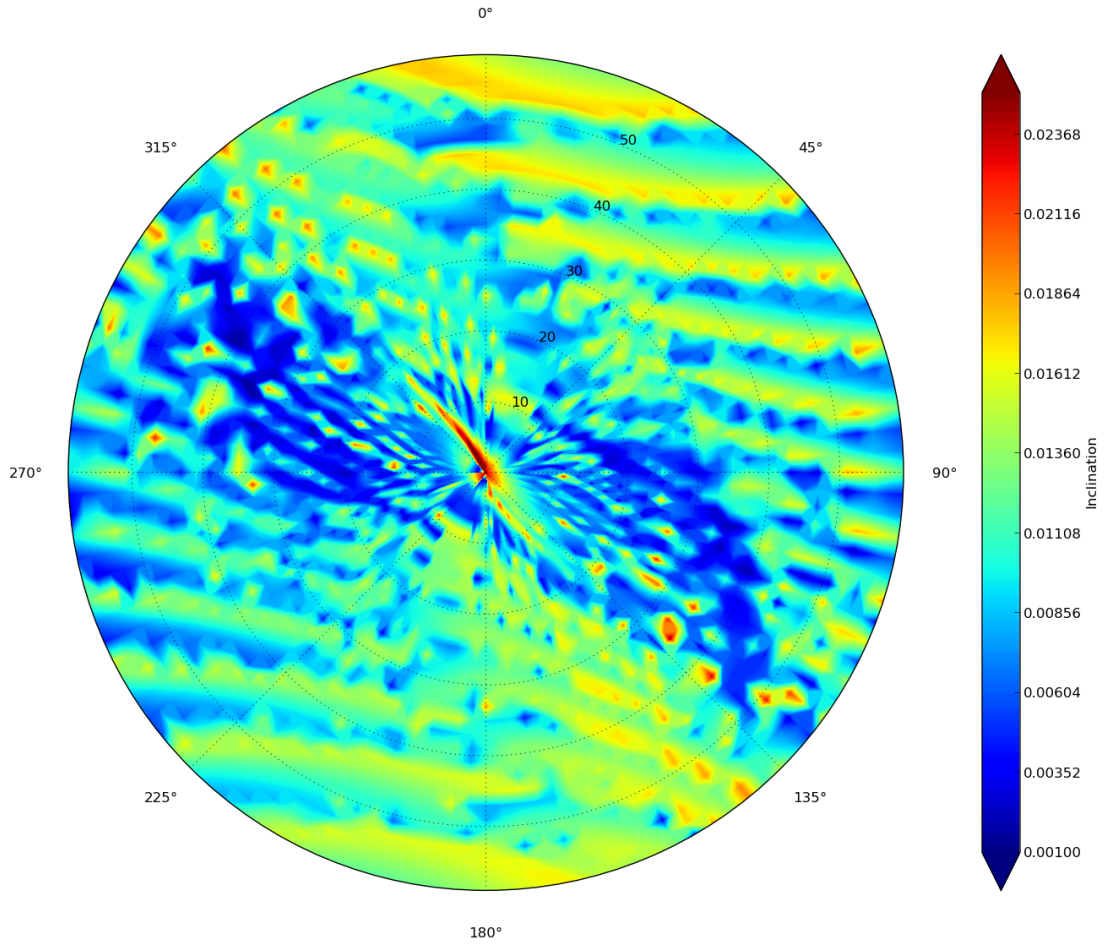

Figure 2.20: Contours of eventual inclination of orbits for normal launch from various positions in the southern hemisphere of Enceladus out to 60^o co-latitude. The non-smoothness of the curves is a result of the grid structure, which was plotted with a mesh of 2^o along latitude and 3^o along longitude (corresponding to 3601 points). The concentric circles correspond to the co-latitudes of 1^o, 20^o, 30^o, 40^o, 50^o and 60^o, respectively. The positive x axis (radial outward) is upwards (longitude = 0^o) and positive y axis (direction of moon's motion) is to the right (longitude = 90^o). The patterns here are similar to the ones seen in other contours.

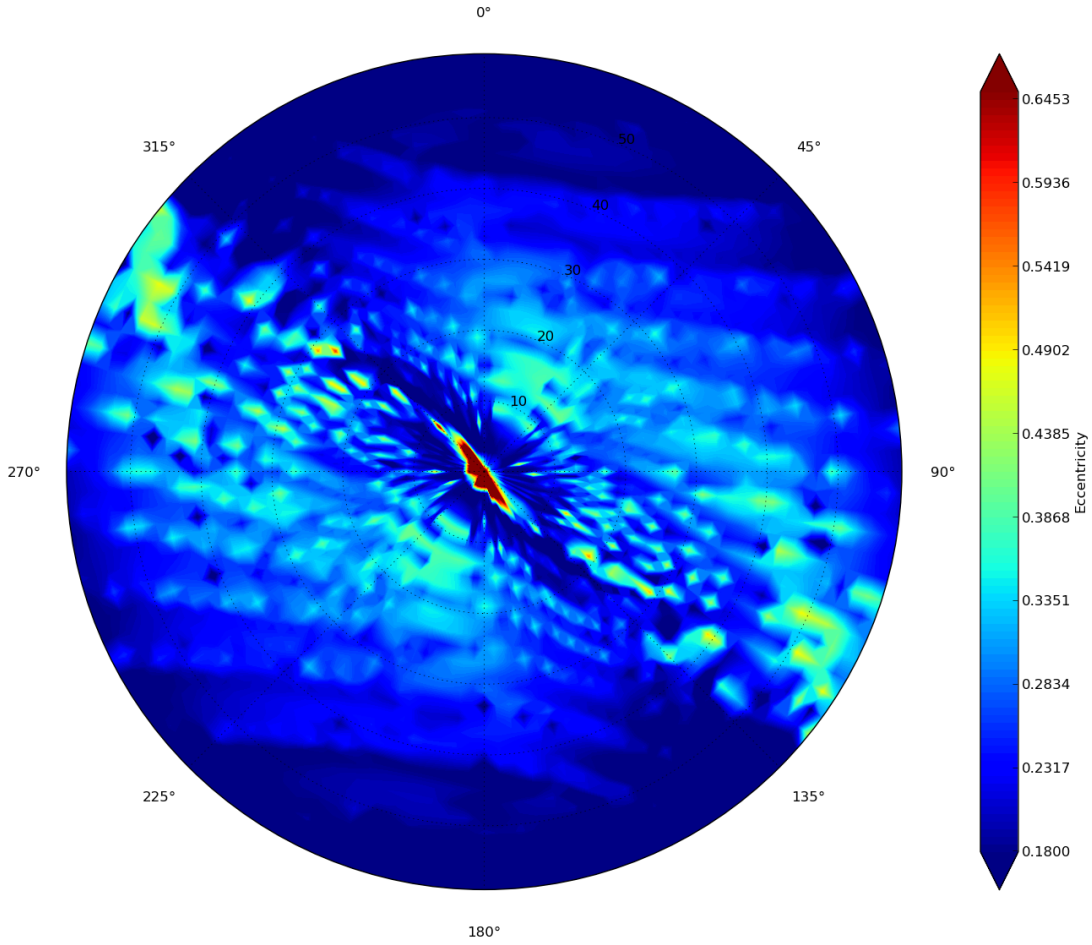

Figure 2.21: Contours of eventual eccentricities of orbits for normal launch from various positions in the southern hemisphere of Enceladus out to 60^o co-latitude. The non-smoothness of the curves is a result of the grid structure, which was plotted with a mesh of 2^o along latitude and 3^o along longitude (corresponding to 3601 points). The concentric circles correspond to the co-latitudes of 1^o, 20^o, 30^o, 40^o, 50^o and 60^o, respectively. The positive x axis (radial outward) is upwards (longitude = 0^o) and positive y axis (direction of moon's motion) is to the right (longitude = 90^o). The patterns here are similar to the ones seen in other contours.

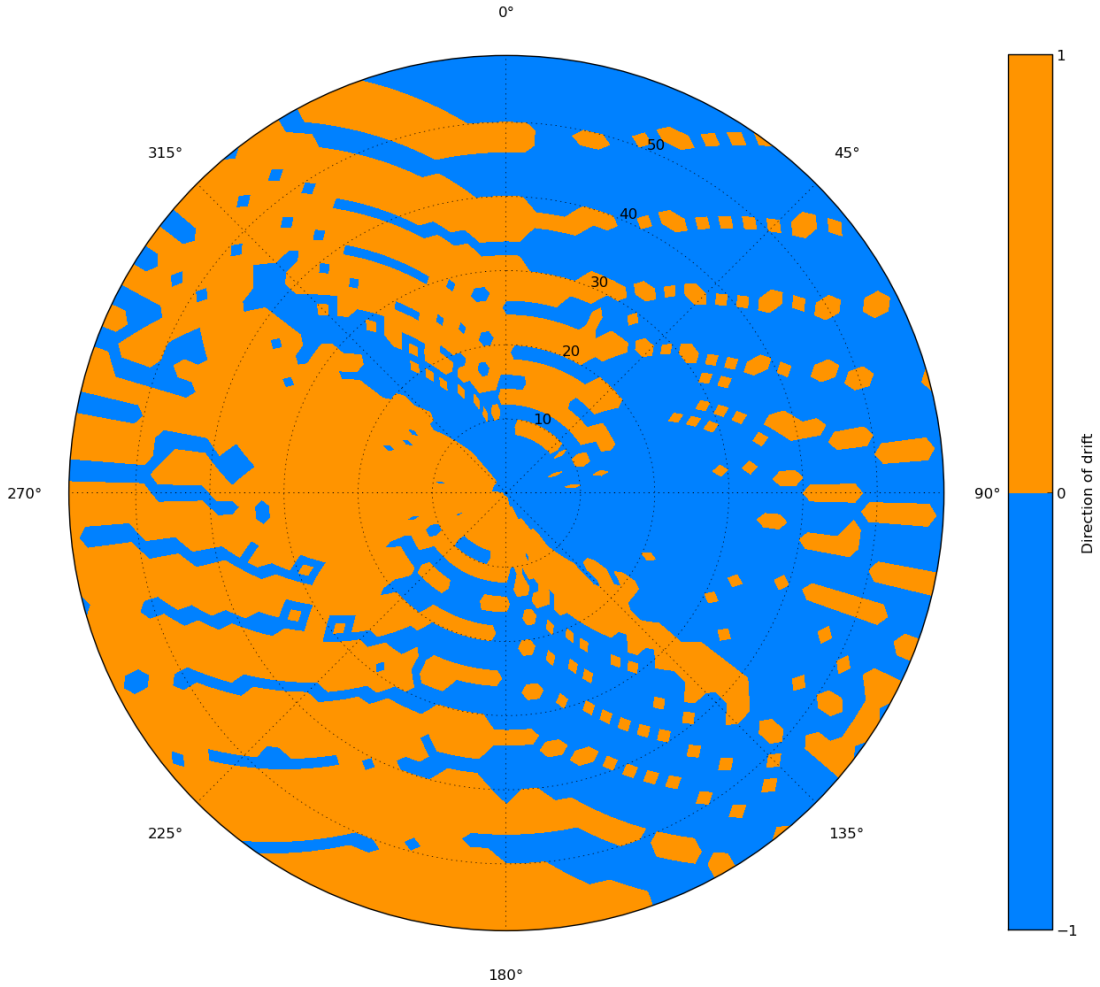

Figure 2.22: Contours of eventual direction of drift of particles for normal launch from various positions in the southern hemisphere of Enceladus out to 60^o co-latitude. The non-smoothness of curve is a result of the grid structure, which was plotted with a mesh of 2^o along latitude and 3^o along longitude (corresponding to 3601 points). The concentric circles correspond to the co-latitudes of 1^o, 20^o, 30^o, 40^o, 50^o and 60^o, respectively. The positive x axis (radial outward) is upwards (longitude = 0^o) and positive y axis (direction of moon's motion) is to the right (longitude = 90^o). The patterns here are similar to the ones seen in other contours. The lighter color represents the trajectories that precess forward with respect to the moon and the darker color represents the trajectories that precess backward.

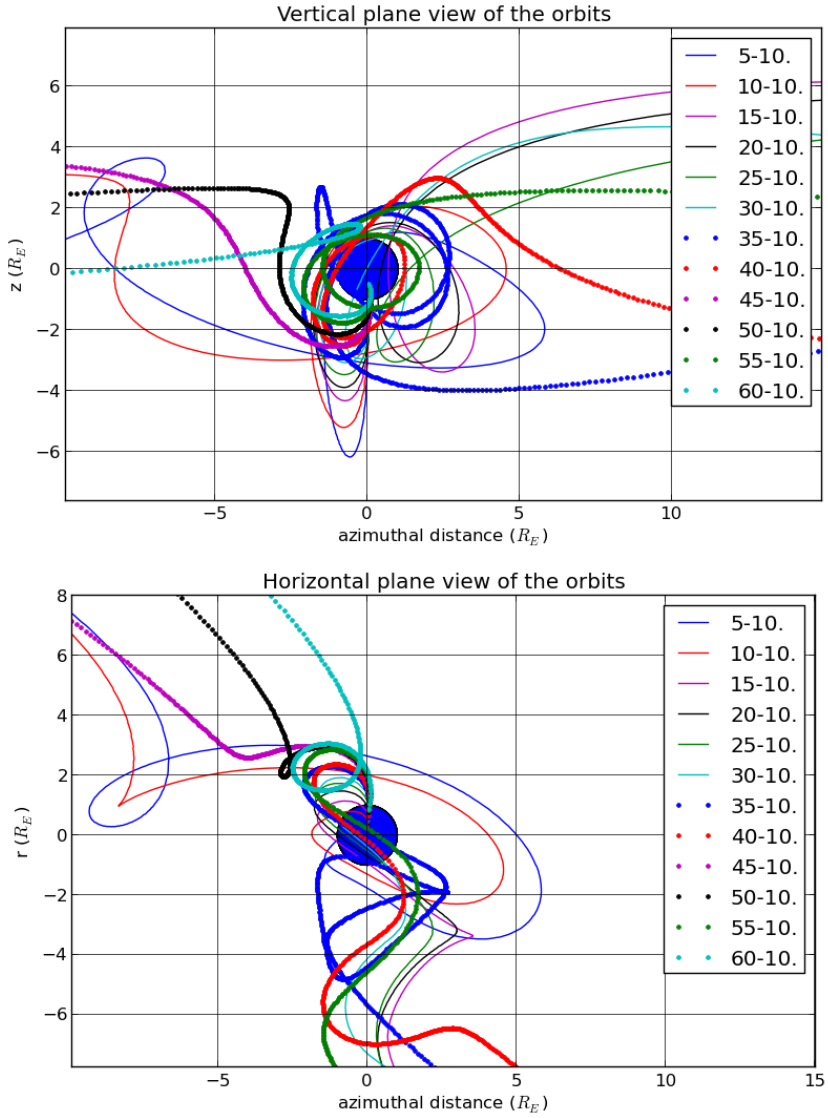

Figure 2.23: Effect of launch co-latitude on trajectories: The evolution of particles starting with the 'cutoff' speed from different co-latitudes in the southern hemisphere (for fixed longitudes of 10^0) - Top: vertical plane, Bottom: horizontal plane. The horizontal axis is the azimuthal distance (in units of the moon's radius). Notice how the orbits change their character with a gradual modification in the co-latitude. These eventually settle into a sinusoidal motion in their orbits around Saturn, drifting away from the moon, owing to different orbital periods.

Launching particles normal to the surface with speeds slightly above cutoff will make them settle into orbits with different orbital inclinations (Fig. 2.20). Any particle on an inclined orbit will reach a maximum possible vertical height of $\sim a_E sin(i)$ away from the equatorial plane on each sides. Figure 2.25 shows this vertical height attainable by a particle in units of Enceladus' radius, plotted vs time. This height is not the actual height of the particle at a general time but computed from the osculating inclination and semi-major axis of the particles. Thus, this is the height at which the vertical speed of the particle would be zero and they would spend more time than anywhere else in their orbit. We launch them from various co-latitudes (5^o to 30^o). In each of the plots, the curve for normal launch (0^o launch) from the South pole is shown for reference. The other lines correspond to launches from various longitudes for the given co-latitude. It is apparent that as the co-latitude increases, the inclinations attained by the cutoff particles decrease. This has an interesting implication similar to the previous one: plumes originating from the region away from the South pole will feed particles with lower inclinations to the E ring. The oscillations in some of the curves correspond to the particles which are still near Enceladus and get continuously perturbed by it.

However, the most interesting and surprising observation is the fact that most of the particles settle at maximum vertical displacements of around $4r_E$. Particles spend more of their orbital time at this height as their vertical speeds are zero at this height. This phenomenon is clearly visible from the final maximum attainable 'heights' for the various particles launched at different latitudes and longitudes as shown in Fig. 2.25. This can explain the double-layered structure of the E ring

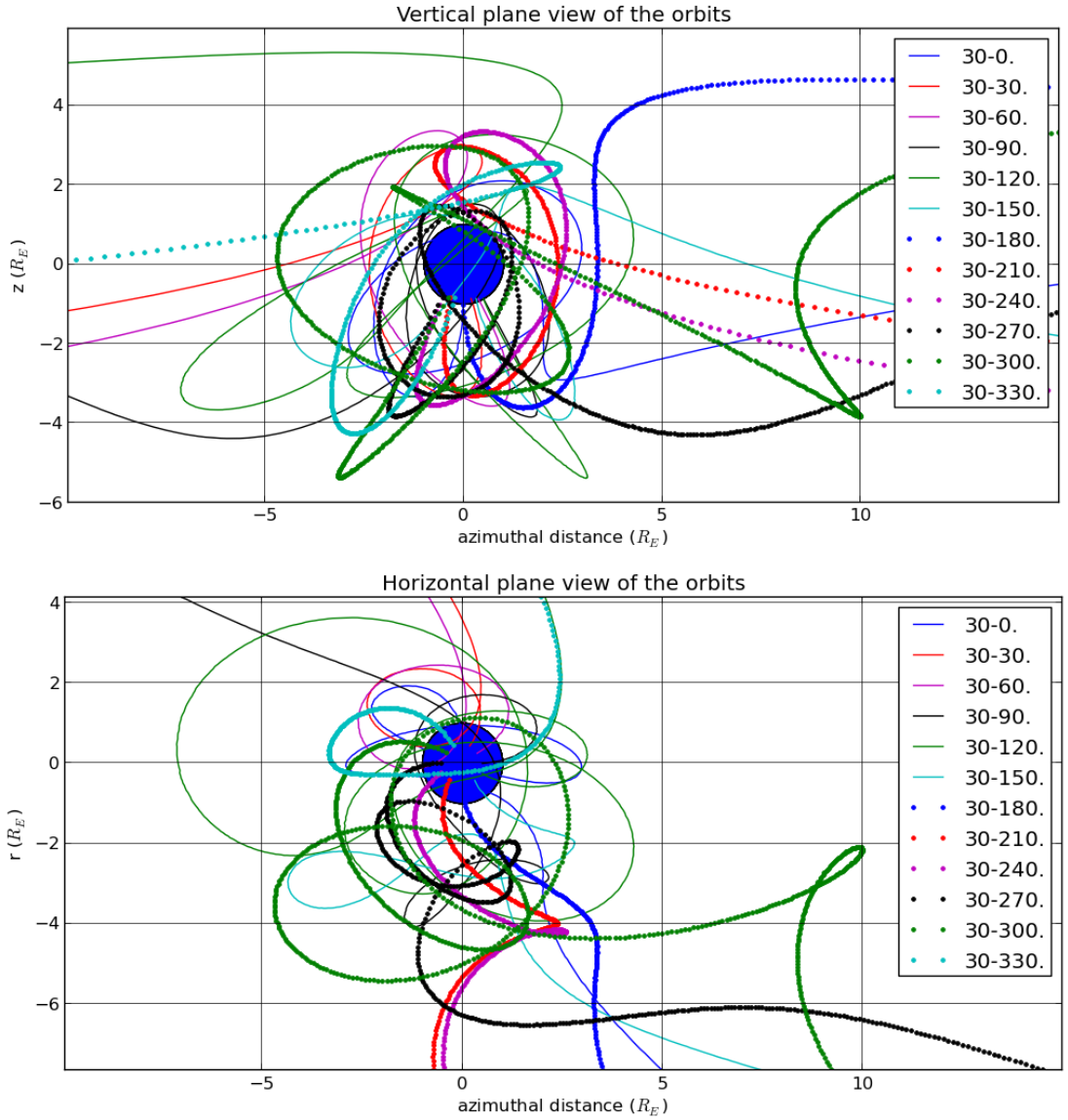

Figure 2.24: Effect of launch longitude on trajectories: The evolution of particles starting with the 'cutoff' speed from different longitudes in the southern hemisphere (for fixed co-latitude of 30^0) - Top: vertical plane, Botton: horizontal plane. The horizontal axis is the azimuthal distance (in units of the moon's radius). Notice how the orbits change their character with gradual modification in the longitude. These eventually settle into a sinusoidal motion in their orbits around Saturn, drifting away from the moon according to their orbital periods.

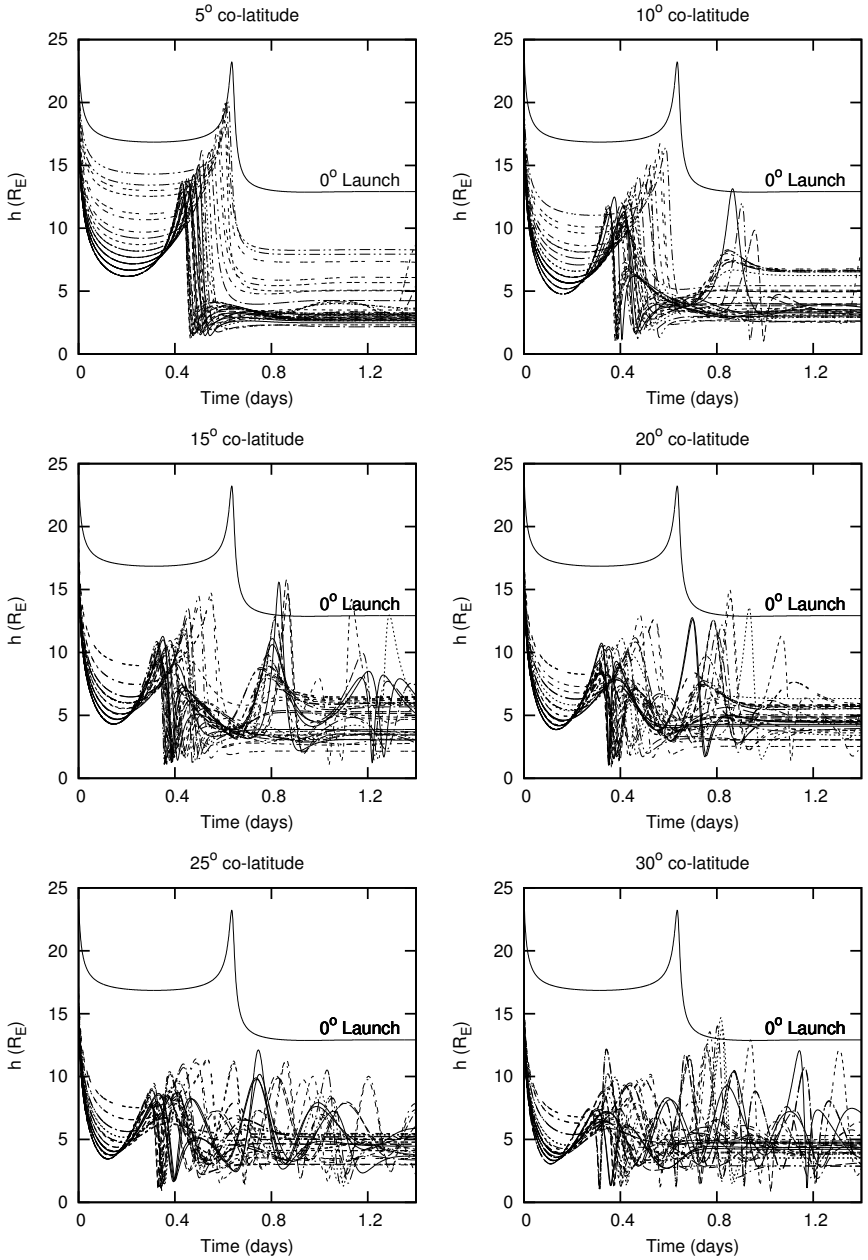

Figure 2.25: The maximum possible instantaneous vertical displacement h (with respect to equatorial plane) possible for a particle ($= ia_E$) during its orbit around Saturn, in units of Enceladus' radius plotted vs time for co-latitudes: 5^o, 10^o, 15^o, 20^o, 25^o and 30^o. Various curves correspond to different launch longitudes (0^o to 350^o with spacing of 10^o) for the given co-latitude. The oscillations are due to close encounters with Enceladus. The particles spend a larger amount of their orbital time at this height as their vertical speeds are zero there [Horanyi et al., 1992]. In each of the panels, the history for vertical launch from the South pole is shown for reference. The oscillations seen in the curves depend on how many close encounters a particle undergoes before escaping the vicinity of the moon. One critical observation is the fact that most of the particles settle at heights of about $4r_E$, irrespective of their cutoff speeds. This is likely to be the primary cause of E-ring's double-layered structure. This phenomenon is emplaced, essentially immediately, within Enceladus' orbital period.

(see Figs. 2.1 and 2.2). Particles barely above the escape velocity (that are most numerous among those that escape) attain this specific inclination which is manifested as the double-layered structure of the E ring. The primary mechanism is the change of energy in the initial launch and a few subsequent close encounters. In this process the signatures of the initial velocities and launch locations are pretty much lost, i.e., the initial velocity and launch cannot be inferred from the particle's current state in the ring. The launch positions of the particles decide the cutoff velocity but the preferred inclination at which the particles settle is only fixed after the close encounters. The fact that most of the particles, away from the South pole settle at around this height ($4r_E$) (see Fig. 2.25), which corresponds to half of the distance between the two layers of E ring suggests that this mechanism produces the structure. The contour of vertical amplitude at equilibrium for different longitudes and co-latitudes can be seen in Fig. 2.26. We can see a 'bean-shaped' region around the South pole from which 'cutoff' particles settle in orbits corresponding to maximum heights equal to approximately the Hill radius of the moon.

We also investigate the effect of plumes being situated at a few selected spots on the southern hemisphere [Spitale and Porco, 2007]. We plot the contour of vertical amplitudes again with a finer mesh (1^o in co-latitude and longitude) near the South pole (Fig. 2.27(Top)). This time we superimpose the eight hot-spots of plume activity as described in Spitale and Porco [2007]. This view, again, shows the southern hemisphere with the moon's velocity towards right and Saturn down. Notice that we only consider normal launch and no tilt with respect to the surface. It is interesting to note from the previous contour (Fig. 2.26) that from a circular region just outside the 30^o co-latitude circle, escape is relatively easier to form the

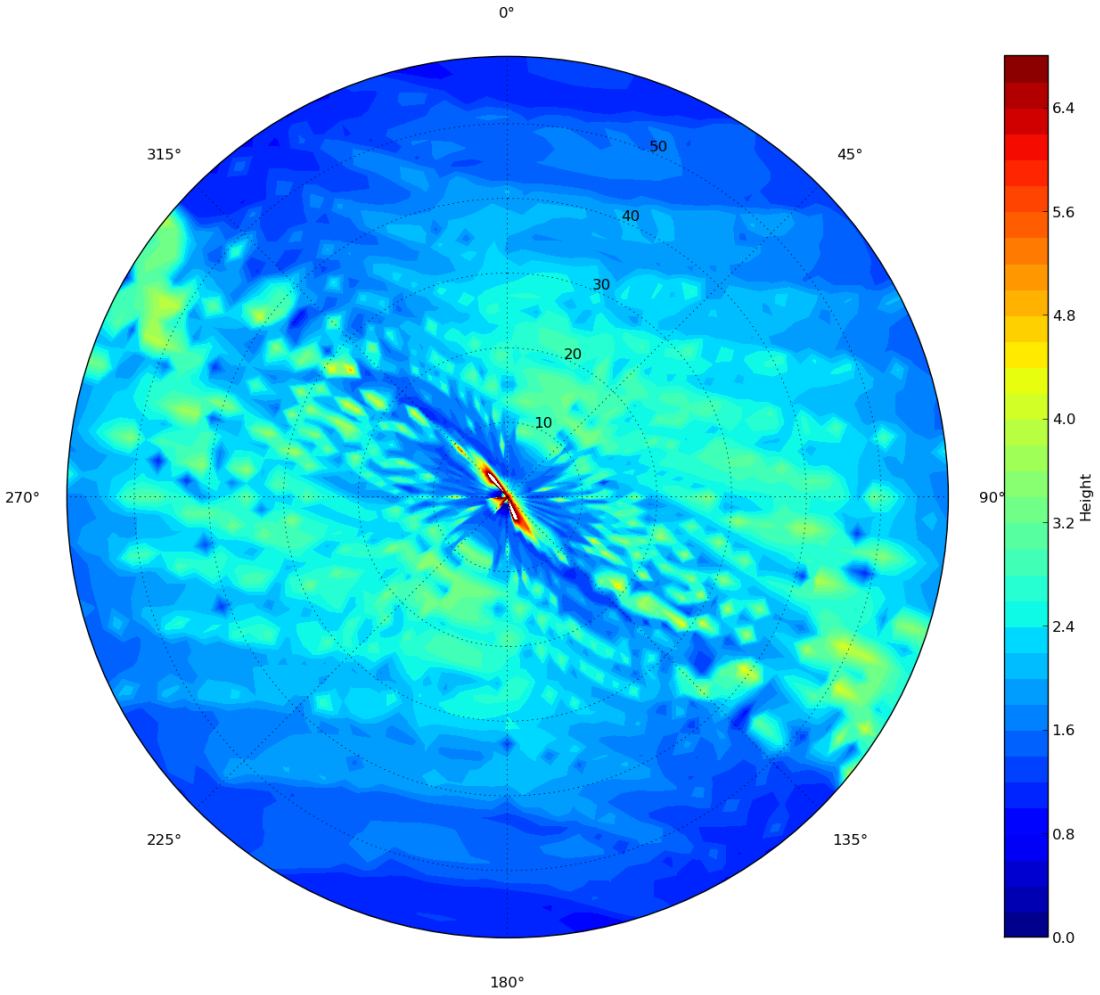

Figure 2.26: Contour for the amplitude of vertical oscillations of particles in equilibrium, launched with cutoff velocities from different latitude and co-longitudes from the southern hemisphere of Enceladus. Notice the 'bean-shaped' region around South pole where the escape is easier (lower cutoff velocities) and many of the particles settle in orbits corresponding to maximum heights approximately equal to the Hill radius of the moon.

double layer. Unfortunately, no active plume spots reside in that circular region, as described next.

The location for easy escape shown in these figures has little correspondence to the 'tiger stripes'. Figure 2.27 (bottom) compares the actual image of the South pole with the map produced. The concentric circles correspond to the 5^o, 10^o, 15^o, 20^o and 25^o co-latitudes from the South pole. It is probably a coincidence that the direction of the stripes matches the pattern produced with the map, but it is very noticeable. Half of the active vents lie close to the spots of relatively easy escape. In this sense the plumes are "lucky" to be near spots where they can feed the ring easily (with lowest speeds). We will present the "actual" simulation of the 'real' plumes in Sec. 6.

2.4.4 Patterns in the contours

The contours presented in the last section show some noteworthy patterns that we will now explain. Looking at Figs. 2.18, 2.20, 2.21, 2.22 and 2.26, we see three prominent patterns:

- P1: Near the circular pericenter, some slanted patterns run at a slight downward incline from the horizontal direction,
- P2: Around the South pole bands emanate radially out, all around, and
- P3: At the pole a $\sim -45^o$ (counter-clock wise) inclined pattern is present.

We describe them one by one here, concentrating on the initial conditions and dynamical factors that relate to these structures.

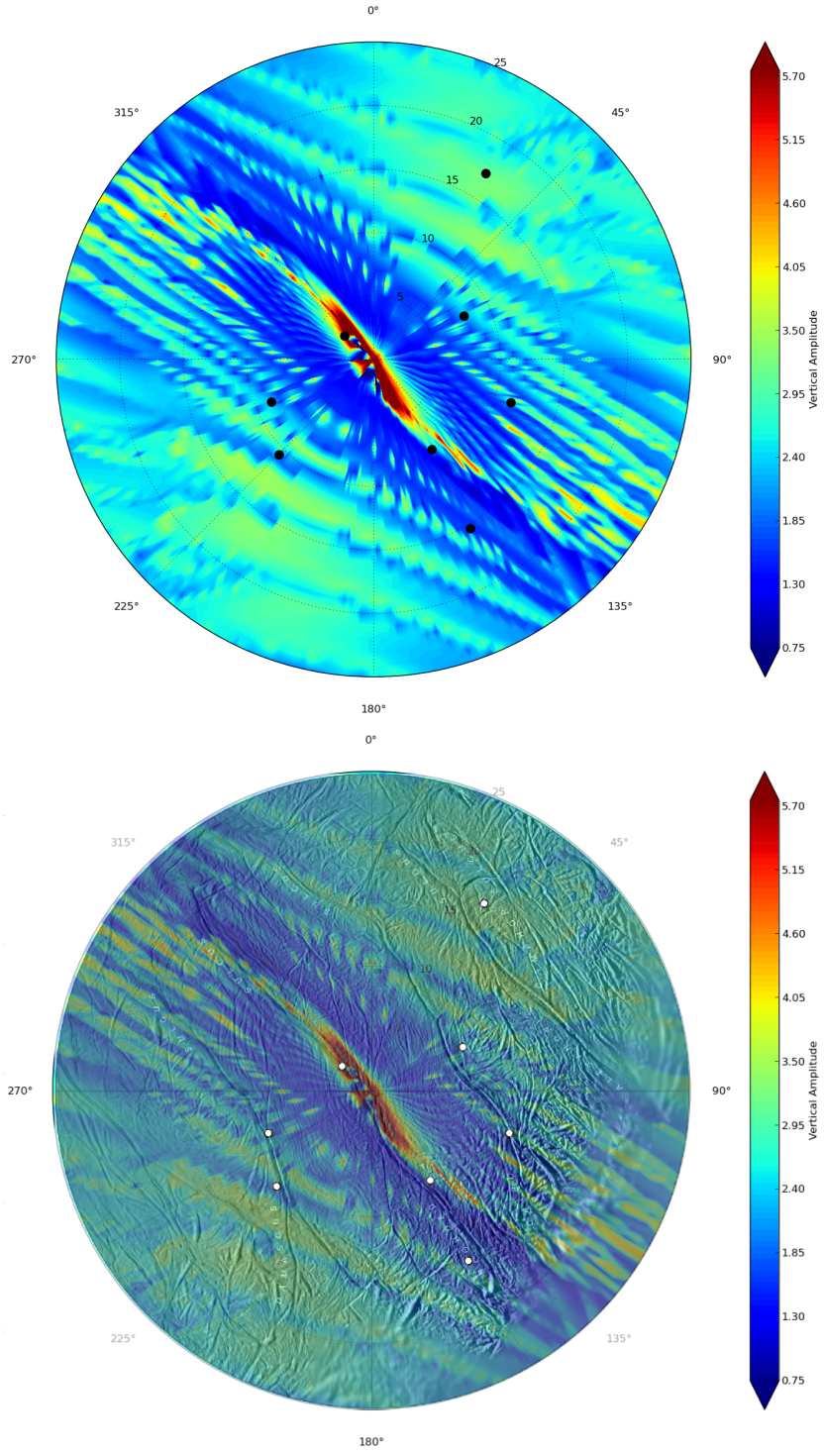

Figure 2.27: Top: The contours of vertical amplitudes that appears when a tighter mesh (1^o both in co-latitude and longitude) is used. Bottom: Easier escape occurs in the following area: the outer circular edge corresponds to the 25^o co-latitude from the South pole. The black dots (top) and white dots (bottom) show the positions of the eight 'real' heaviest plume-activity spots [Spitale and Porco, 2007].

In Fig. 2.28 we show the contour plots of the South pole for the cutoff speeds for normal launch from the southern hemisphere. The four subplots show the situation for Enceladus at different semi-major axis (with associated physical variables like orbital velocity and time period, etc., changing accordingly). To concentrate on the outer bands we truncate the upper speed to $1.02v_{esc}$ in each of these subplots. The first natural thing to notice is that the further away the moon (Enceladus) is from the central mass (Saturn), the contour becomes more uniform because the range of cutoff speeds shrinks. This can be seen from the lower scales in each of these subplots. When the moon is placed at 10 times the real semi-major axis distance, we see the cutoff speeds are in a small range around $1v_{esc}$, which should be intuitively equivalent to an isolated moon case. More importantly, we can see that when the semi-major axis is half the real value, the outer bands approach almost horizontal, while when the moon is at ten times the real semi-major axis, they gradually change to vertical bands (corresponding to Pattern P1). There are other features emanating at the South Pole which overlay the outer pattern, but we will discuss them later.

When the moon is near the central body, tidal forces are most effective. Hence, points on the moon's surface are equivalent (in terms of cutoff speed from the surface) in a horizontal direction (direction of motion of the moon, as seen on the contour plots). Whereas when far away, tidal forces are relatively immaterial and the direction becomes more important. As we can see in Fig. 2.28 (10a: ten times the real semi-major axis) the forward end has higher cutoff speed than the back-facing end, because particles launched from the back-end can fall off the moon easily where as the particles starting from the front-facing end have to escape the

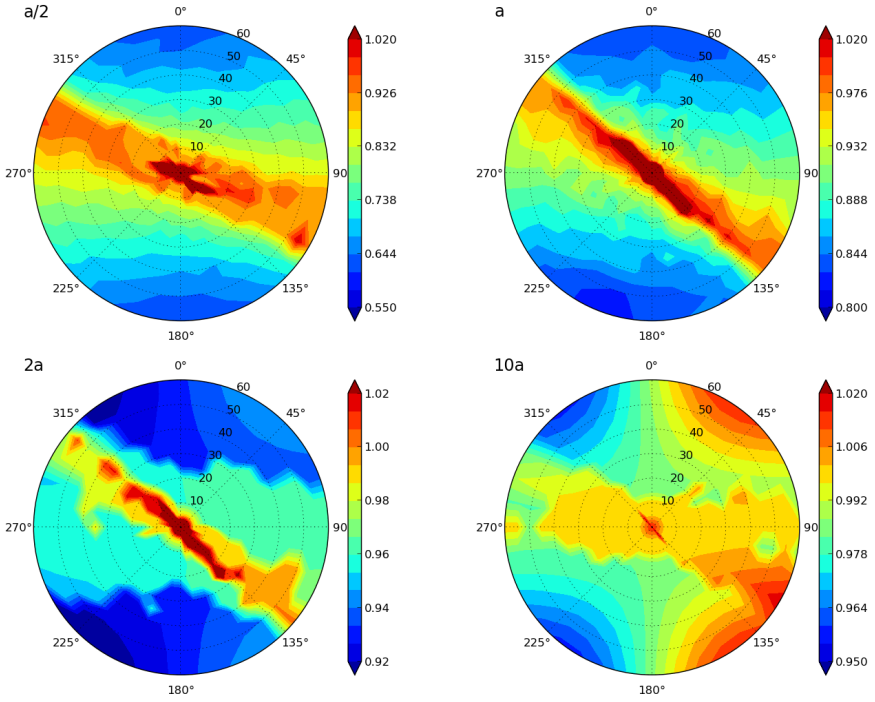

Figure 2.28: Contours of cutoff speeds for normal launch from Enceladus at different semi-major axes. As usual, the moon moves to the right and the radial outward direction is up, while we look directly at the South pole.

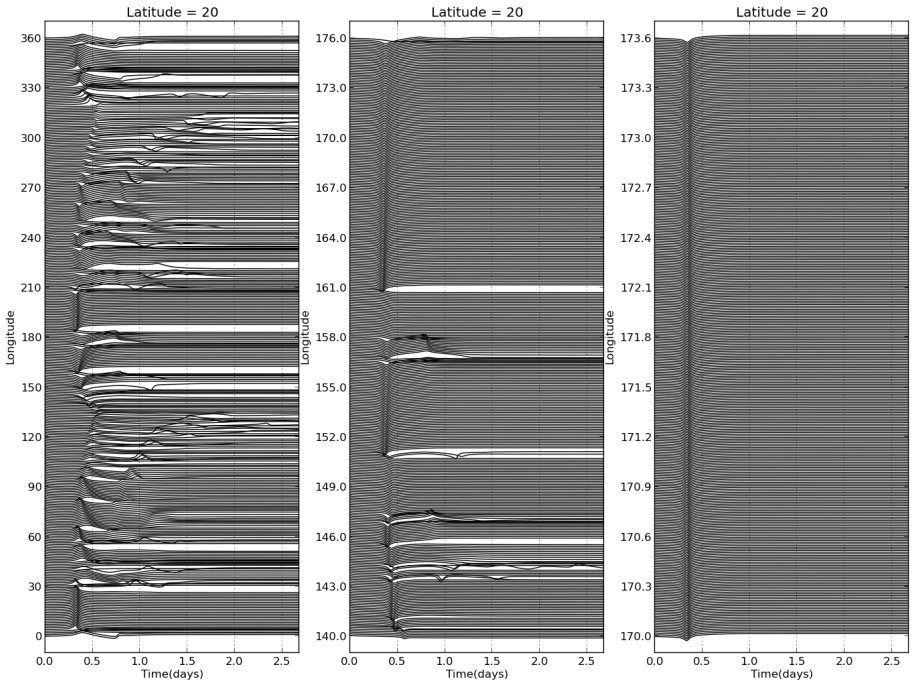

Figure 2.29: These are plots of semi-major axis versus time for the particles starting with cutoff speeds from different longitudes for a fixed co-latitude of 20^o. The plots are displaced by a small but equal amount to look at the changes in the orbital patterns of the particles. The middle plot expands a small region from the left plot. And the right is the further magnification of a small region from the middle plot. A white band will appear when there has been a sudden change in the cutoff speed or dynamics of close encounter. These bands appear all over and represent the ridges we see as described in the second pattern (P2). The figure also shows a 'wedge' at around 135^o and 315^o, corresponding to the third pattern (P3).

whole moon before falling off (for a backward escape, which is more common as seen in the last section).

To account for the second pattern (P2) of bands emanating in all directions from the South pole, we look at the initial dynamics of the orbits starting in the South polar region. Figure 2.29 (left) shows the semi-major axis of various particles plotted against time, for first two orbital periods. These particles start with

the cutoff speeds at the indicated longitude. The co-latitude is fixed at 20^o. We displace these orbits along the vertical axis slightly, to look at the gradual change in the pattern that occurs in the orbits of these particles. We see some white bands all over the longitudes. These correspond to the positions where the orbital character changed suddenly with respect to its neighboring particles - because of the change in the geometry of close encounters with the moon. These white gaps correspond to what we see in the contour plots as bands emanating in all directions from the South pole (P2). Furthermore, we see 'wedge' shapes near 135^o and 315^o. These correspond to the third pattern (P3) as we noted above. When we zoom into these longitudes in Fig. 2.29 - middle and right, the pattern does not self replicate itself at lower magnifications. This is a manifestation of the simple but inherently non-linear problem we are dealing with.

If we repeat this exercise at other latitudes (Fig.2.30), similar patterns arise, establishing these white bands (change in the character of orbits) as the reason from the second pattern (P2).

Finally, let's investigate the third pattern in the contours (P3) - the one in the vicinity of South pole. Figure 2.31 shows semi-major axis plotted against time for particles starting with cutoff speed at different co-latitudes for a fixed longitude (55^o and 145^o). We clearly see that at the lower co-latitudes the first encounter takes more time for the orbits starting with longitude 145^o. This corresponds to the fact that in that direction (145^o longitude), the cutoff speeds are higher as the particle spends more time in its orbit before encountering the moon. This again corresponds to type of close encounter these particles undergo with the moon, based on their initial conditions and geometry. Also, it is noteworthy that these

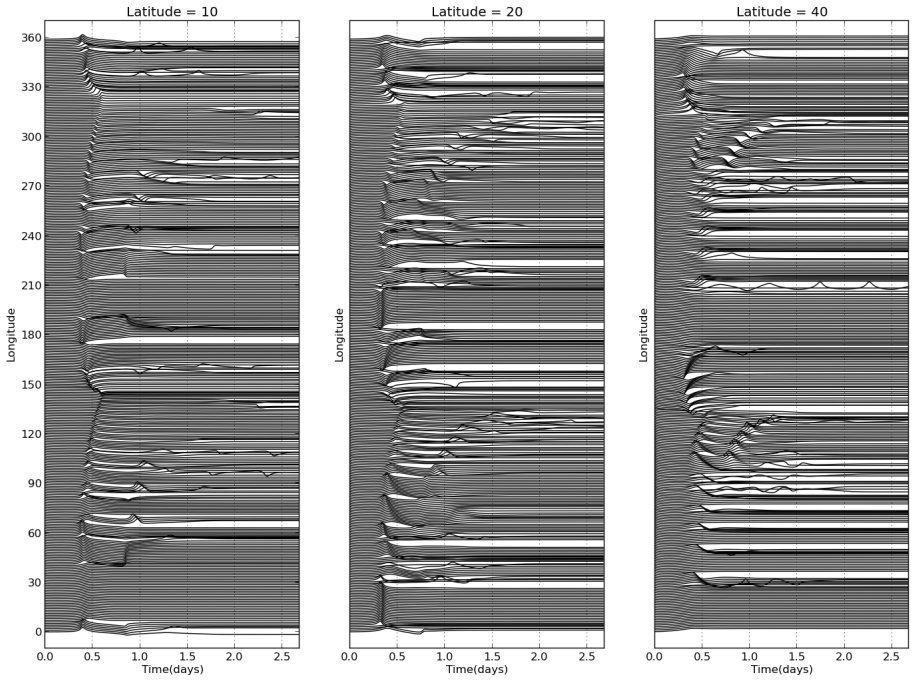

Figure 2.30: Similar to Fig. 2.29, we see similar 'white band' patterns at other latitudes too. These correspond to the second pattern (P2) we listed in the start of Sec. 2.4.4.

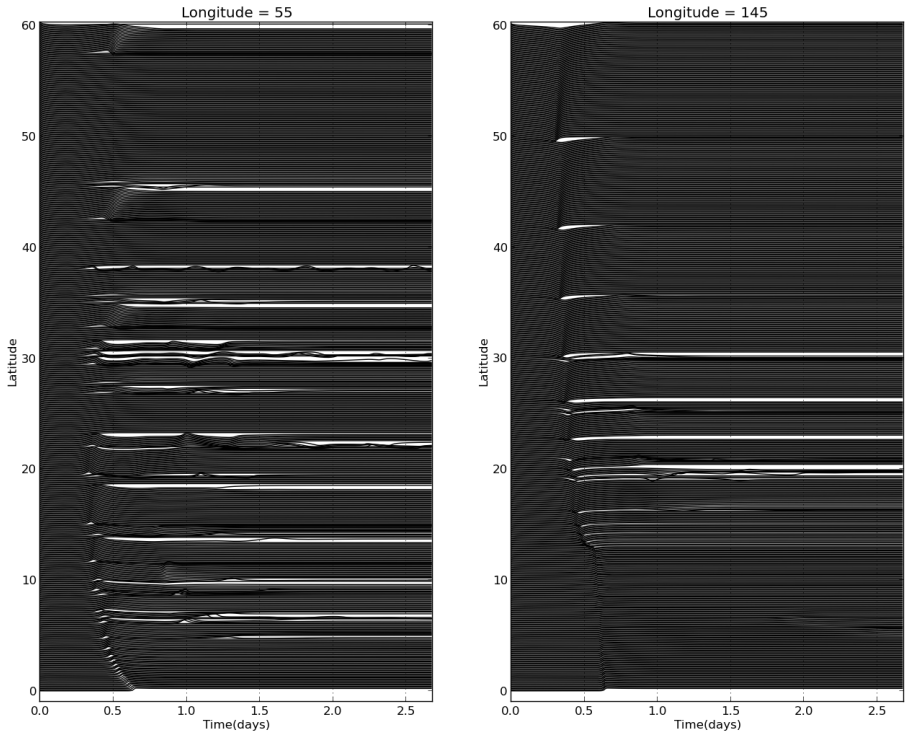

Figure 2.31: Similar to the previous figures (Fig. 2.29 and 2.30), this plot shows the variation in orbits along a fixed longitude when we change the co-latitude. Particles starting near the pole at longitude of 145^o take longer to encounter the moon and hence have higher cutoff speeds, which gets manifested as the third pattern (P3) we listed at the start of Sec. 2.4.4.

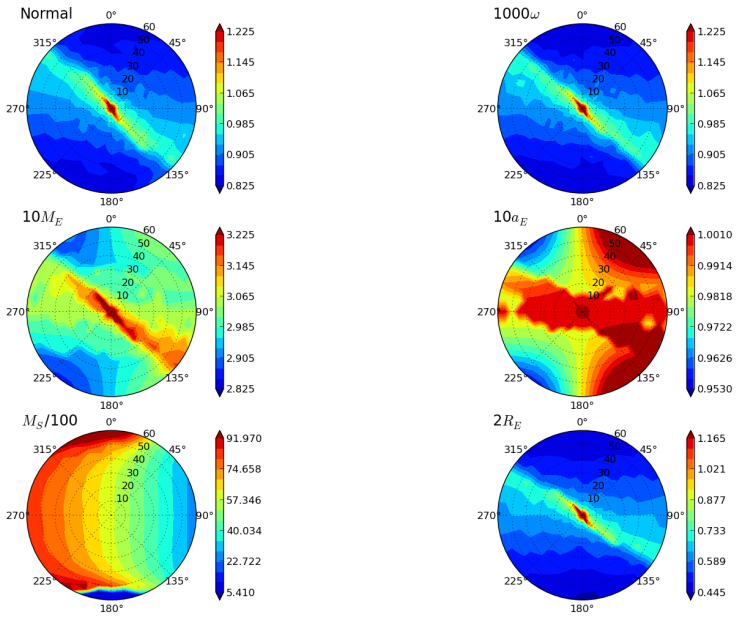

Figure 2.32: Six different experiments with parameters of the system changed (Left - normal, ten times Enceladus' mass, one hundredth Saturn's mass. Right - Thousand times Enceladus' spin, ten times Enceladus' semi-major axis, two times Endeladus' radius). When the mass of Saturn is decreased by a factor of 100, the pattern around the pole disappears.

plots have fewer 'white bands' that were present in other launch comparisons (Fig. 2.29 and 2.30). This implies that the variation owing to longitudes is smoother than the variation owing to co-latitudes.

The third pattern (P3) of slanted lines (corresponding to the longitude of 145^o) running across the plot, near the pole, is mainly because of Saturn's presence. This is seen in Fig. 2.32, which shows six different situations with physical parameters of the system changed to see how the cutoff-speed contours change. When we decrease the mass of Saturn by a factor of 100, the pattern changes drastically around the pole. Further investigations are needed to pin down the exact source of this peculiar pattern. This effect, as noted by Kempf et al. [2010], has been

attributed to the dynamics of the particle in the rotating frame (of Enceladus).

2.5 Analysis of orbits for longer time

Here we consider the dynamics of E-ring particles over longer intervals (100-300 yrs). Particles from the South pole of Enceladus are started with velocities ranging between 0.9-1.9 v_{esc}, launched normally from the surface. In a few simulations we give some lateral speeds too. Again, we do not consider any non-gravitational forces, but only gravity and Saturn's oblateness [Kempf et al., 2008, 2010]. We investigate the time history of the orbital elements of these particles and comment qualitatively about the particle spatial densities in the ring. We will also show that gravitational forces may explain the radial spread of the gaussian core of the E ring [Hedman et al., 2012].

2.5.1 Lifetime of particles

Figure 2.33 shows the survival rate of particles for a given initial speed of launch (with initial velocities consisting of both normal (0.9-1.9 v_{esc}), tangential and radial components (-0.5 to +0.5 v_{esc})). All components are randomly distributed with speeds picked from a constant probability distribution. As the launch speed increases, a greater fraction of particles survives. Figure 2.33 shows that the survival plateaus at about $1.4v_{esc}$ approximately the same as the critical 'cutoff speed' that was obtained previously. Two factors play roles here. First, once a particle has speed above the 'cutoff speed' it escapes to form the E-ring population. This graph would have been a step function if the particles were launched purely normal

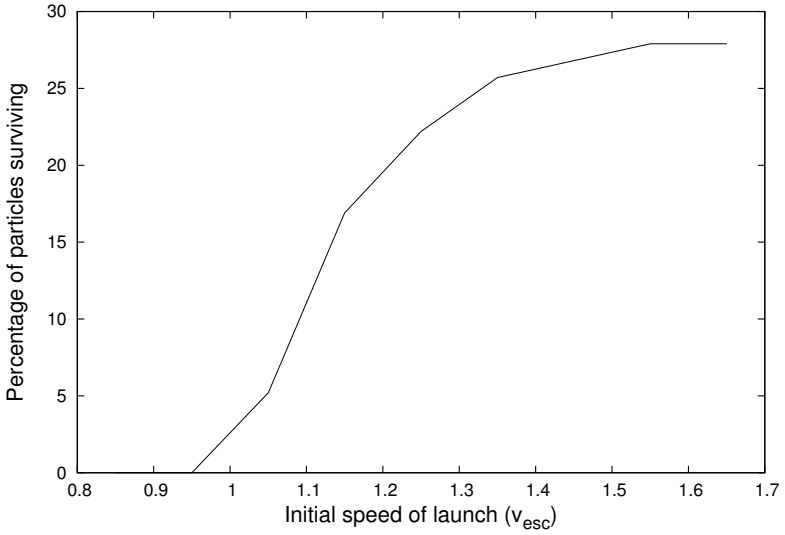

Figure 2.33: Particles remaining after 200 years of evolution as a function of initial launch speed from the South pole. In these simulations the initial velocity was also given some tangential and radial components (see text).

to the surface at the South pole. The plot is continuous because of the radial and tangential velocities given to the particles, which of course is more realistic. This effect is produced because the particles' orbital periods change due to the radial and tangential components of velocities, which also affect the 'cutoff speeds'. Second, the higher the particle's speed, the greater are the chances that the particle will remain away from the moon to avoid quick collisions. Though the particles cross the orbital plane two times per orbit, the higher speeds remove the particles from the moon's Hill sphere and Saturn's oblateness induces differential drift and orbital period changes; thus, higher-speed particles are more likely to miss the moon during ring-plane crossing during the first few opportunities. Also, gravitational focussing is less effective at higher speeds. Hence, over longer time scales, after the system is "stirred", collisions occur a probabilistic chance events, leading to exponential decay (Fig. 2.4).

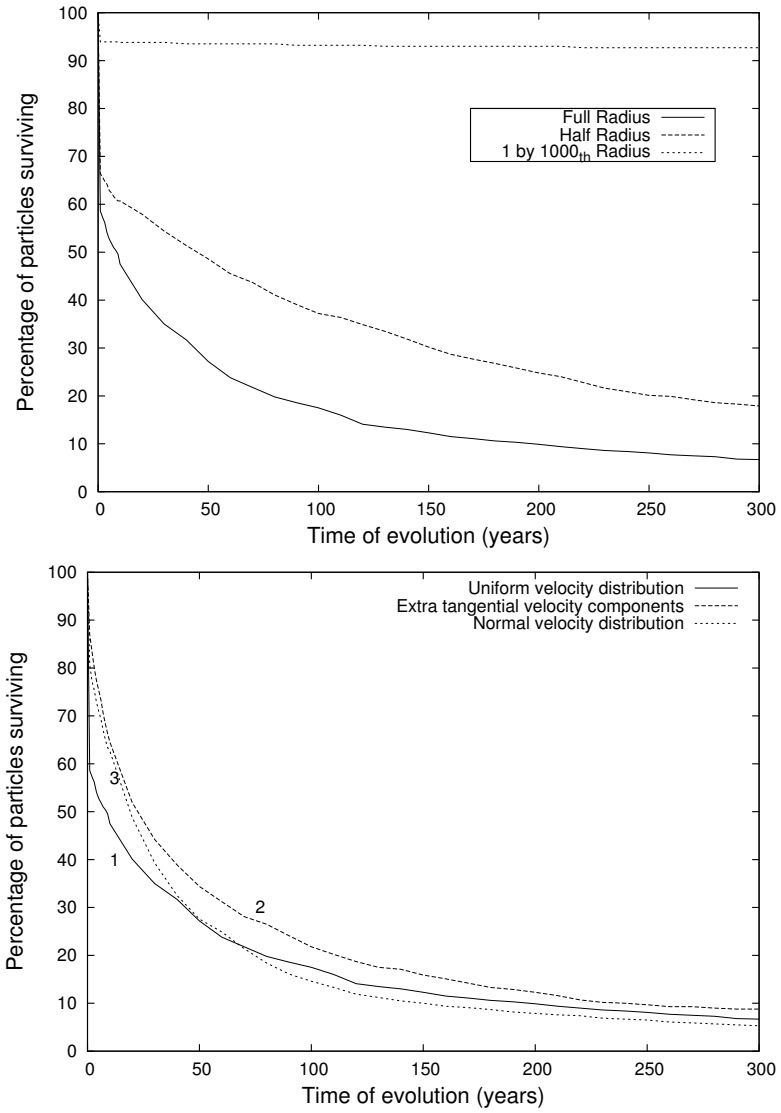

Figure 2.34: Top: Particles remaining as a function of time. The curves correspond to the case of full radius, half radius and 1/1000th radius of Enceladus. The initial transient drop associated with all of the curves occurs through immediate re-collisions within the first few orbital periods. Bottom: Loss of particles for three different initial conditions: Curve 1: Particles are initially launched normal to the South pole with random speeds uniformly distributed between $0.9 - 1.9 v_{esc}$. Curve 2: In addition to the conditions for curve 1, tangential and radial random velocities are added, uniformly distributed between -0.5 to $+0.5 v_{esc}$. Curve 3: These velocities are normally distributed about $1.4 v_{esc}$ with a standard deviation of $0.3 v_{esc}$, along with uniformly distributed tangential and radial velocities between $-0.5 v_{esc}$ to $0.5 v_{esc}$. Subsequently all have exponential decay.

Figure 2.34 shows the result of simulations carried out for longer times for the E-ring particles. In these particular simulations, we start with 1000 particles with velocities varying between $0.9v_{esc}$ to $1.9v_{esc}$, launched from the South pole normal to the surface. We show the percentage of surviving particles as a function of time. Curves 1, 2 and 3 correspond to the results, when the full radius of the moon was assumed (the distinction among 1, 2 and 3 is explained in the caption). Apart from that, we have results for the cases when we take half the radius and one-thousandth of the radius. The $r_{enc}/1000$ case corresponds to the effect of a point mass moon on the ring. A small drop in the plot is due to the finite, but small, radius of the test moon.

The transient decays in all three cases in Fig. 2.34. This corresponds to the initial loss of particles, including those that do not escape and those that collide with the moon during the first few encounters. The figure shows a dramatic drop in the particles surviving once the radius is increased from $0.001r_{Enc}$ to $0.5r_{Enc}$, and even fewer survivors with the actual radius. Once the transient phase is over, the remaining particles populate the gaussian core of E ring. Particle numbers still decay, because a fraction continue to collide with the moon over a longer timescale (the collision time scale with the moon $\sim$ 100 years; see Eq. 2.3). In reality, particles are also lost out of the gaussian core because of non-gravitational forces [Hamilton and Burns, 1994, Burns et al., 2001, Horányi et al., 2008]. Hence, if the E ring is long-lived and maintains its present spatial density, then the South-pole plumes at Enceladus must supply the material at a rate that balances this decay and other losses to maintain any possible equilibrium. The interesting corollary is that, though the ring core itself is presumably old, most particles in the ring core are no more than 100-300 years old but are being continuously replaced by

the newer ones introduced at the plumes [Burns et al., 2001]. This, obviously, assumes that the only loss mechanism of E-ring particles is collisions with the moon; this requires the minimum possible supply rate, and neglects the loss of particles through non-gravitational evolution, sublimation, etc. [Burns et al., 2001] from the system, as well as fragmentation of particles. Particles that come back and collide with the moon, possibly at high relative velocity, provide impact ejecta, and can supply new particles to the ring [Hamilton and Burns, 1994].

Figure 2.34 (Bottom) depicts the behavior of different initial velocity distributions. Curve 1 shows the percentage of surviving particles when the particles are launched normally with initial speeds varying uniformly between $0.9v_{esc}$ to $1.9v_{esc}$. For curve 2, we add a tangential component of velocity uniformly distributed between $-0.5v_{esc}$ to $0.5v_{esc}$. Curve 3 shows the percentage of survivors when the particles are launched with normally distributed (Gaussian) speeds of launch with a mean $1.4v_{esc}$ and a standard deviation of $0.3v_{esc}$, along with uniformly distributed tangential and radial velocities between $-0.5v_{esc}$ to $0.5v_{esc}$. An initial tangential velocity makes the transition state vanish. This is plausible and can be explained as follows:

Imparting a tangential component of the velocity changes the particle's orbital period considerably. Hence these particles, which ultimately oscillate in the z direction do not find the moon there to collide with, on the next pass through the ring plane. This is different from those particles that are not given an additional tangential velocity. Hence, if the initial speed is low, these particles are destined to re-collide with the moon in the first encounter. Therefore, particles that have a tangential component of the velocity will be more likely to feed the ring, as also

seen in the analysis for briefer times. The other major result visible in this plot is the fact that, after 100 years of evolution, curves 1, 2 and 3 become almost indistinguishable. This implies that the close encounters with the moon modulate the signatures of the initial velocity distribution of the particles in the ring. In other words, the close encounters scatter particles until relative velocities are determined by those encounters, rather than by the initial conditions [Gladman et al., 1996].

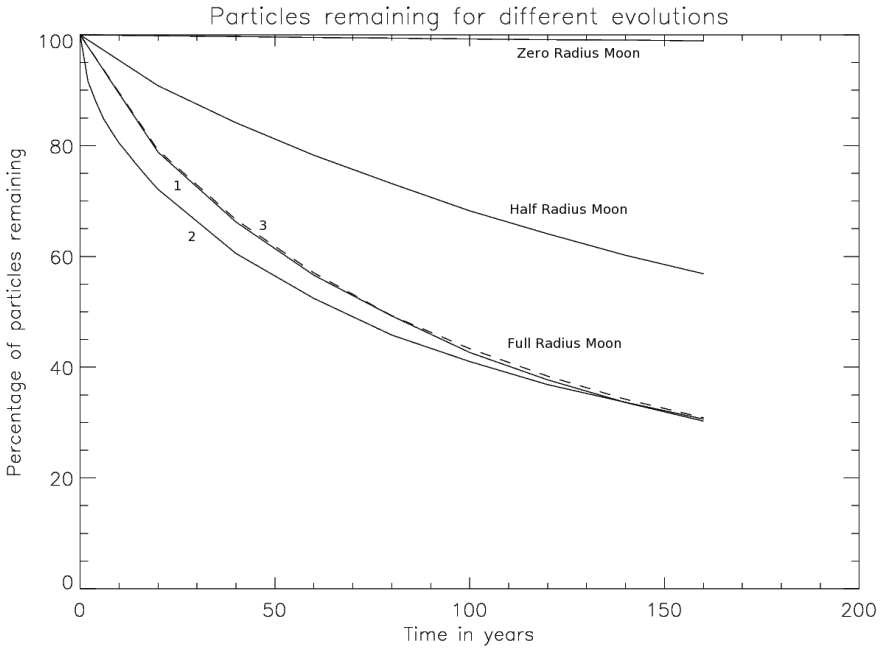

Figure 2.35: Particles remaining after 200 years of evolution for a given initial launch velocity for the mass of moon $1/10^{th}$ of the real moon. This figure is similar to Fig. 2.34, except for the absence of the initial dramatic loss.

Let us now look into the effect of mass change of the moon on the dynamics. We do the same simulation with the mass of the moon $1/10^{th}$ of the actual value. The first realization is the universal disappearance of the transient loss. The moon has lost gravitational influence over the particles so that it is no longer able to hold back particles during the first few encounters. Obviously the escape velocities calculated for the new system are much smaller than the previous case.

2.5.2 Effects of other moons

Other major satellites such as Mimas, Tethys, Dione, Rhea and Titan were incorporated into the system to see if they affect the evolution in any way. No visible effect on the structure of the ring was observed due to them. They play a very minor role in the precession of the particles' orbits and no resonance effect is visible in regions near Enceladus' orbit [Burns and Gladman, 1998].

For an estimate, the acceleration due to Saturn's gravity is $\frac{GM}{r^2} \sim 0.67\ m/s^2$ at Enceladus' orbit whereas Dione's tidal effect is $\frac{2GM_{Dio}\triangle r}{r^3} \sim 2.6 \times 10^{-9} m/s^2$, where $\triangle r$ is the radial distance between Dione's and Enceladus' orbit. The latter effect is clearly negligible.

2.5.3 Effect of other forces

Apart from gravity, radiation pressure and electromagnetic forces play a very significant roles in the evolution of the overall E ring. They become important for any small (less than 1 μm) particles present in the ring [Burns et al., 2001]. For comparison, Table 4.4 lists the accelerations produced by different forces on a 1-micron-sized particle. It is clear that gravity is the prime-mover in ring dynamics. Oblateness, electromagnetic and radiation forces become important in a longer time-scale analysis (time $\sim$ 1/acceleration). Over shorter time-scales these forces strongly depend on the size of the particles. However, the features near Enceladus' orbit can be explained by gravitational forces alone. Gravity quickly (first few orbits) defines the gaussian halo (the radial and vertical extent in the vicinity of Enceladus) of the E ring. This chapter has analyzed the role of gravitational force

Force Type	**Expression**	**acceleration (m/s^2)**
Point mass gravity	$\frac{GM}{r^2}$	0.67
Oblateness	$\frac{GM}{r^2} J_2 \left(\frac{R_S}{r}\right)^2$	6.9×10^{-4}
Electromagnetic	$\frac{qB}{m}(v + r\omega)$	1.3×10^{-4}
Radiation	$\frac{3J_0 Q_{Pr}}{4\rho c d_s^2 r_g}$	1.8×10^{-5}
Tidal (due to Dione)	$\frac{2GM_{Dio}\triangle r}{R^3}$	2.6×10^{-7}

Table 2.3: Accelerations produced by different forces on a micron-sized particle in the E ring near Enceladus' orbit. q is the charge on the particle ($\sim 3 \times 10^{-16}$ C, maximum possible charge on a 1-micron radius sphere for a given voltage), B is Saturn's magnetic field at distance r (3.6×10^{-7} Tesla), m is the mass of a 1-micron radius spherical particle (10^{-14} kg), v is Enceladus' orbital velocity, ω is Saturn's spin ($\sim 10^{-4}$ rad/sec), J_0 is the unit-less radiation constant for the limit of geometrical optics (1.36×10^3), Q_{P_r} is the non-dimensional radiation pressure coefficient (~ 1), ρ is the particle's density (assumed to be 1000 kg/m^3), c is the speed of light ($\sim 3 \times 10^8$ m/s), d_s is 9.6 (Saturn's distance from Sun in AU), r_g is the radius of particle (1 micron), M_{Dio} is Dione's mass, $\triangle r$ is the radial distance between Dione's and Enceladus' orbits (10^8 m) and R is the semi-major axis of Dione (3.77×10^8 m). Electromagnetic and radiation forces increase strongly at smaller particle sizes.

in the formation of gaussian halo of the double layer.

We did not consider any of these forces in our simulations of E ring core. Since, as we have shown, the double-layer can be explained as a short-term phenomenon, non-gravitational forces apparently have a limited role to play. They, however, are relevant in the longer-term dynamics of the ring, particularly in radially expanding the ring away from the gaussian core [Horányi et al., 2009, Kempf et al., 2010]. We now show simulation results where the vertical and radial extents of the E ring, in the immediate vicinity of Enceladus, are produced solely by gravitation.

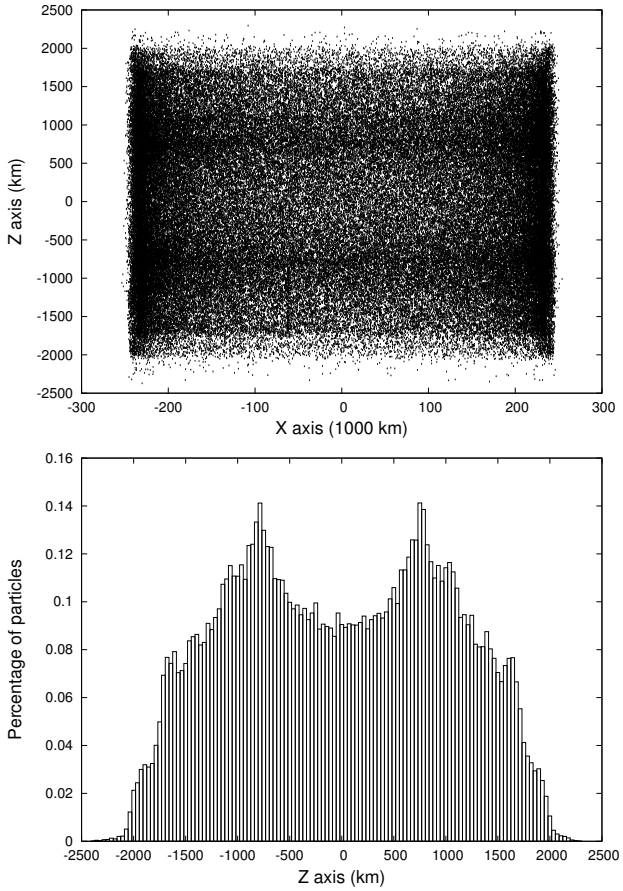

Figure 2.36: Top: Side view of the simulated E-ring core after 1 year (see text for details). The double-layer is apparent here. Bottom: The distribution of particles in the vertical direction in the E-ring after 1 year of simulation. The separation between the two peaks is $\sim$ 2000 km.

2.6 A gravitational model of the E ring

Building upon the insights of the previous section, we now present a unified model of the E-ring core. We combine together all the trajectories from the eight hot spots [Spitale and Porco, 2007] from the southern hemisphere of Enceladus. The particles were started simultaneously from the spots normal to the surface, all at the same time. The velocity was uniformly distributed between $0.8v_{esc}$ to $1.4v_{esc}$. The evolution is for 1 year. To make the model real (i.e., to simulate continuous emission from the plumes around the orbit), we rotate the trajectory of the particles proportional to the time of evolution. We also resample each orbit uniformly in time (per day) to generate more particles with the same initial conditions but lagged in time. This improves the overall density of the ring without affecting the results. This whole sample of particles is the final E-ring core. The side view of the final model is shown in Fig. 2.36 (Top). The double layer is apparent in the model. It corresponds to a width of $\sim 2r_H$, similar to that measured in the observed E ring (Fig. 2.2). The dense concentration at the sides arises because of looking at the ring sideways at the edges [Horanyi et al., 1992]. Also notice that the vertical scale is stretched for clarity.

The percentage of particles as a function of vertical height after 1 year is shown in Fig. 2.36 (Bottom). The dip at the ring plane is apparent, and the distance between the layers is about 2000 km, the same as the observations (Fig. 2.2). The small time interval in which the structure is created indicates that gravitational effects are enough to produce the structure. The simulations also produce the radial halo of the double-layered structure as shown in the onion-peel observations [Hedman et al., 2012]. Figure 2.37 shows the radial excursion of the ring particles. The particles have a radial extent of about 10,000 km, of the order of the E ring

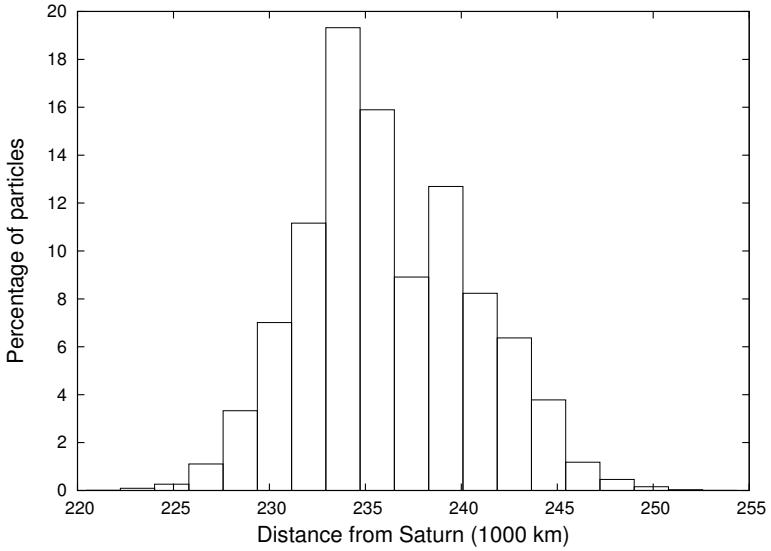

Figure 2.37: The radial distribution of particles in a 1-yr E-ring simulation. The radial extent of the ring is about 10,000 km (inwards and outwards) from the orbit of Enceladus ($\sim$ 238,000 km). This is caused by the change in semimajor axis of the particles in the first few close encounters with the moon (Fig. 2.11). There are fewer particles at the radial position of the moon, because they collide with the moon in the simulation. This dynamics happens quickly, all under gravitational forces alone. The observed dip we see is due to the short simulation time.

double-layered core [Hedman et al., 2012]. This suggests that the bulk of the E-ring core is the result of a local gravitational effect. Further radial diffusion occurs owing to other forces [Horányi et al., 2008, Kempf et al., 2010].

2.7 Conclusions

We have described how the particles in the E-ring core near Enceladus' orbit evolve over two sets of time-scales, a few orbits and $\sim$ 200 yrs. We conclude that

- The immediate vertical and radial structure of the E-ring core are outcomes of a very small time-scale phenomenon - close encounters during the launch in first few orbital periods.
- The launch velocities from the southern hemisphere in general (for normal launch) causing the double-layered structure are of the order of 0.86 to 0.9 times the escape velocity.
- Gravity is the central player in the short-term structures seen in the E-ring core.
- At longer time-scales ($\sim$ 100 yr.), the ring core is replenished by the geysers at Enceladus; typical particles have an age of about 100-300 years (upper limit).

CHAPTER 3

THE MATHEMATICS OF RESONANCE

In celestial mechanics an orbital resonance occurs when two orbiting bodies exert regular, periodic gravitational influences on each other, because their orbital periods are close to a ratio of two small integers. Because Saturn's rings extend across more than $1R_S$, the orbital periods of ring particles range almost continuously from ∼5 hr (D ring) to ∼14 hr (outer A ring), meaning that resonance phenomena are ubiquitous across the Saturnian ring system. These resonances can be stable or unstable: an unstable resonance will drive away particles and create gaps, while a stable resonance can reinforce the configurations of moons and ring particles.

In this chapter we will derive the expressions for the disturbing function and other quantities related to the phenomenon of resonance. The disturbing function is the perturbing potential (i.e., its gradient equals a force or acceleration) causing a mass' orbit to deviate from a simple Keplerian orbit. We will express that potential as a function of the orbital elements of the two masses. We will follow Murray and Dermott [1999] closely, but will elaborate on material that is not in that book.

3.1 The disturbing function

We start with a central planet of mass M_c. In our applications we usually have an external satellite of mass m' which perturbs an (internal) test particle of mass m, both of which orbit the central (more massive) planet (Fig. 3.1). We develop the expressions of the disturbing functions for each of the small masses.

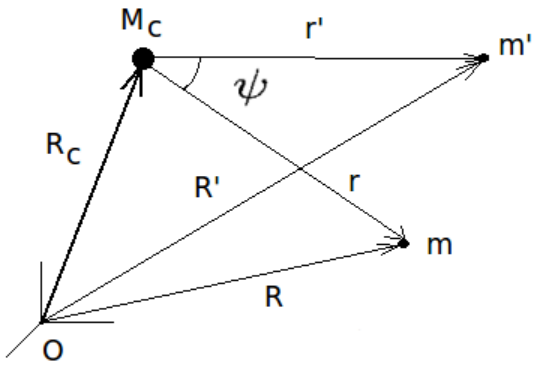

Figure 3.1: Three-body setup

Relative to an inertial coordinate system with origin O, we have $\overrightarrow{R_c}$ = the position vector of the central planet, $\overrightarrow{R'}$ = the position vector of the exterior mass, $\overrightarrow{R}$ = the position vector of the interior mass, $\overrightarrow{r'} = R' - \overrightarrow{R_C}$ = the position vector of the exterior mass relative to the central planet and $\overrightarrow{r} = \overrightarrow{R} - \overrightarrow{R_C}$ = the position vector of the interior planet relative to the central mass. The same terms without the overhead arrows express the magnitude (length) of the corresponding vectors:

$$r' = \sqrt{x'^2 + y'^2 + z'^2} \tag{3.1}$$

and

$$r = \sqrt{x^2 + y^2 + z^2}, \tag{3.2}$$

where x, y, z are the coordinates of the internal mass with respect to the central planet and x', y', z' are the coordinates of the external mass with respect to the central planet. The magnitude of the position vector of the exterior mass with respect to the interior mass, $\overrightarrow{r'} - \overrightarrow{r}$, is given by

$$|\overrightarrow{r'} - \overrightarrow{r}| = \sqrt{(x' - x)^2 + (y' - y)^2 + (z' - z)^2}. \tag{3.3}$$

Applying Newton's gravitational law for the central, interior and exterior masses,

the equations of motion are

$$\ddot{\overrightarrow{R_c}} = Gm\frac{\overrightarrow{r}}{r^3} + Gm'\frac{\overrightarrow{r'}}{r'^3}, \tag{3.4}$$

$$\ddot{\overrightarrow{R}} = Gm'\frac{\overrightarrow{r'} - \overrightarrow{r}}{(r'-r)^3} - GM_c\frac{\overrightarrow{r}}{r^3}, \tag{3.5}$$

and

$$\ddot{\overrightarrow{R'}} = Gm\frac{\overrightarrow{r} - \overrightarrow{r'}}{(r-r')^3} - GM_c\frac{\overrightarrow{r'}}{r'^3}; \tag{3.6}$$

overhead double dots represent second derivatives with respect to time and G is the universal gravitational constant. Taking the differences of the suitable equations above to find the equations of motion of the two masses with respect to the central mass, we get

$$\ddot{\overrightarrow{r}} + G(M_c+m)\frac{\overrightarrow{r}}{r^3} = Gm'\frac{\overrightarrow{r'} - \overrightarrow{r}}{|\overrightarrow{r'} - \overrightarrow{r}|^3} - Gm'\frac{\overrightarrow{r'}}{r'^3} \tag{3.7}$$

and

$$\ddot{\overrightarrow{r'}} + G(M_c+m')\frac{\overrightarrow{r'}}{r'^3} = Gm\frac{\overrightarrow{r} - \overrightarrow{r'}}{|\overrightarrow{r} - \overrightarrow{r'}|^3} - Gm\frac{\overrightarrow{r}}{r^3}. \tag{3.8}$$

The left-hand sides of the equations are just the classical two-body problem equation for each particle. The right-hand sides consist of the perturbation terms. Converting the force terms into potentials, we have

$$\ddot{\overrightarrow{r}} - \nabla U = \nabla D, \tag{3.9}$$

and

$$\ddot{\overrightarrow{r'}} - \nabla' U' = \nabla' D', \tag{3.10}$$

where the gradients ∇ and ∇' are

$$\nabla = \hat{i}\frac{\partial}{\partial x} + \hat{j}\frac{\partial}{\partial y} + \hat{k}\frac{\partial}{\partial z}, \tag{3.11}$$

$$\nabla' = \hat{i}\frac{\partial}{\partial x'} + \hat{j}\frac{\partial}{\partial y'} + \hat{k}\frac{\partial}{\partial z'}, \tag{3.12}$$

and the potentials are

$$U = \frac{G(M_c + m)}{r}, \tag{3.13}$$

$$U' = \frac{G(M_c + m')}{r'}, \tag{3.14}$$

$$D = \frac{Gm'}{|\overrightarrow{r'} - \overrightarrow{r}|} - Gm' \frac{\overrightarrow{r} . \overrightarrow{r'}}{r'^3} \tag{3.15}$$

and

$$D' = \frac{Gm}{|\overrightarrow{r'} - \overrightarrow{r}|} - Gm \frac{\overrightarrow{r} . \overrightarrow{r'}}{r^3}. \tag{3.16}$$

D and D' are called the interior and exterior disturbing functions, respectively, and are each composed of a "direct" and an "indirect" part. The terms containing dot products are the indirect parts. They arise because the central planet experiences accelerations due to each of the other two masses, which indirectly affect the two smaller masses. This term is zero in the case when system's center of mass is chosen as the origin.

Introducing n = the mean motion (i.e., the average angular velocity) of the unperturbed interior mass about the central mass, n' = the mean motion of the unperturbed exterior mass, a = the semimajor axis of the reference orbit ($G(M_c + m) = n^2 a^3$) of the internal mass, a' = the semimajor axis of the reference orbit ($G(M_c + m') = n'^2 a'^3$) of the exterior mass, $\alpha = \frac{a}{a'}$, $\mu = Gm$ and $\mu' = Gm'$ in the equations and specifying the direct (R_D), the exterior (R_E) and the interior (R_I) parts of the disturbing function, we obtain

$$D = \frac{\mu'}{a'} R_D + \frac{\mu'}{a'} \alpha R_E \tag{3.17}$$

and

$$D' = \frac{\mu}{a'} R_D + \frac{\mu}{a'} \frac{1}{\alpha^2} R_I, \tag{3.18}$$

$$R_D = \frac{a'}{|\overrightarrow{r'} - \overrightarrow{r}|}, \tag{3.19}$$

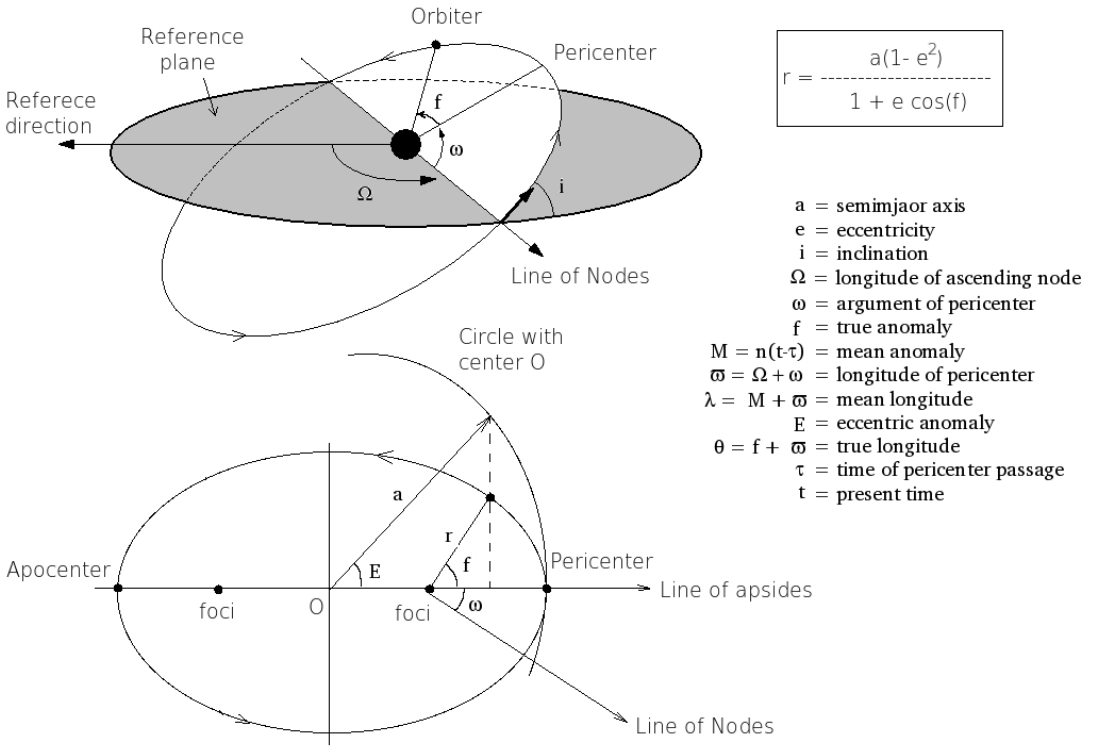

Figure 3.2: Orbital elements of an elliptical orbit around a central mass.

$$R_E = -\left(\frac{r}{a}\right)\left(\frac{a'}{r'}\right)^2 cos\psi, \tag{3.20}$$

and

$$R_I = -\left(\frac{r'}{a'}\right)\left(\frac{a}{r}\right)^2 cos\psi, \tag{3.21}$$

where ψ is the angle between the radius vectors (r and r') of the two masses with respect to the central mass, M_C (Fig. 3.1).

We will use the Saturn-Mimas-Methone system to illustrate our formulation. The ratio of the masses is $10^{13} : 10^6 : 1$ (see Ch. 4). Clearly, Saturn and Mimas dominate Methone and are hardly affected by its perturbations. Also the center of mass of the system will lie almost at Saturn's center. Hence, in our case, both R_E and R_I are zero because we choose the center of mass of the system as the origin of the coordinate system. We now outline the expansion of R_D but, for full details,

see Murray and Dermott [1999, pp. 228-233]. By the law of cosines,

$$|\overrightarrow{r'} - \overrightarrow{r}|^2 = r^2 + r'^2 - 2rr'cos\psi. \tag{3.22}$$

When expanding the disturbing function as a power series, the following identity, which exploits the use of Legendre polynomials, is utilized

$$\begin{aligned}
\frac{1}{|\overrightarrow{r'} - \overrightarrow{r}|} &= \frac{1}{r'}\left[1 - 2\frac{r}{r'}cos\psi + \left(\frac{r}{r'}\right)^2\right]^{-\frac{1}{2}} && (3.23)\\
&= \frac{1}{r'}\left[1 + \frac{r}{r'}cos\psi + \left(\frac{r}{r'}\right)^2\left(\frac{3cos^2\psi - 1}{2}\right) + O\left(\frac{r}{r'}\right)^3\right] && (3.24)\\
&= \frac{1}{r'}\sum_{l=0}^{\infty}\left(\frac{r}{r'}\right)^l P_l(cos\psi), && (3.25)
\end{aligned}$$

where $P_l(x)$ is the l^{th}-order Legendre polynomial with argument $cos\psi$. Notice that the constant terms have been removed from the above expressions because when they are part of a potential, they will not contribute any force as they do not survive differentiation. Now we need to write the angle ψ in terms of the orbital elements of the two masses, which will result in the final series expansion. That is, we want

$$R_D = \mu' \sum f(a, a', e, e', i, i')cos\phi, \tag{3.26}$$

where

$$\phi = j_1\lambda' + j_2\lambda + j_3\varpi' + j_4\varpi + j_5\omega' + j_6\omega, \tag{3.27}$$

in which λ' = the mean longitude of the exterior mass, λ = the mean longitude of the interior mass, ϖ' = the longitude of pericenter of the exterior mass, ϖ = the longitude of pericenter of the interior mass, ω' = the argument of pericenter of the exterior mass and ω = the argument of pericenter of the interior mass (see Fig. 3.2), and the j_i are integers such that

$$\sum_{i=1}^{6} j_i = 0. \tag{3.28}$$

This so-called d'Alembert relation follows from the azimuthal invariance of the primary's potential (since the perturbing potential cannot depend on the orientation of the coordinate system). By finding the exact form of the function f in Eq. 3.26, we can pick out the dominant (constant or slowly varying) terms and the combination of angles that describes the resonance. The first step is to express the angle ψ in terms of the orbital variables. By doing a Taylor expansion and using Laplace coefficients [Izsak, 1963], we can write a series expansion of the disturbing function [Murray and Dermott, 1999, pp. 233-248]. When the time periods of the two masses are in a simple integer ratio of a:b, the order of the resonance is defined as $|a - b|$. We need to retain all significant terms in the expansion for numerical accuracy. As an example, the resonance between Enceladus and Pallene is third-order and hence we need at least a third-order expansion. By contrast, in the cases of Anthe-Mimas and Methone-Mimas, we can just keep the first-order terms of the expansion because these resonances are first-order.

The terms in the disturbing function expansion are of three types - secular ($D^{(sec)}$), resonant ($D^{(res)}$) and short-period ($D^{(sho)}$):

$$R_D = D^{(sec)} + D^{(res)} + D^{(sho)}. \tag{3.29}$$

Any argument (the angular terms for sines and cosines) that does not involve mean longitudes is constant or slowly varying and can give rise to secular terms (i.e., long-period). Occasionally, the time-varying terms may be canceled due to a commensurability between the two mean motions (or, equivalently, the two corresponding orbital periods). We classify these arguments as resonant terms. Because of the dependence on semimajor axis, these terms are localized while secular terms represent global effects. Any other argument is classified as short-period. These latter terms integrate to zero over longer times, according to the

averaging principle [Murray and Dermott, 1999, p. 293]. That is, after averaging,

$$< R_D >=< D^{(sec)} > + < D^{(res)} > . \tag{3.30}$$

We now proceed to classify the types of resonances that occur in ring systems and derive some analytical results.

3.2 Types of resonances related to Saturn's rings

A central point mass induces a classical closed Keplerian ellipse for a particle orbiting around it (disregarding the parabolic and hyperbolic open orbits). Generally, the central planets are oblate and thus other (higher order) perturbations are present. These additional perturbations change the orbital shape. One can consider the modification to the body's orbit as being perturbed by oscillations about the three directions - orbital, radial and vertical, like three simple harmonic oscillators acting simultaneously. These three frequencies (the mean motion, n; the radial frequency, κ; and the vertical frequency, ν) are given by Murray and Dermott [1999, p. 268]:

$$n^2 = \frac{1}{a}\left(\frac{\partial V}{\partial r}\right)_0, \tag{3.31}$$

$$\kappa^2 = \frac{3}{a}\left(\frac{\partial V}{\partial r}\right)_0 + \left(\frac{\partial^2 V}{\partial r^2}\right)_0, \tag{3.32}$$

$$\nu^2 = \frac{1}{a}\left(\frac{\partial V}{\partial r}\right)_0 + \frac{1}{a^2}\left(\frac{\partial^2 V}{\partial \alpha^2}\right)_0, \tag{3.33}$$

where a is the semimajor axis of the unperturbed orbit, α is the angle of the particle's position vector at a given instant from the equatorial plane (inclination with the equatorial plane) and the subscript 0 denotes that the partial derivative is evaluated at $r = a$ and $\alpha = 0$.

The major geometric consequence of these oscillations is that the orbit, in general, is no longer closed. The extent to which the rates of the radial and vertical excursions (i.e., those due to the eccentricity and the inclination) differ from n is a measure of the rate of change of the pericenter and the node, respectively. Hence,

$$\dot{\varpi} = n - \kappa \tag{3.34}$$

and

$$\dot{\Omega} = n - \nu. \tag{3.35}$$

A perturbing satellite will, of course, introduce its own set of frequencies n', κ' and ν', given by the same equations with a replaced by a'. The satellite's potential can be expanded in the same manner as the expansion presented in the last section. For each argument in the expansion (the angular terms inside the cosines), the pattern speed Ω_p is defined as the angular frequency of a reference frame in which this argument is stationary. In other words, it is the time derivative of the time-dependent terms for a given argument. The general form of Ω_p is [Murray and Dermott, 1999, p. 482]

$$s\Omega_p = sn' + k\kappa' + p\nu', \tag{3.36}$$

which, using expressions equivalent to Eq. 3.34 and 3.35, becomes

$$s\Omega_p = (s + k + p)n' - k\dot{\varpi}' - p\dot{\Omega}', \tag{3.37}$$

where s, k, and p are integers and s is non-negative. This gives rise to three types of resonances.

- **Corotation Resonance**: This occurs when the integer multiple of the difference between s and Ω_p is zero, i.e.,

$$s(n - \Omega_p) = 0. \tag{3.38}$$

Substituting the value of sΩ_p from Eq. 3.37, we get

$$(s + k + p)n' - sn - k\dot{\varpi}' - p\dot{\Omega}' = 0. \tag{3.39}$$

The integral of the left-hand side of this equation should be zero or near zero for a corotation resonance. Integrating with respect to time and using the definition for the mean longitude λ = nt + ϖ, we get the expression for the resonance argument of a corotation resonance,

$$\varphi = (s + k + p)\lambda' - s\lambda - k\varpi' - p\Omega'. \tag{3.40}$$

The above expression shows that the longitude of pericenter (ϖ) and the longitude of ascending node (Ω) of the perturbed particle are not involved in corotation resonances. Since only the mean longitude appears, this would imply (from the perturbation equations) that only the semi-major axis of the perturbed particle would be affected by this resonance.

- **Lindblad Resonance**: This occurs when an integer multiple of n-Ω_p is equal to the natural frequency of radial oscillations of the perturbed particle, κ, i.e.,

$$s(n - \Omega_p) = \pm\kappa, \tag{3.41}$$

where the upper and lower signs correspond to inner and outer Lindblad resonances, respectively. Following the line of argument for a corotation resonance, we can derive the resonance argument for a Lindblad resonance as

$$\varphi = (s + k + p)\lambda' - (s \mp 1)\lambda - k\varpi' \mp \varpi - p\Omega'. \tag{3.42}$$

The Lindblad resonance has no terms related to the longitude of ascending node (Ω) of the perturbed particle, implying that only semi-major axis and eccentricity of the perturbed particle are affected by this resonance.

- **Vertical Resonance**: This resonance occurs when the integer multiple of n-Ω_p is equal to the natural frequency of vertical oscillations of the perturbed particle, ν, i.e.

$$s(n - \Omega_p) = \pm s\nu, \tag{3.43}$$

where the upper and lower signs correspond to inner and outer vertical resonances, respectively. Again, following a similar formulation to that before, we can write the resonance argument for the vertical resonance as

$$\varphi = (s + k + p)\lambda' - (s \mp 1)\lambda - k\varpi' \mp \Omega - p\Omega'. \tag{3.44}$$

A vertical resonance affects both the semi-major axis and the inclination of the perturbed particle.

3.3 Sample Calculations

We will now present a sample calculation using the expressions for the disturbing functions provided in Murray and Dermott [1999, pp. 233-248]. Let us take the case of the Methone-Mimas resonance. We must first determine the resonant terms in the fourth-order expansion (to keep all the significant terms, a first-order expansion should suffice but to make comparisons with higher-order terms we evaluate some higher-order terms) of the disturbing function for the Methone-Mimas case and then search for the terms where the resonance argument is librating (i.e., the time-dependent term averages to 0). A resonance argument will be the combination of angles occurring inside the cosine term in the expansion such that $j_1\lambda' + j_2\lambda$ is close to zero. When resonance occurs, these terms are either constant or librate (i.e., oscillate) slightly around some constant value. This argument will identify possible resonances and then we will compare the "strength" of the resonance terms

by ratios of the amplitude of the coefficients of the corresponding cosine terms.

In order to locate the possible resonances, we first take the ratio of the orbital periods of Methone and Mimas.

$$\frac{T_{Methone}}{T_{Mimas}} = \frac{1.009574\ days}{0.942423\ days} = 1.0714 \approx \frac{15}{14}. \tag{3.45}$$

This hints at where to start to look for first-order resonances for this pair of satellites. Accordingly, we search for all the terms of the form $15\lambda_{Methone} - 14\lambda_{Mimas}$ in the expansion of the disturbing function (λ_i = mean longitude of i^{th} moon). Keep in mind that several terms are possible because additional slow-moving angles (e.g., Ω or ϖ) are necessary in order to satisfy the d'Alembert rule (Eq. 3.28). This is a case where the perturber (Mimas) is interior, so we have the expression of the disturbing function as

$$R_D = \sum S_l \, cos(\phi_l), \tag{3.46}$$

where S_l is the strength of the l^{th} term and ϕ_l is its corresponding argument. Table 3.1 gives all the arguments starting with $15\lambda_{Methone} - 14\lambda_{Mimas}$ for the fourth order expansion.

To accurately simulate the orbits of any two moons that are involved in resonance, we would require precise initial conditions for these bodies. So, instead of numerically simulating the orbits, we take the time history of the two moons from the respective NASA kernels [Acton, 1996], which are numerically integrated orbits of the system fitted to observations. Figure 3.3 plots these arguments against time for 22 years. These diagrams show which arguments are, and which are not, librating (i.e., oscillating about some fixed angle). We see four arguments that are

$15\lambda_{Methone} - 14\lambda_{Mimas} - \varpi_{Mimas}$
$15\lambda_{Methone} - 14\lambda_{Mimas} - \varpi_{Methone}$
$15\lambda_{Methone} - 14\lambda_{Mimas} + \varpi_{Methone} - 2\varpi_{Mimas}$
$15\lambda_{Methone} - 14\lambda_{Mimas} - 2\varpi_{Methone} + \varpi_{Mimas}$
$15\lambda_{Methone} - 14\lambda_{Mimas} + \varpi_{Mimas} - 2\Omega_{Mimas}$
$15\lambda_{Methone} - 14\lambda_{Mimas} + \varpi_{Methone} - 2\Omega_{Mimas}$
$15\lambda_{Methone} - 14\lambda_{Mimas} - \varpi_{Mimas} - \Omega_{Methone} + \Omega_{Mimas}$
$15\lambda_{Methone} - 14\lambda_{Mimas} - \varpi_{Mimas} + \Omega_{Methone} - \Omega_{Mimas}$
$15\lambda_{Methone} - 14\lambda_{Mimas} + \varpi_{Mimas} - \Omega_{Methone} - \Omega_{Mimas}$
$15\lambda_{Methone} - 14\lambda_{Mimas} - \varpi_{Methone} - \Omega_{Methone} + \Omega_{Mimas}$
$15\lambda_{Methone} - 14\lambda_{Mimas} - \varpi_{Methone} + \Omega_{Methone} - \Omega_{Mimas}$
$15\lambda_{Methone} - 14\lambda_{Mimas} + \varpi_{Methone} - \Omega_{Methone} - \Omega_{Mimas}$
$15\lambda_{Methone} - 14\lambda_{Mimas} + \varpi_{Mimas} - 2\Omega_{Methone}$
$15\lambda_{Methone} - 14\lambda_{Mimas} + \varpi_{Methone} - 2\Omega_{Methone}$

Table 3.1: Various arguments of Methone-Mimas disturbing function that contain $15\lambda_{Methone} - 14\lambda_{Mimas}$.

librating in Fig. 3.3. We calculate the strengths (by calculating the corresponding S_l of the four librating arguments) to ascertain the dominant resonance present.

Table 3.2 shows the resonance arguments with the corresponding leading terms giving expressions for their strengths and the associated numerical values (calculated in units of specific energy (i.e., per unit mass), since these represent potentials per unit mass).

The terms f_{27}, f_{31}, f_{35} and f_{36} are the strength coefficients as taken from Murray

Resonance argument	Strength term	Value
$15\lambda_{Methone} - 14\lambda_{Mimas} - \varpi_{Mimas}$	$e_{Mimas} f_{27}$	9.56×10^{-2}
$15\lambda_{Methone} - 14\lambda_{Mimas} - \varpi_{Methone}$	$e_{Methone} f_{31}$	4.94×10^{-4}
$15\lambda_{Methone} - 14\lambda_{Mimas} + \varpi_{Methone} - 2\varpi_{Mimas}$	$e^2_{Mimas} e_{Methone} f_{35}$	2.17×10^{-5}
$15\lambda_{Methone} - 14\lambda_{Mimas} - 2\varpi_{Methone} + \varpi_{Mimas}$	$e_{Mimas} e^2_{Methone} f_{36}$	9.43×10^{-8}

Table 3.2: Various arguments of the Methone-Mimas disturbing function that contain $15\lambda_{Methone} - 14\lambda_{Mimas}$, their leading strength terms and the corresponding values in energy per unit mass.

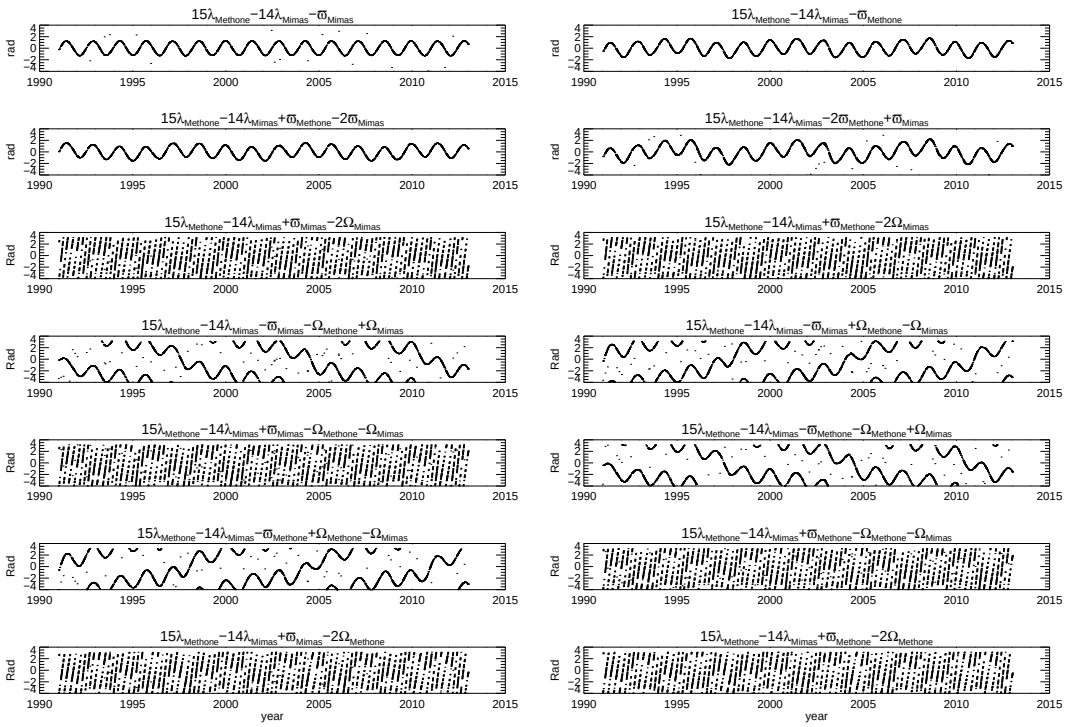

Figure 3.3: Various arguments of the Methone-Mimas disturbing function starting with $15\lambda_{Methone} - 14\lambda_{Mimas}$ that satisfy the d'Alembert relation. The first four arguments librate; their strengths are given in Table 3.2.

and Dermott [1999, pp. 539-556]. They are given by the following expressions

$$f_{27} = \frac{1}{2}\left[-30b_{1/2}^{15} - \frac{\alpha}{2}\, b_{3/2}^{14} - 2\alpha b_{3/2}^{15} + b_{3/2}^{16}\right], \tag{3.47}$$

$$f_{31} = \frac{1}{2}\left[29b_{1/2}^{14} - \frac{\alpha}{2}\, b_{3/2}^{13} - 2\alpha b_{3/2}^{14} + b_{3/2}^{15}\right], \tag{3.48}$$

$$f_{35} = \frac{1}{16}\left[-29264 - 913\alpha\delta + 33\alpha^2\delta^2 + \alpha^3\delta^3\right] b_{1/2}^{16}, \tag{3.49}$$

$$f_{36} = \frac{1}{16}\left[20722 + 653\alpha\delta - 34\alpha^2\delta^2 - \alpha^3\delta^3\right] b_{1/2}^{14}. \tag{3.50}$$

In the above expressions, the Laplace coefficients are defined as

$$b_s^i(\alpha) = \frac{1}{\pi}\int_0^{2\pi} \frac{cosi\psi}{(1 - 2\alpha cos\psi + \alpha^2)^s} d\psi, \tag{3.51}$$

and δ is the differential operator following the rule

$$\delta b_s^j(\alpha) = s\left(b_{s+1}^{j-1}(\alpha) - 2\alpha b_{s+1}^{j}(\alpha) + b_{s+1}^{j+1}(\alpha)\right). \tag{3.52}$$

The value of the strength terms in Table 3.2 clearly shows that the resonance with the argument $15\lambda_{Methone} - 14\lambda_{Mimas} - \varpi_{Mimas}$, the corotation resonance of Methone and Mimas, is the system's most prominent one. The second strongest resonance, the Lindblad resonance of Methone and Mimas, has an argument of $15\lambda_{Methone} - 14\lambda_{Mimas} - \varpi_{Methone}$. In next chapter, we identify and present the prominent resonance arguments for the Anthe-Mimas and Pallene-Enceladus systems.

3.4 Pendulum Model

When a body is in an exact resonance, the sum of the time-dependent terms in the argument is constant. But, in general, these arguments oscillate slightly about their mean values and hence they librate, i.e., the body's motion is similar to that of a pendulum.

The argument of a general cosine term in an expansion is

$$\phi = j_1\lambda' + j_2\lambda + j_3\varpi' + j_4\varpi + j_5\Omega' + j_6\Omega. \tag{3.53}$$

The averaged disturbing functions, with long-period terms integrated out, have the general form [Murray and Dermott, 1999, p. 329]

$$< D >= \frac{Gm'}{a'}\left[D^{(sec)} + e^{|j_4|}e'^{|j_3|}sin^{|j_6|}(i/2)sin^{|j_5|}(i'/2)\left[f_d(\alpha) + f_e(\alpha)\right]cos\phi\right], \tag{3.54}$$

and

$$< D' >= \frac{Gm}{a}\left[\alpha D^{(sec)} + e^{|j_4|}e'^{|j_3|}sin^{|j_6|}(i/2)sin^{|j_5|}(i'/2)\left[\alpha f_d(\alpha) + f_i(\alpha)\right]cos\phi\right], \tag{3.55}$$

where $< D >$ is the averaged disturbing function for an internal resonance and $< D' >$ is for an external resonance. $D^{(sec)}$ is given by

$$\begin{aligned} D^{(sec)} &= \frac{1}{8}(e^2+e'^2)\left(2\alpha D+\alpha^2 D^2\right) b^0_{1/2} \\ &+\frac{1}{4}ee'\left(2-2\alpha D-\alpha^2 D^2\right) b^1_{1/2} cos(\varpi'-\varpi) \\ &-\frac{1}{2}\left(sin^2(i/2)+sin^2(i'/2)\right)\alpha b^1_{3/2} + sin(i/2)sin(i'/2)\alpha b^1_{3/2} cos(\Omega'-\Omega). \end{aligned}$$

The terms $f_e(\alpha)$ and $f_i(\alpha)$ (which contain the sum of various Laplace coefficients) can be found in the Appendix of Murray and Dermott [1999, pp. 539-556]. We will write the appropriate form when presenting our calculations later. When the system is in a resonance, we expect the argument to be nearly constant. We are interested in the time history of ϕ. Does it oscillate or drift? To find this history, we take the time derivative of this and use the fact that $\lambda = nt + \epsilon$, where $\epsilon = \varpi - n\tau$ is the mean longitude of epoch (τ is the time of pericenter passage along the osculating orbit). Thus we get

$$\dot{\phi} = j_1(n'+\dot{\epsilon'}) + j_2(n+\dot{\epsilon}) + j_3\dot{\varpi'} + j_4\dot{\varpi} + j_5\dot{\Omega'} + j_6\dot{\Omega} = 0. \tag{3.56}$$

Neglecting all other angles except the first two (after substituting average angular velocities in the resonance argument), we get the familiar-looking expression for resonances which relates the angular velocities of two bodies in resonance as a ratio of integers (j_1 and j_2).

$$j_1 n' + j_2 n \approx 0. \tag{3.57}$$

The above expression will correspond to a $|j_1|:|j_2|$ resonance, and the order of the resonance would be $||j_1| - |j_2||$. Using Lagrange's equations for the variation of the orbital elements (considering only the lowest-order terms in e and i) [Murray and Dermott, 1999, pp. 328-329], we have

$$\dot{n} = -\frac{3}{a^2}\frac{\partial D}{\partial \lambda}, \tag{3.58}$$

$$\dot{e} = -\frac{1}{na^2 e}\frac{\partial D}{\partial \varpi}, \tag{3.59}$$

$$\dot{i} = -\frac{1}{na^2 sini}\frac{\partial D}{\partial \Omega}, \tag{3.60}$$

$$\dot{\varpi} = \frac{1}{na^2 e}\frac{\partial D}{\partial e} + \frac{sin(i/2)}{na^2}\frac{\partial D}{\partial i}, \tag{3.61}$$

$$\dot{\Omega} = \frac{1}{na^2 sini}\frac{\partial D}{\partial i}, \tag{3.62}$$

$$\dot{\epsilon} = \frac{e}{2na^2}\frac{\partial D}{\partial e}, \tag{3.63}$$

we can substitute the values of the time derivatives of the angles in terms of the disturbing function. In this way, we convert Eq 3.56 into a second-order differential equation by differentiating again with respect to time.

All our results will be derived for an external resonance case (e.g., Pallene-Enceladus). Murray and Dermott [1999, pp. 334-341] discuss internal resonances. If we assume that the internal perturber's angular values have second derivatives equal to zero (this occurs because the bigger mass's orbit is not disturbed significantly by the smaller mass) and only the perturbed body (interior to the perturbing moon) undergoes changes with respect to time, we get

$$\ddot{\phi} = j_1 \dot{n}' + j_1 \ddot{\epsilon}' + j_3 \ddot{\varpi}'. \tag{3.64}$$

We can calculate $\ddot{\phi}$ in terms of the orbital parameters now.

$$\dot{\epsilon}' = \alpha e'^2 C_s + \frac{1}{2}\alpha |j_3| C_r e'^{|j_3|} e^{|j_4|} sin^{|j_6|}(i/2) sin^{|j_5|}(i'/2) cos\phi, \tag{3.65}$$

$$\ddot{\varpi}' = 2\alpha C_s + \alpha |j_3| C_r e'^{|j_3|-2} e^{|j_4|} sin^{|j_6|}(i/2) sin^{|j_5|}(i'/2) cos\phi, \tag{3.66}$$

and

$$\dot{n}' = 3\alpha j_1 C_r n' e'^{|j_3|} e^{|j_4|} sin^{|j_6|}(i/2) sin^{|j_5|}(i'/2) sin\phi, \tag{3.67}$$

where

$$C_s = \frac{Gm}{n' a'^2 a}\frac{1}{8}\left[2\alpha D + \alpha^2 D^2\right] b^0_{1/2}, \tag{3.68}$$

$$C_r = \frac{mn'}{M_c\alpha} f_d(\alpha). \tag{3.69}$$

Here $f_d(\alpha)$ is a function as defined by Murray and Dermott [1999, pp. 539-556] and will be evaluated for our specific case later in this chapter (Eq. 3.74). Differentiating these first-order differential equations (Eq. 3.65 - 3.67) again, we get

$$\ddot{\epsilon}' = 2\alpha e'\dot{e}'C_s + \frac{1}{2}\alpha|j_3|C_r e'^{|j_3|-1}e^{|j_4|}sin^{|j_6|}(i/2)sin^{|j_5|}(i'/2)\left[|j_3|\dot{e}' - \dot{\phi}e'sin\phi\right], \tag{3.70}$$

$$\ddot{\varpi}' = \alpha|j_3|C_r e'^{|j_3|-3}e^{|j_4|}sin^{|j_6|}(i/2)sin^{|j_5|}(i'/2)\left[(|j_3|-2)\dot{e}'cos\phi - \dot{\phi}e'sin\phi\right], \tag{3.71}$$

and

$$\ddot{n}' = 3\alpha j_1 C_r n' e'^{|j_3|-1}e^{|j_4|}sin^{|j_6|}(i/2)sin^{|j_5|}(i'/2)\left[|j_3|e'sin\phi\dot{\phi} + e'cos\phi\dot{\phi}\right]. \tag{3.72}$$

These equations can be substituted into Eq. 3.64 to get the pendulum model equation for an exterior resonance. Let us now see a specific calculation for the case presented by Methone and Mimas, where we use equations similar to the ones derived above for the internal case [Murray and Dermott, 1999, pp. 334-341].

In the last section we identified prominent resonance arguments that librate for the Methone-Mimas case. We now calculate the exact form of the pendulum equations for the two resonances that are first-order. Let's take the corotation resonance with the argument

$$15\lambda_{Methone} - 14\lambda_{Mimas} - \varpi_{Mimas}. \tag{3.73}$$

For this case, $j_1 = 15$, $j_2 = -14$, $j_3 = 0$, $j_4 = -1$, $j_5 = 0$ and $j_6 = 0$. Also

$$f_d(\alpha) = \frac{1}{2}\left[-30 - \alpha\delta\right] b^{15}_{1/2}(\alpha). \tag{3.74}$$

We calculate $C_r = -2.701 \times 10^{-11}$ and $C_s = -1.286 \times 10^{-10}$. This gives the second-order equation for ϕ as

$$\ddot{\phi} = 3C_r j_1^2 n_{Methone} e_{Mimas} \frac{a_{Mimas}}{a_{Methone}} sin\phi, \tag{3.75}$$

which implies an angular frequency for small librations ($\phi << 1$) of

$$\omega_{corotation} = \sqrt{-3C_r j_1^2 n_{Methone} e_{Mimas} \frac{a_{Mimas}}{a_{Methone}}}. \tag{3.76}$$

Notice that C_r is negative in the above equation. On substituting values, the oscillation period is ∼460 days.

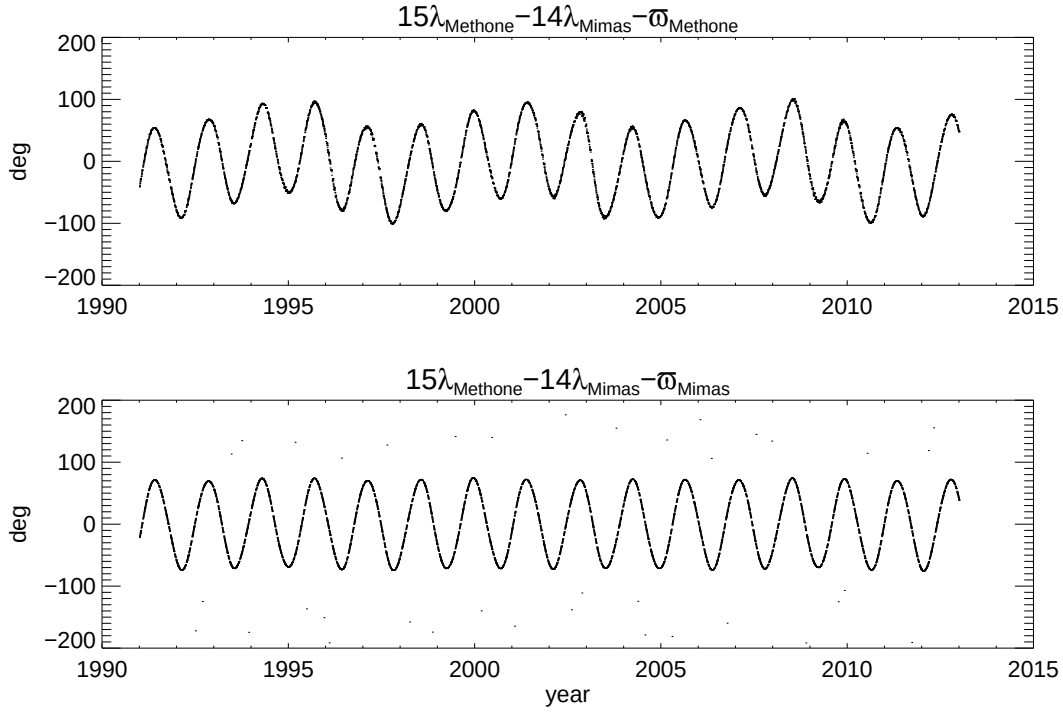

Figure 3.4: (a) The argument of the 15:14 Lindblad resonance for Methone and Mimas. (b) The argument of the 15:14 outer corotation resonance for Methone and Mimas. These plots are drawn from NASA kernels [Acton, 1996].

Figure 3.4(b) displays the same argument, where its period is seen to be about ∼550 days. A difference between idealization and reality is expected because of higher-order terms which were neglected.

Further, the 15:14 Lindblad resonance argument is

$$15\lambda_{Methone} - 14\lambda_{Mimas} - \varpi_{Methone}. \tag{3.77}$$

For this case $j_1 = 15$, j_2 = -14, j_3 = -1, $j_4 = 0$, $j_5 = 0$ and $j_6 = 0$. Also

$$f_d(\alpha) = \frac{1}{2}\left[29 + \alpha D\right] b_{1/2}^{14}, \tag{3.78}$$

where d = 27, where we neglect higher order terms. We calculate that $C_r = 2.69581 \times 10^{-11}$ and $C_s = -1.28624 \times 10^{-10}$, so that the second-order differential equation for ϕ is

$$\ddot{\phi} = 3C_r j_1^2 n_{Methone} e_{Methone} \alpha sin\phi + j_3^2 C_r \alpha \left[-\frac{C_r \alpha |j_3| sin(2\phi)}{2e_{Methone}^2} - \frac{\dot{\phi} sin\phi}{e_{Methone}} \right]. \tag{3.79}$$

This nonlinear equation can be solved numerically to identify its oscillations. We evaluate the values of coefficients and then solve the following equation:

$$\ddot{\phi} = 1.25062 \times 10^{-16} sin\phi - 3.30795 \times 10^{-14} sin(2\phi) - 2.57214 \times 10^{-7} \dot{\phi} sin\phi, \tag{3.80}$$

which has an oscillation period of 460 days, for an oscillation with an amplitude of 70^o. Figure 3.4(a) displays the same argument from the simulations and its period is about 550 days.

Following similar algebra for Anthe's case we can calculate $C_r = -2.113 \times 10^{-11}$ and the libration period to be $\sim$ 720 days (using $j_1 = 11$).

3.5 Libration width

The libration width is the distance that a body can be displaced from the exact resonance and still display a pendulum-like motion. The same argument developed in the previous section can now be used to determine this width. The total specific energy (kinetic and potential per unit mass) of a body during its pendulum motion can be written as [Murray and Dermott, 1999, p. 336]

$$E = \frac{1}{2}\dot{\phi}^2 + 2\omega^2 sin^2 \frac{\phi}{2}. \tag{3.81}$$

The constant E can be calculated as the maximum potential energy that the body will have when at the extrema of its oscillation ($\dot{\phi} = 0$ and $\phi = \pi$). This gives

$$E = -6j_1^2 C_r n' e^{|j_4|} e'^{|j_3|} \alpha = 2\omega^2. \tag{3.82}$$

Substituting these values into Eq. 3.81 gives

$$\dot{\phi} = \pm\sqrt{12 j_1^2 |C_r| n' e^{|j_4|} e'^{|j_3|} \alpha}\; cos\frac{\phi}{2}. \tag{3.83}$$

Differentiating Kepler's law, we get

$$\delta a = -\frac{2}{3}\frac{\delta n}{n} a. \tag{3.84}$$

Now, from Eq. 3.67 with the values substituted, we have

$$\dot{n}' = 3j_1 C_r n' \alpha e^{|j_4|} e'^{|j_3|} sin\phi. \tag{3.85}$$

This and Eq. 3.65 can be used to derive n' as a function of ϕ which in turn can be employed to arrive at

$$\delta n' = \sqrt{12|C_r| n' \alpha e^{|j_4|} e'^{|j_3|}}. \tag{3.86}$$

Hence, using Eq. 3.84, we have

$$\delta a'_{max} = \pm\sqrt{\frac{16}{3}\frac{|C_r| \alpha e^{|j_4|} e'^{|j_3|}}{n'}} a'. \tag{3.87}$$

Substituting values, we find $\delta a'_{max} = 35.67$ km for the Mimas-Methone corotation resonance and $\delta a'_{max} = 2.51$ km for the Lindblad resonance. Clearly the corotation resonance has a larger amplitude and a higher stability range.

Again, following similar algebra for Anthe's case we get the libration width of Anthe-Mimas resonance near Anthe's orbit to be about 34.52 km.

3.6 Resonance-splitting

Finally, let us outline the procedure to determine the radial separation between the locations of these two similar nearby resonances (slightly different resonance arguments but with the same leading terms). This separation can be used to address the stability of particles within a given resonance in the presence of another neighboring resonance argument. We illustrate the process by using the case of the corotation and Lindblad resonances of the Mimas-Methone system. Let particle 1 be in the 15:14 corotation resonance with Mimas; its relation for the exact resonance will be

$$15n_1 - 14n_{Mimas} - \dot{\varpi}_{Mimas} = 0. \tag{3.88}$$

For particle 2 (considered to be in the 15:14 Lindblad resonance with Mimas), a similar expression is given by

$$15n_2 - 14n_{Mimas} - \dot{\varpi}_2 = 0. \tag{3.89}$$

Taking the difference between the two equations, we have

$$n_1 - n_2 = \Delta n = \dot{\varpi}_{Mimas} - \dot{\varpi}_2. \tag{3.90}$$

Using Eq. 3.84, this can instead be expressed as

$$\Delta a = \frac{2}{45}\frac{a_{Mimas}}{n_{Mimas}}\left(\dot{\varpi}_{Mimas} - \dot{\varpi}_2\right). \tag{3.91}$$

For Methone's example, from Eq. 3.91, Δa is 3.29 km, indicating the two resonances are near one another. This potentially complicates the dynamics of the particles in Methone's arc, as they may switch from one resonance to another following a slight perturbation. In Chapter 4 we will use the results developed above to describe the dynamics of particles in the Methone and Anthe arcs and in Pallene's ring.

CHAPTER 4

THE DYNAMICS OF RING ARCS FOR ANTHE, PALLENE AND METHONE

4.1 Introduction

Images from the Cassini mission have revealed three dusty faint rings of Saturn that lie along the orbits of three small Saturnian moons - Methone, Anthe and Pallene [Hedman et al., 2009a]. The three moons have radii of $1-3$ km. Table 4.1 lists the physical and orbital properties of these three moons along with those of Mimas and Enceladus. It is noteworthy that the moons Anthe and Methone have arcs associated with them, while Pallene has a complete ring along its orbit (for dusty particles). All three moons experience resonant or near-resonant perturbations from nearby, bigger moons of Saturn. Mimas (semimajor axis of $3.08R_S$ where R_S is Saturn's radius) lies interior to all the satellites while Enceladus ($3.95R_S$) is exterior. Methone is in both a 15:14 Lindbad resonance [Spitale et al., 2006] and a co-rotation resonance with Mimas [Hedman et al., 2009a]. Anthe is in a 11:10 co-rotation resonance with Mimas [Cooper et al., 2008]. Pallene was reported to be in a 19:16 mixed resonance with Enceladus [Spitale et al., 2006]; however, we show a slightly different near-resonance to be operating.

Burns et al. [1999, 1980] and Dobrovolskis and Burns [1980] have suggested how faint rings may be generated off small moons with impact ejecta supplying ring particles. Starting from a moon's surface, slowly moving particles become trapped into the arcs/rings, as first suggested for the Adams ring of Neptune by Goldreich et al. [1986], who gave a resonance-stabilized theory for the location and extent

of the arcs. Porco [1991] applied this model to Voyager data and identified the 43:42 corotation inclination resonance with Galatea as operative. Horanyi and Porco [1993] further showed that a periodic perturbation changes the effective mean motion, and this in turn displaces the arcs 0.2 km further away from the moon Galatea and also modifies the location of the arc-confining resonances by a comparable amount. Hanninen and Porco [1997] later demonstrated numerically that the combination of the corotation-inclination resonance and an outer Lindblad resonance with Galatea would be able to confine particles for short times in Neptune's ring arcs. However, more recent telescopic observations have found that the arcs' continuing evolution is not consistent with the 43:42 corotation inclination resonance [Sicardy et al., 1999, de Pater et al., 2005]. Consequently, the Porco [1991] model was reformulated by Namouni and Porco [2002] in terms of the 43:42 corotation eccentricity resonance, but required introducing the ring's mass as a free parameter.

Interesting dynamics are found for other confirmed faint rings discovered in the Saturn system by Cassini: the G ring arc [Hedman et al., 2007b] and the Janus-Epimetheus ring [Williams and Murray, 2011]. The Goldreich et al. [1986] model applies more simply to the G ring, which has longitudinally localized material along the orbit of its embedded moon Aegaeon [Hedman et al., 2007b, 2010] that is trapped in a 7:6 co-rotation eccentricity resonance with Mimas. The Janus-Epimetheus ring surrounds the orbits of the moons and is probably supplied by meteoroid impacts into them [Williams and Murray, 2011]. The ultra-faint arcs in this chapter are similar to the G ring, being constrained by the resonances they are involved in. For Pallene though, there is no constrained arc, but the ring maybe maintained inclined due to the resonance, as we will argue in the discussion. Cal-

legari [2013] is also investigating the resonances that operate in this neighborhood.

After recalling some observational evidence for material associated with these three moons, this chapter will describe the dynamical and structural features of the ring associated with Pallene, and of the arcs associated with Methone and Anthe, as observed by the Cassini spacecraft and as illuminated by our numerical simulations and calculations. The next section presents the observations of the arcs and the ring. In Sec. 3 we describe the numerical setup used for the integrations. Section 4 considers the resonances of the moons involved in some detail. We discuss the results in Sec. 5. In Sec. 6 we explore the conditions under which non-gravitational forces are not important, suggesting that gravity explains the observed confinement. Conclusions are presented in the last section.

Moon	Mass (kg)	Radius (km)	density (kg/m^3)	a (R_s)	e	i (deg)	Orbital period (days)
Mimas	$^{j}3.85\times 10^{19}$	$^{r}198$	1184	$^{m}3.0751$	$^{m}0.0202$	$^{m}1.53_F$	$^{m}0.942$
Methone	$^{r'}\sim 10^{13}$	$^{r'}\sim 3$	88	$^{s}3.22$	$^{s}0.0001$	$^{s}0.007$	$^{s}1.01$
Anthe	$^{c}\sim 10^{13}$	$^{c}\sim 2$	298	$^{p}3.28$	$^{p}0.001$	$^{p}0.1$	$^{p}1.037$
Pallene	$^{p'}\sim 5\times 10^{13}$	$^{p'}\sim 2$	1492	$^{s}3.52$	$^{s}0.004$	$^{s}0.181$	$^{s}1.154$
Enceladus	$^{j}1.08\times 10^{20}$	$^{r}252.1$	1611	$^{m}3.9453$	$^{p}0.0045_F$	$^{m}0.02$	$^{m}1.370$

Table 4.1: Physical and orbital properties of selected satellites of Saturn. A suffix 'F' means the number given is the forced value. References: c - Cooper et al. [2008], j - Jacobson et al. [2006], r - Roatsch et al. [2009], r' - Roussos et al. [2006], m - Murray and Dermott [1999] p - Porco et al. [2006], p' - Porco [2007], s - Spitale et al. [2006]

4.2 Observations

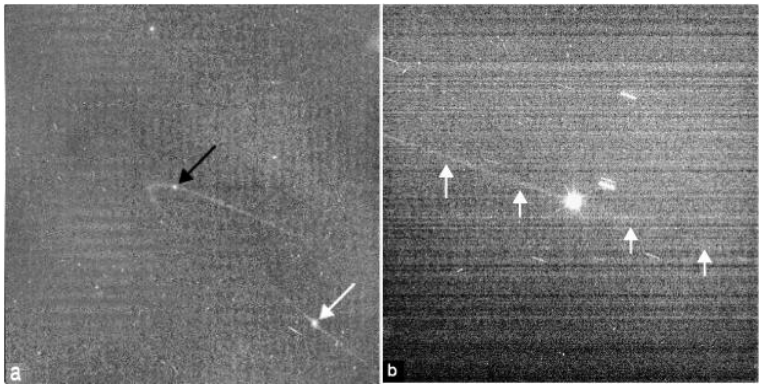

Figure 4.1: (a) One of the images (N1572353098, phase angle 22.6^o), that first revealed the Anthe arc and the Methone arc. Anthe is marked with a black arrow and Methone with a white arrow. The faint streaks surrounding these moons are the Anthe and Methone arcs [Hedman et al., 2009a]. The range to Anthe is 2303167 km (a pixel is $\sim$ 13 km). (b) Nearly edge-on views of the Pallene ring: N1514138009 (range to Pallene=166015 km; a pixel is $\sim$ 10 km), phase angle of 87^o, ring opening angle of 0.26^o. The Pallene ring is marked with white arrows. The bright spot near the image center is Pallene. Orbital motion is from left to right [Hedman et al., 2009a]. Images are produced after standard calibration and flat-fielding and additional removal of a quadratic background. The image is rotated so that Saturn's north pole would point approximately up; the image brightness has been stretched to bring out the subtle details. The horizontal banding is an imaging artifact. The other bright dots are caused by stars and cosmic rays.

Figure 4.1a shows the arcs associated with Methone and Anthe [Hedman et al., 2009a]; each extends only a finite range of longitudes surrounding the respective moons. The observed longitudinal extents of the arcs are $\sim 20^o$ for Anthe's arc and $\sim 10^o$ for Methone's arc; these are less than the theoretically maximum possible values (the length of each resonance well). Anthe is found to be librating within its arc of material [Hedman et al., 2009a]. Figure 8 in Hedman et al. [2009a] shows the radial width of Anthe's arc to be a few hundred km. Methone's arc has similar radial width (personal communication, M. M. Hedman, 2010).

In contrast, Pallene's ring appears continuous, in high-phase-angle images (im-

plying small particles), while images at other phase angles (bigger particles) show a denser arc near Pallene [Hedman et al., 2009a]. At high phase the Pallene ring has a radial full-width at half-maximum of approximately 2500 km [Hedman et al., 2009a]. But medium-phase images (personal communication, M. M. Hedman, 2012) find a radial width of $\sim$ 100 km. They also indicate that the ring is extremely thin vertically, having an approximately Gaussian vertical profile with a full-width at half-maximum of less than 50 km (much less than the $\sim$1300 km vertical excursions of the moon from Saturn's equatorial plane due to its inclination). This implies that Pallene's ring is inclined like the moon's orbit, by about 0.2^o. This is surprising because we might expect the ring to become axially symmetric due to the precession caused by Saturn's oblateness (see Fig. 4.1b, Hedman et al. [2009a]). In our calculations, we will assume a radial width of $\sim$ 200 km for the ring and arcs. We investigate Pallene's arc particles resonance with Enceladus (confinement and inclination).

As discussed in Ch.1 (Fig. 1.10), the in-situ absorption signatures associated with Methone's arc [Roussos et al., 2008] indicate a 15^o-long longitudnal arc with particles larger than a mm and with optical depth lower than $\sim 10^{-6}$. Higher-phase images of Pallene [Hedman et al., 2009a] display a thin ring of smaller particles around Saturn.

These observations give us some typical parameter values to work with in our simulations of these arcs and ring. Pallene ring is clearly continuous for dusty particles (from high-phase angle images), but it is not clear whether this is true for larger particles (from mid and low-phase images).

4.3 Numerical setup

Motivated by these observations, numerical simulations were carried out to understand the dynamics of the arcs and ring associated with these small moons. For initial conditions of the ring particles, we started them from the surfaces of their respective moons. The initial speeds from the moon's surface are chosen to be of the order of its escape speed. The numerical integration package SWIFT [Levison and Duncan, 1994a] was the prime mode of carrying out simulations where close encounters and collisions were enabled. Our simulations are carried out with Saturn considered as an inertial frame; this is valid because Enceladus' mass is 10^{-7} of Saturn's and because Saturn's gravitational acceleration due to the Sun is many orders of magnitude less than the accelerations of the particles that we study.

Impacts of interplanetary meteoroids onto a moon's surface will eject material [Burns et al., 2001]. Many particles will fall back on the moon as they are unable to overcome the moon's gravitational pull. Particles with higher velocities (of the order of escape speed of the moon), though lesser in number, can escape the moon's gravitational influence and supply the ring or arcs along the orbit of the moon. Because they present a reasonably large cross-section to be hit by micrometeoroids and have little gravity to keep the impact ejecta from escaping, satellites of 1-100 km in radius are thought to be ideal sources for supplying escaped ejecta [Burns et al., 1999]. Since Anthe, Methone and Pallene are at the smaller end of this distribution, they will test this ejection model. The velocity distribution of this impact ejecta depends on the surface properties of the moon being hit and its radial distance from Saturn [Burns et al., 1980]. Assuming this model to supply particles, grains were started from the surface of the moons.

In most of our simulations, particles with a range of speeds uniformly varying between $1.0v_{esc}$ to $1.1v_{esc}$ (v_{esc} is the escape speed from the surface of an isolated, non-rotating spherical moon, which is 0.94 m/s for Methone, 1.15 m/s for Anthe and 1.83 m/s for Pallene) were launched normal to the surface of the moons from regularly spaced grids on the surface. Instead of directly integrating the orbits of the moons, the NAIF kernels for these orbits [Acton, 1996] with previously integrated orbits were used to improve accuracy and to better mimic the real situation. The NAIF kernels (Table 4.2) contained orbit information for the interval 1/1/91 to 12/31/13, thus limiting our particle integrations to be 23 yrs. Within our integrations, the unit of length is one Saturnian radius ($R_S = 60,330$ km), the unit of time is 24 hrs and G = 1 (see Ch. 2). We, however, present results in 'mks' units. Simulations were carried out in the Saturnian inertial frame of reference, non-rotating with Saturn at the origin. Saturn's mass is 5.6851×10^{26} kg. The planet's gravity field includes the higher-order gravitational moments $J_2 = 0.016298$ and $J_4 = -0.000915$ for R_S = 60,330 km [Murray and Dermott, 1999]. Table 4.3 presents the properties of all other moons included in out short-term (23 years) simulations.

Kernel	Description
sat252s.bsp	Mimas, Enceladus, Tethys, Dione, Rhea, Titan, Methone
sat281.bsp	Pallene, Anthe
de418	Saturn Barycenter
naif0008.tls	Kerner wrapper
saturn_inertial.tk	Saturn-o-centric inertial coordinate system

Table 4.2: Kernels used for the moons.

Massless test particles with velocities near or in excess of the escape speeds at the surfaces of the moons may escape their gravitational pulls [Dobrovolskis and Burns, 1980]. These particles will subsequently respond to the gravitational

Name (NAIF id)	Mass (kg)	Radius (km)	Semimajor axis (Rs)
Mimas (601)	3.85×10^{19}	198	3.0751
Enceladus (602)	1.08×10^{20}	252.1	3.9453
Tethys (603)	6.18×10^{20}	530	4.8835
Dione (604)	1.10×10^{21}	560	6.2555
Rhea (605)	2.31×10^{21}	764	3.7371
Titan (606)	1.35×10^{23}	2575	20.2531

Table 4.3: Properties of moons included in simulation [Murray and Dermott, 1999].

influence of Saturn and the other six moons - Mimas, Enceladus, Tethys, Dione, Rhea, Titan. If a particle collides with a moon, it is removed from the simulation. We assume that the particles in Anthe's and Methone's arcs and Pallene's ring do not affect each other. Non-gravitational forces are not included in our simulations, but we anticipate them to play an important role over longer periods of time (see Sec. 4.6).

4.4 Resonances inhabited by moons

Each of these three moons appears to be in some resonant relationship with either Mimas or Enceladus [Spitale et al., 2006, Cooper et al., 2008, Hedman et al., 2009a]. This can be seen by plotting the resonance arguments, which are linear combinations of the orbital elements of the moons as derived from the kernels. We also wish to explore other possible similar resonances. The orbital elements used here are epicyclic or geometric elements [Renner and Sicardy, 2006] rather than conventional osculating elements. Epicyclic or geometric elements use the concept of ring streamlines, which are the flow paths of ring's particles considered as a fluid. These differ from the conventional osculating elements, which are the orbital elements a particle would have if any small perturbation (such as oblateness) were instantaneously removed. When the central body is oblate, the osculating elements

of close-in orbits show significant short-period variations. The epicyclic elements, by contrast, change only slowly on orbital time-scales, and thus are more suitable to use when considering the orbits (with small eccentricities and inclinations) of satellites or ring particles around an oblate planet.

Using the computed orbital elements of the moons, we identified the most prominent resonance arguments. This search was done with the anticipation that the particles starting from the moon's surface with low relative speeds are likely to be trapped in similar and nearby resonances. We plot the moon's prominent resonance arguments for reference. For Pallene we determine that no resonance is present, but rather only a slightly different near-resonance, contrary to a previous report [Spitale et al., 2006]. In the following discussion, the strength of the resonance is measured by the absolute value of the terms multiplied in front of the corresponding resonant terms in the disturbing function (see Ch. 3).

4.4.1 Anthe

Figure 4.2 shows the epicyclic elements of Anthe as functions of time. The mean longitude (λ), argument of pericenter (ω) and longitude of pericenter (ϖ) represent the residual values after linear background trends have been subtracted from each of them. Constant values have also been subtracted from the longitudes in order to give variations with means of zero (see Fig. 4.2). The de-trended mean longitude for Anthe oscillates about its average value, suggesting the effects of a possible mean-motion resonance.

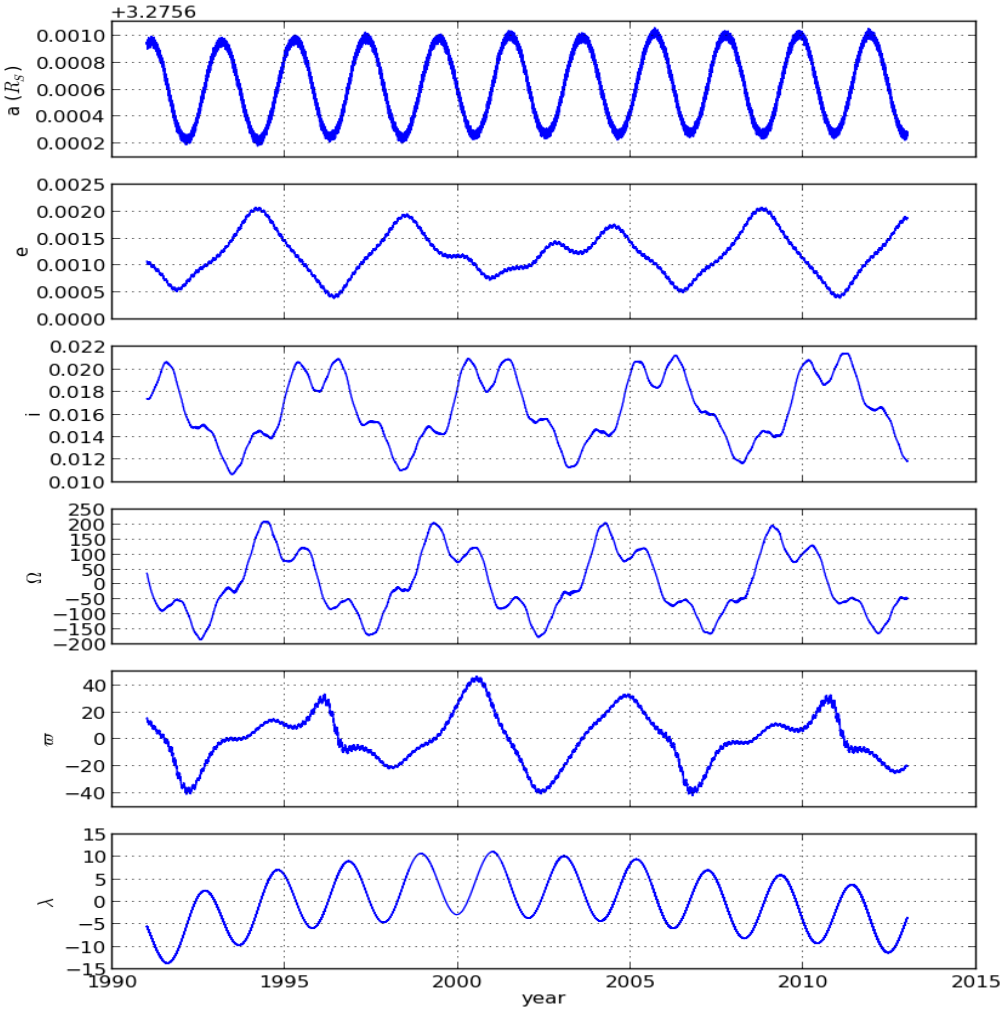

Figure 4.2: The epicyclic orbital elements of Anthe between 1991 and 2013. Here a is the semi-major axis, e is the eccentricity, i is the inclination from Saturn's equatorial plane, Ω is the longitude of ascending node, ϖ is the longitude of pericenter and λ is the mean longitude of Anthe. Best-fit linear background trends have been subtracted from all longitude profiles to identify oscillations around secular trends for Ω, ϖ and λ.

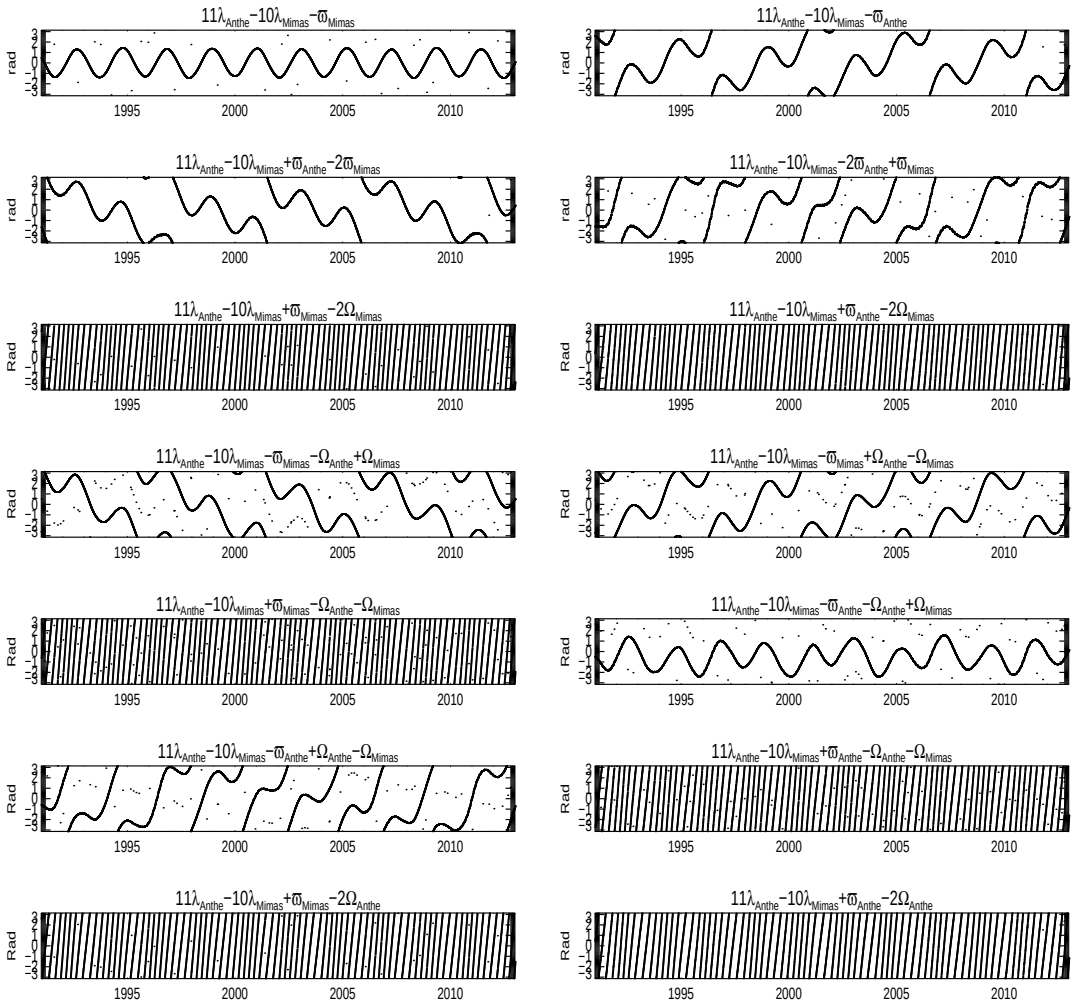

Figure 4.3: Search for possible resonance arguments of similar strengths with the leading variable as $11\lambda_{Anthe} - 10\lambda_{Mimas}$. The figure shows the possible resonance arguments plotted versus time. The vertical axis goes from $-\pi$ to π.

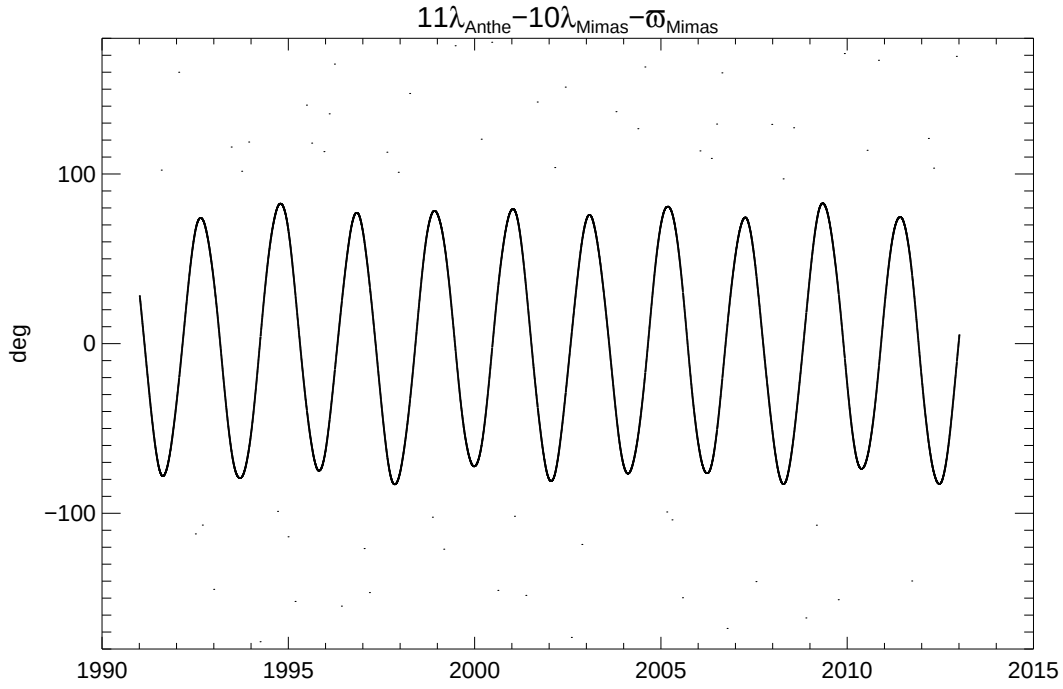

Figure 4.4: The resonance argument, $11\lambda_{Anthe} - 10\lambda_{Mimas} - \varpi_{Mimas}$, for the 11:10 corotation eccentricity resonance of Anthe with Mimas. It is clearly librating.

We search for possible resonance arguments of similar strengths with the leading variable as $11\lambda_{Anthe} - 10\lambda_{Mimas}$, where λ_i is the mean longitude of the i^{th} moon. Figure 4.3 shows possible resonance arguments plotted versus time. Two arguments are constrained (one first-order and one third-order, see Ch. 3). Also, notice that a few other arguments circulate fairly slowly while yet others circulate rapidly. These slow circulations correspond to resonances that the particles in the arcs could inhabit, depending on the energy of those particles. We will analyze this further in the next subsection.

In agreement with Cooper et al. [2008], we verify that Anthe is in the 11:10 corotation eccentricity resonance with Mimas. The resonance argument with maximum

strength is

$$\phi = 11\lambda_{Anthe} - 10\lambda_{Mimas} - \varpi_{Mimas}; \tag{4.1}$$

its history is plotted in Fig. 4.4. When the system was simulated with Mimas removed, the oscillations in the semimajor axis disappeared and the above resonance argument started to circulate. This clearly demonstrates that Anthe is indeed in resonance with Mimas. The amplitude of the oscillation of the resonance argument is 78^o with a period of 2.08 years.

4.4.2 Methone

Figure 4.5 plots the epicyclic elements of Methone as a function of time. The plotted mean longitude, longitude of pericenter and longitude of ascending node again represent the residual values after linear background trends have been subtracted from each of them. Once more we have subtracted constant values from the longitudes in order to give approximately zero mean variability. Even though the orbital elements again show the characteristic oscillations of resonance, the situation in this case is less clear. Plots of all the resonance arguments of similar strengths starting with $15\lambda_{Methone} - 14\lambda_{Mimas}$ are given in Fig. 4.6. Two first-order and two third-order resonance (refer Ch. 3) arguments are librating. A few others drift slowly while the remainder circulate furiously. In the next subsection, we investigate in which resonance Methone's arc particles reside.

Methone is found to be in two prominent first-order resonances with Mimas: the 15:14 corotation resonance with Mimas as well as the 15:14 outer Lindbad resonance with Mimas. Figure 4.7 shows these resonance arguments of Methone with

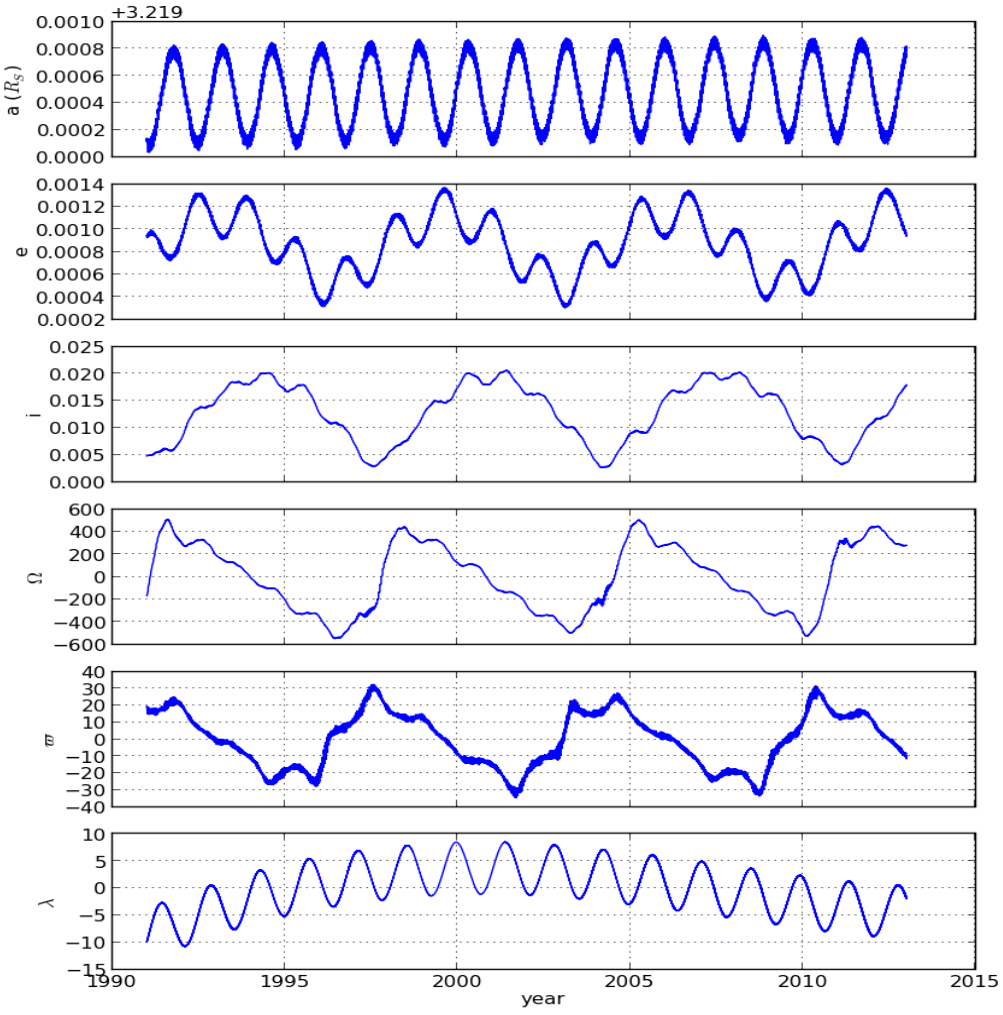

Figure 4.5: The epicyclic orbital elements of Methone between 1991 and 2013. Here a is Methone's semi-major axis, e is the eccentricity, i is the inclination from Saturn's equatorial plane, Ω is its longitude of ascending node, ϖ is its longitude of pericenter and λ is its mean longitude. Best-fit linear background trends have been subtracted from all longitude profiles for Ω, ϖ and λ.

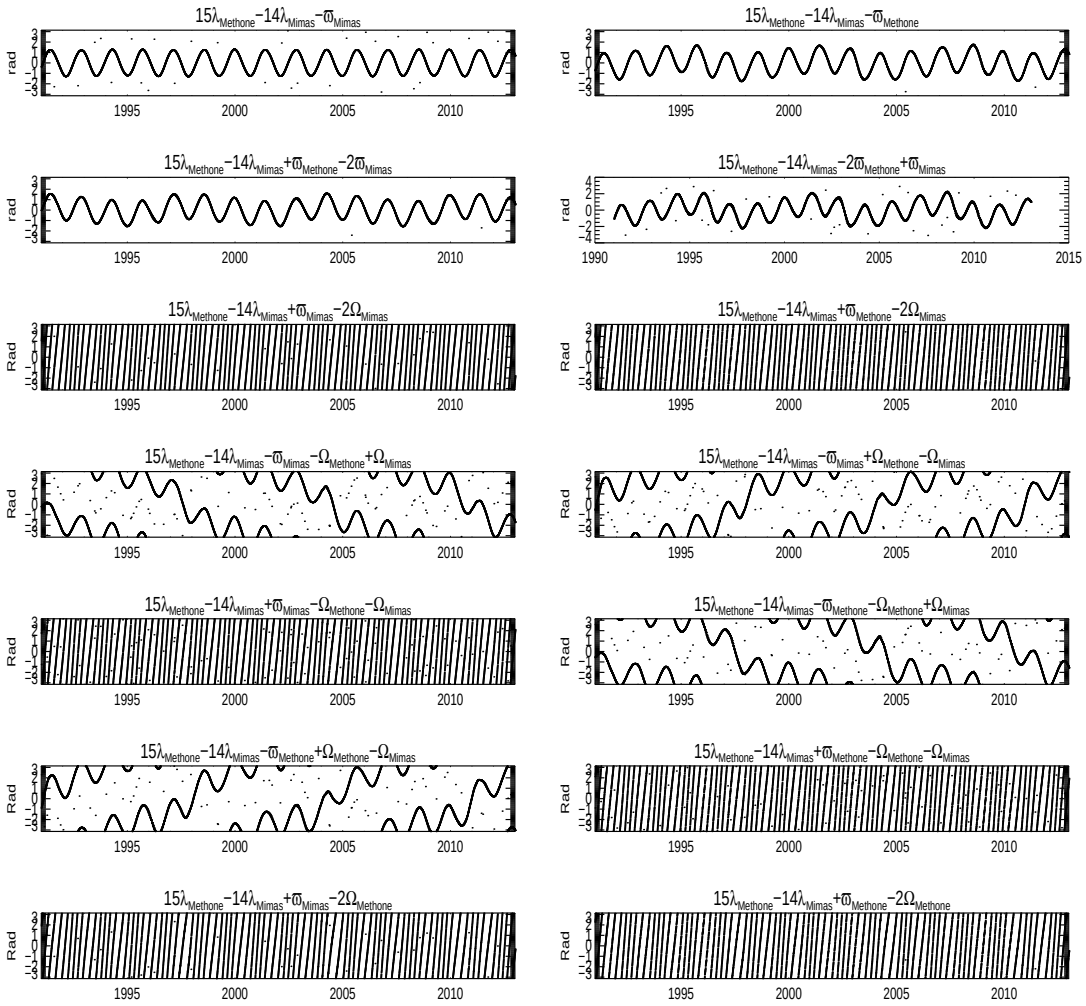

Figure 4.6: Search for possible resonance arguments of similar strengths with the leading variable as $15\lambda_{Methone} - 14\lambda_{Mimas}$. The figure shows the possible resonance arguments plotted versus time. The vertical axis goes from $-\pi$ to π.

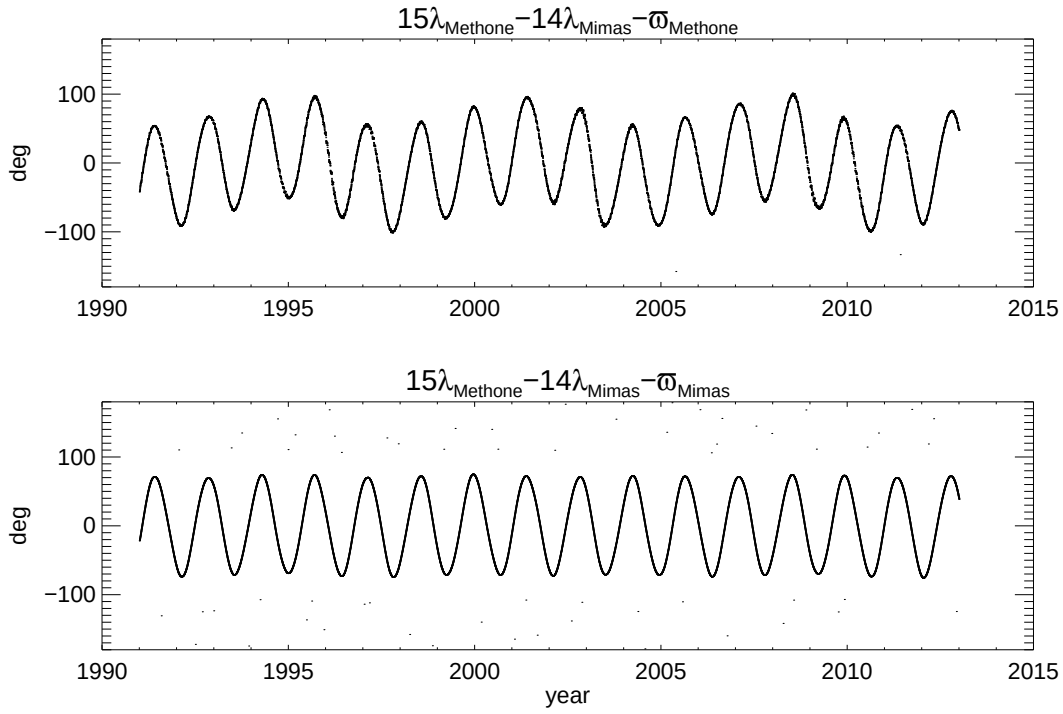

Figure 4.7: Two similar resonance arguments of Methone with Mimas. Top: $15\lambda_{Methone} - 14\lambda_{Mimas} - \varpi_{Methone}$, the 15:14 outer Lindbad resonance with Mimas. Bottom: $15\lambda_{Methone} - 14\lambda_{Mimas} - \varpi_{Mimas}$, the 15:14 corotation resonance with Mimas. Both are seen to librate.

Mimas. Figure 4.7 top plots the corotation resonance argument [Spitale et al., 2006] which is:

$$\phi^T = 15\lambda_{Methone} - 14\lambda_{Mimas} - \varpi_{Methone}, \tag{4.2}$$

and Fig. 4.7 bottom displays the outer Lindbad resonance argument [Hedman et al., 2009a] which is:

$$\phi^B = 15\lambda_{Methone} - 14\lambda_{Mimas} - \varpi_{Mimas}. \tag{4.3}$$

The associated resonant semimajor axes are separated by ~ 3.29 km (as calculated in the last section of Ch. 3). We expect the particles in Methone's arc to have these signatures of the resonances, and this turns out to be true as described in Section 5. The amplitude of each of the oscillations of the two resonance arguments is $\sim 70^o$ and their periods are about 1.3 years. They are similar because the values are primarily determined by the leading terms, which are the same for both.

4.4.3 Pallene

Figure 4.8 shows the histories of Pallene's epicyclic elements. The mean longitude (λ), longitude of pericenter (ϖ) and longitude of ascending node (Ω) represent the residual values after linear background trends have been subtracted from each of them. Constant values have also been subtracted from the longitudes in order to give zero means to the variation. The orbital elements are clearly constrained, particularly Pallene's inclination and its Ω. We will investigate these confinements for the ring particles in the next subsection. Spitale et al. [2006] argue for a possible 19:16 inner, mixed resonance with Enceladus ($19\lambda_{Enceladus} - 16\lambda_{Pallene} - \varpi_{Pallene} - 2\Omega_{Pallene}$). We found this specific argument to be circulating and hence conducted our own search. These differences could be because of different sources

of orbit integrations. Figure 4.9 shows all possible resonance arguments of similar strengths starting with the terms $19\lambda_{Enceladus} - 16\lambda_{Pallene}$. The closest we get is a third-order near-resonance that circulates with a period of ∼20 yrs, and is weakly bound. The coefficients of the disturbing functions corresponding to these near-resonances have triple factors of the eccentricities and inclinations of Enceladus and Pallene, and hence correspond to weak resonances.

Figure 4.10 shows the near-resonance argument that circulates most slowly, given by:

$$\phi = 19\lambda_{Enceladus} - 16\lambda_{Pallene} - \varpi_{Enceladus} - 2\Omega_{Enceladus}. \tag{4.4}$$

The evolution of the near-resonance argument contains a 60^o oscillation with a period of about 1.5 years superposed on a shallow linear trend of ∼20 ^{o}/yr. Thus, this argument is circulating and hence is only a near-resonance, but all other nearby arguments are circulating at much faster rates.

4.5 Particles in the arcs/ring

4.5.1 Extent of arcs/ring

As we have just shown, the dynamics of Anthe and Methone are governed by first-order resonant interactions with Mimas while Pallene has a weak third-order near-resonance with Enceladus. Particles in the arcs, that leave the moons' surfaces at low relative speed, will likely be in the same, or nearby, resonances as their parent moons. As a limiting case, we do not consider non-gravitational accelerations on the particles in our simulations, meaning that our particles are larger

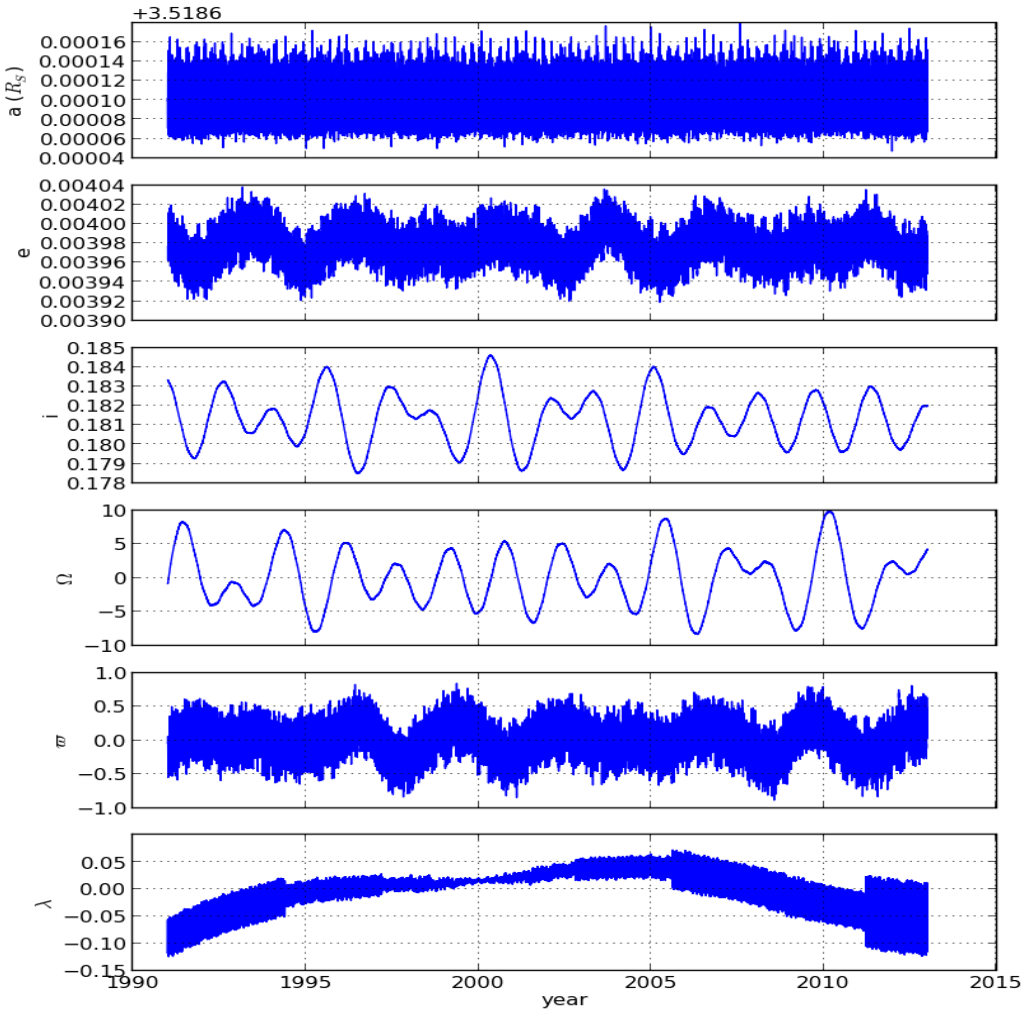

Figure 4.8: The epicyclic orbital elements of Pallene between 1991 and 2013 derived from the kernels (refer to Table 4.2). Here, a is the semi-major axis, e is the eccentricity, and i is the inclination from Saturn's equatorial plane. Best-fit linear background trends have been subtracted from for the mean longitude (λ), longitude of pericenter (ϖ) and longitude of ascending node (Ω). The fuzzyness in several of these curves is due to low-amplitude orbit-frequency changes in the epicyclic elements.

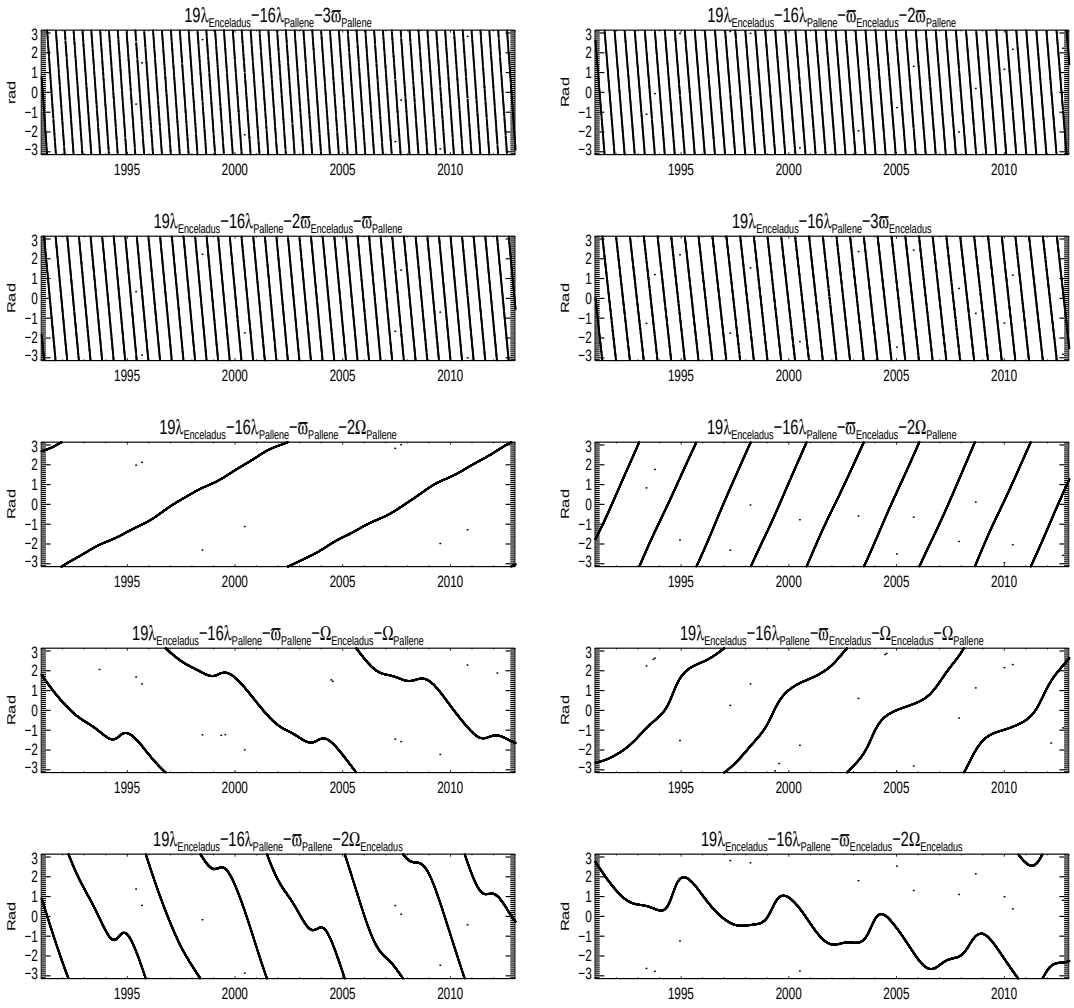

Figure 4.9: Searches for possible resonant arguments of similar strengths with the leading variable as $19\lambda_{Enceladus} - 16\lambda_{Pallene}$. Ten possible resonance arguments are plotted versus time.

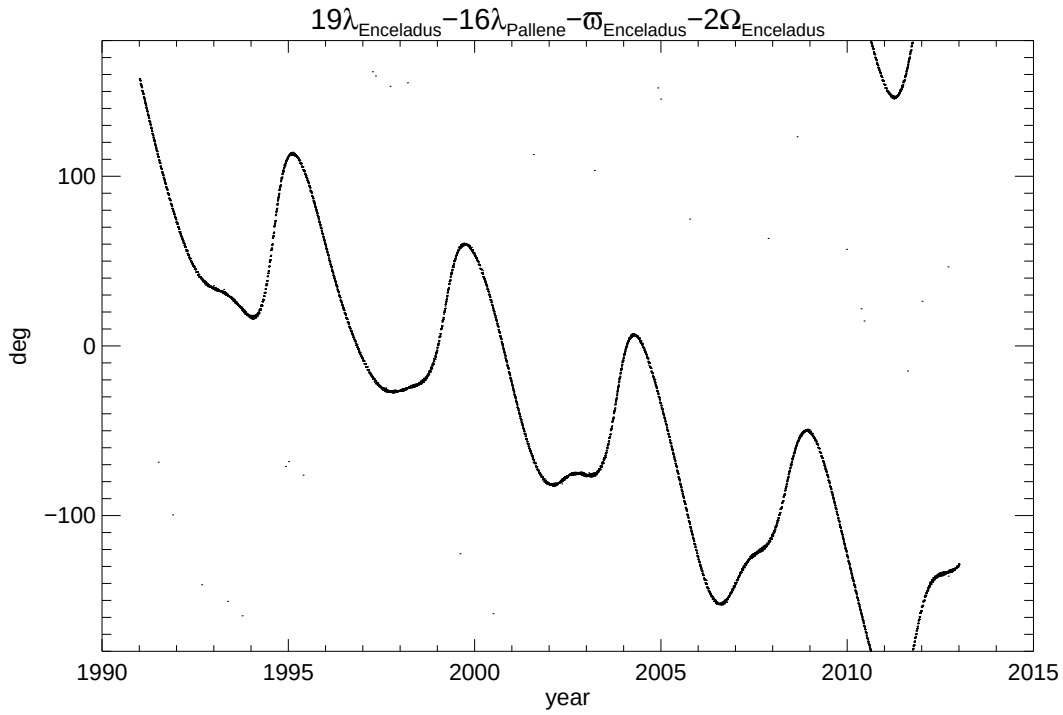

Figure 4.10: The 'near' resonance argument of the 19:16 mixed resonance of Pallene with Enceladus ($19\lambda_{Enceladus} - 16\lambda_{Pallene} - \varpi_{Enceladus} - 2\Omega_{Enceladus}$).

than several microns in size (e.g., Methone's arc has at least some particles larger than 1 mm [Roussos et al., 2008]). In Sec. 4.6 we discuss the situations under which non-gravitational forces (electromagnetic, radiation forces) can be neglected for the simulations considered in this work.

Other nearby moons (Tethys, Dione, Rhea and Titan) have insignificant effects as we have verified by running the simulation with and without those moons, with no change in the stability of the arcs/ring.

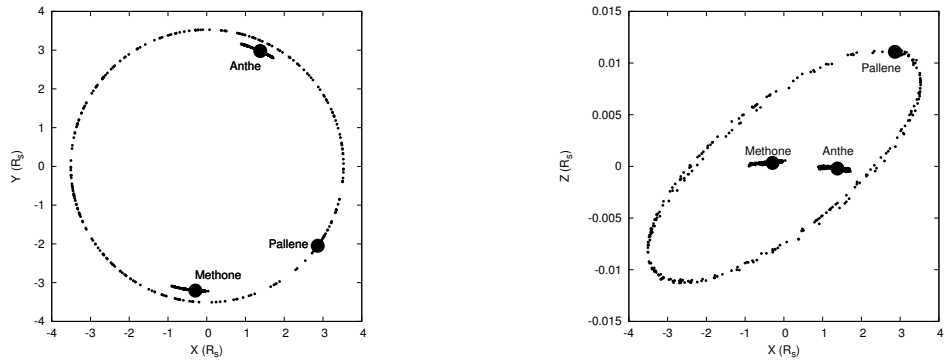

Figure 4.11: Snapshot of the Saturnian ring-arc system on Dec 31, 2013 following twenty three years of perturbations from nine Saturnian moons (Methone, Anthe, Pallene, Mimas, Enceladus, Tethys, Dione, Rhea and Titan). On Jan 1, 1991, 972 particles (324 each) were projected normally with launch speeds 1-1.1 times the formal escape speed from isolated spherical moons (Anthe, Methone and Pallene), uniformly distributed over the surface. The orbital distances along the three axes are given in R_S. The figure clearly shows arcs associated with Anthe and Methone while Pallene sports a ring formed along its orbit around Saturn. The inclination of the ring associated with Pallene is magnified for clarity by stretching the Z axis (250 times). Two arcs of particles lie along the orbits of their respective moons - Anthe and Methone.

Fig. 4.11 shows a snapshot of the system simulated for 23 years. In each of these simulations, 324 particles were started from the surfaces of the three moons; these

particles were launched uniformly from the surface (with a co-latitude grid spaced 10^o, and a co-longitude grid spaced 20^o apart), with velocities from v_{esc} to $1.1v_{esc}$ (uniformly randomly distributed). The plot clearly illustrates that the Anthe and Methone arcs are constrained for this period around the moons while the material from Pallene forms a complete ring of material encircling Saturn. We recall that the resonances of Methone and Anthe are first-order while Pallene's near-resonance is only third-order and hence much weaker. We compare the strength of resonance in the next subsection. Since the arcs and ring particles are in similar resonances as their parent moons (as we show next), it presumably explains why the former arcs are constrained while Pallene's ring is not. The third-order near-resonance has a smaller potential well, making the confinement of particles less likely. We proceed with detailed simulations and calculations of particles associated with Anthe and Methone followed by Pallene's case.

Figure 4.12 displays temporal snapshots of particles continuously emitted from Anthe's surface (with a period of 1/20 th of a day), from all over the surface. The figure indicates clearly that the arc is constrained near Anthe as the maximum azimuthal extent beyond Anthe is $\sim 10^o$ on either side, in the 23 years of evolution studied here. Similar analysis for Methone's arc follows in Fig. 4.13. Different concentrations of particles in the first subplot result from particles being at different phases as a result of close encounter with the moon. With time, the particles drift around the resonant region, but remain constrained by Mimas' resonance. This can be considered as the early parts of the evolution of the arcs, but conclusively shows that they are indeed constrained after 23 yrs. For example, Fig. 4.14 (top) shows the vertical excursion of a particle started from Methone versus the

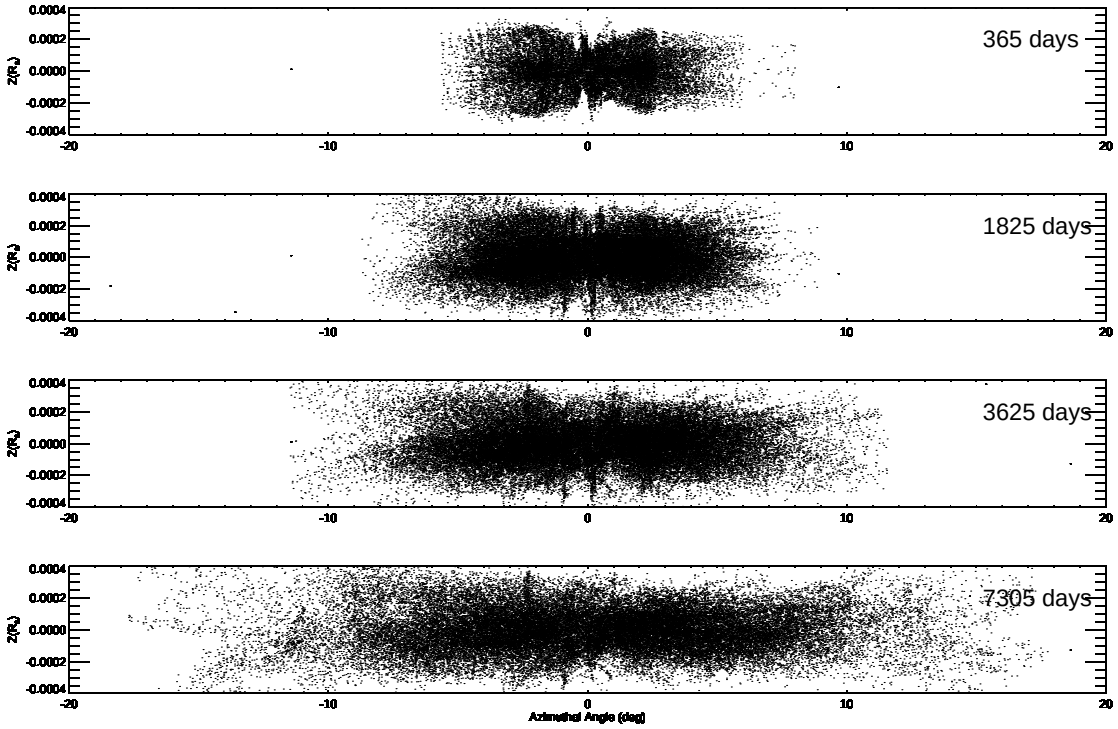

Figure 4.12: The temporal snapshots of Anthe's arc: The vertical height vs azimuth for particles near Anthe started at (0,0) and followed to subsequent times with the path sampled once per day. The arc is seen to be constrained within $\sim 10^o$, in 20 yrs. The non-uniformity of particles in the initial phases can be attributed to stroboscopic effects as detailed in the text.

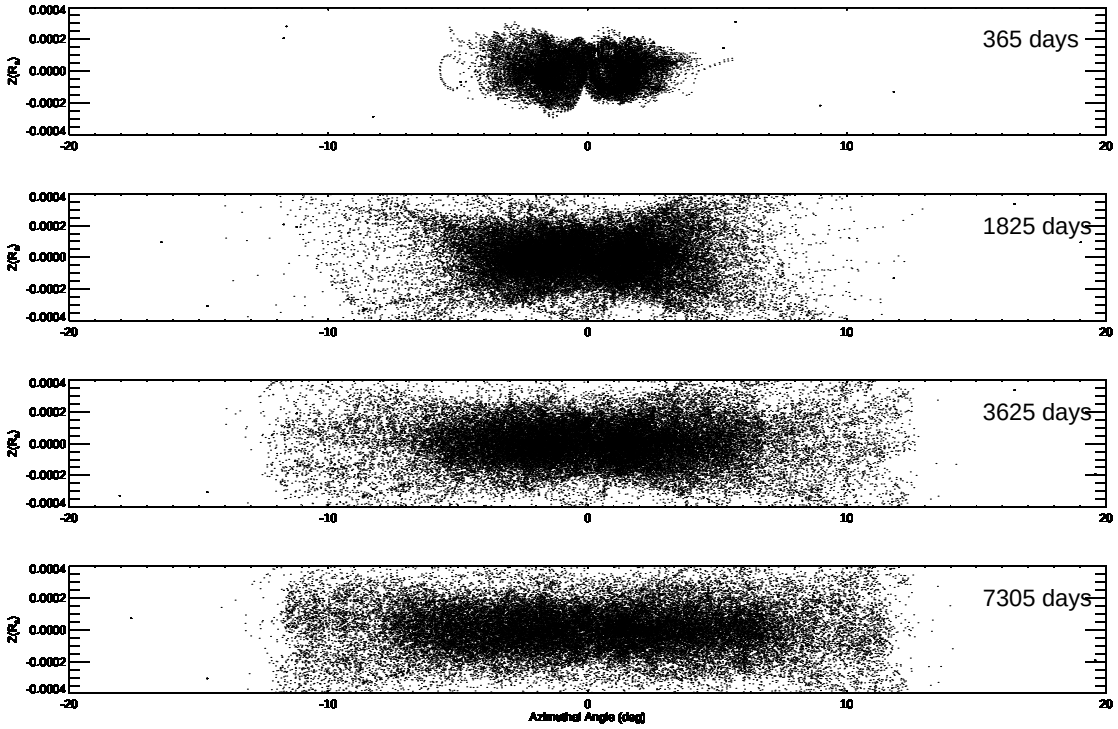

Figure 4.13: The temporal snapshots of Methone's arc: The vertical height vs azimuth of particles near Methone started at (0,0) and followed to subsequent times with path sampled once per day. The arc is seen to be constrained within $\sim 10^o$, in 20 yrs. The non-uniformity of particles in initial phases can be attributed to stroboscopic effects as detailed in the text.

azimuthal angle along Methone's orbit with 20 data points plotted per day. This orbit is drawn in the frame fixed at Methone at (0,0). The particle starts from (0,0), moves to the right and then starts to move back to the left, all throughout oscillating in the vertical direction. The same plot with 1 data point per day is shown in Fig. 4.14 (middle). This also illustrates the libration but not all the details of the vertical oscillations. A collection of particles launched from different latitudes from Methone with 1 data point per day plotted is further shown in Fig. 4.14 (bottom). In the top plot of Fig. 4.13, the patch missing below the moon can be explained because of this stroboscopic effect.

By contrast, Pallene's particles are not similarly confined, but fill the entire orbit (Fig. 4.15). The sinusoidal distribution in (z, θ) of Pallene's particles indicates the ring's inclination. We will calculate the spreading rate associated with Pallene's ring shortly and speculate on the age of Pallene's ring.

We now investigate the resonance arguments of particles in the arcs surrounding Anthe and Methone. As expected, the particles are found to reside in the same resonances as their respective parent moons. Figures 4.16 and 4.17 show the fraction of particles versus the amplitudes of their resonance arguments. In Anthe's case, the spread of amplitudes produces a distribution of particles with two peaks around the moon's libration amplitude, one on each side, which forms an arc along its orbit. The case of Methone-associated particles is more complicated just like Methone's, where the moon exhibits two resonances. Particles around Methone are in a Lindblad resonance, and Fig. 4.17 (left) indicates that the resonance arguments are librating, with the distribution peaked around that of Methone's,

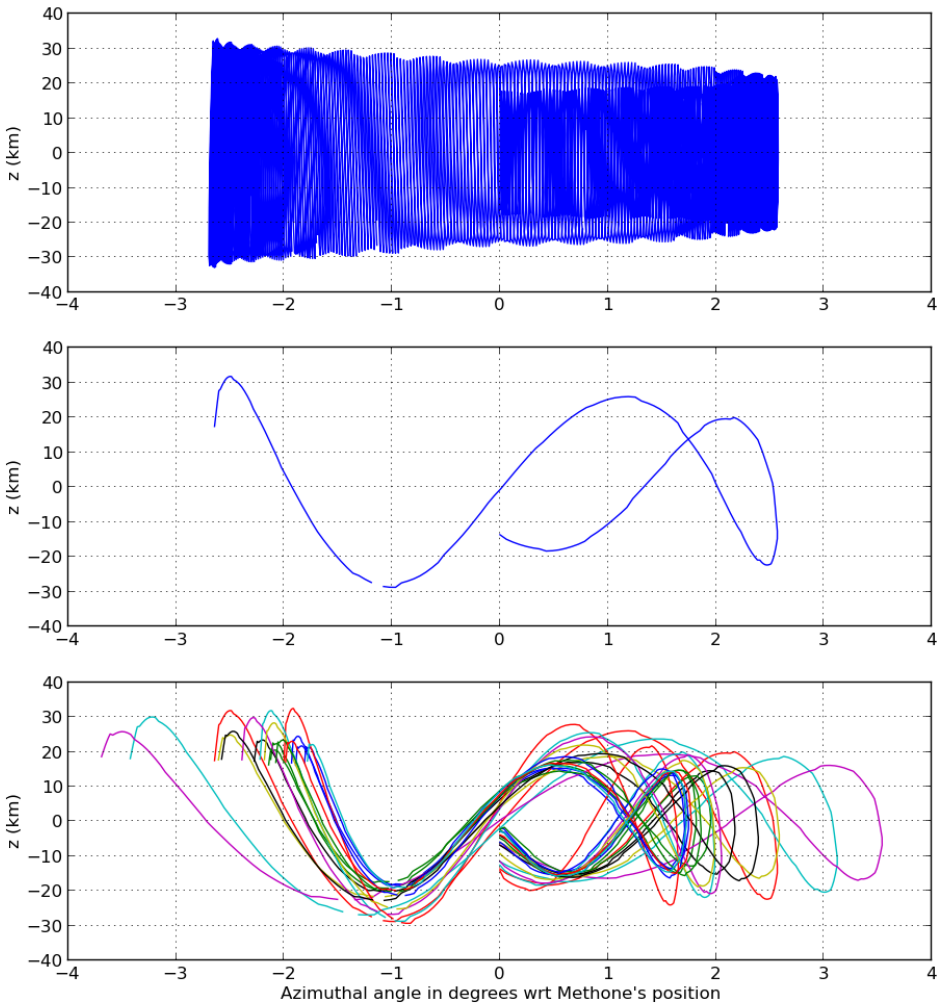

Figure 4.14: Top: Vertical excursion of a particle started from Methone versus the azimuthal angle (with respect to Methone) with 20 data points per day. Middle: vertical excursion of a particle started from Methone versus the azimuthal angle with 1 data point per day. Bottom: Vertical excursion of a 18 particles started from Methone, with varying launch positions, versus the azimuthal angle with 1 data point per day. The pattern below (0,0) happens when the particles cross the equatorial plane almost at the same time, because of similar orbital periods, initially in the evolution. All these orbits are plotted for 190 days of evolution after launch.

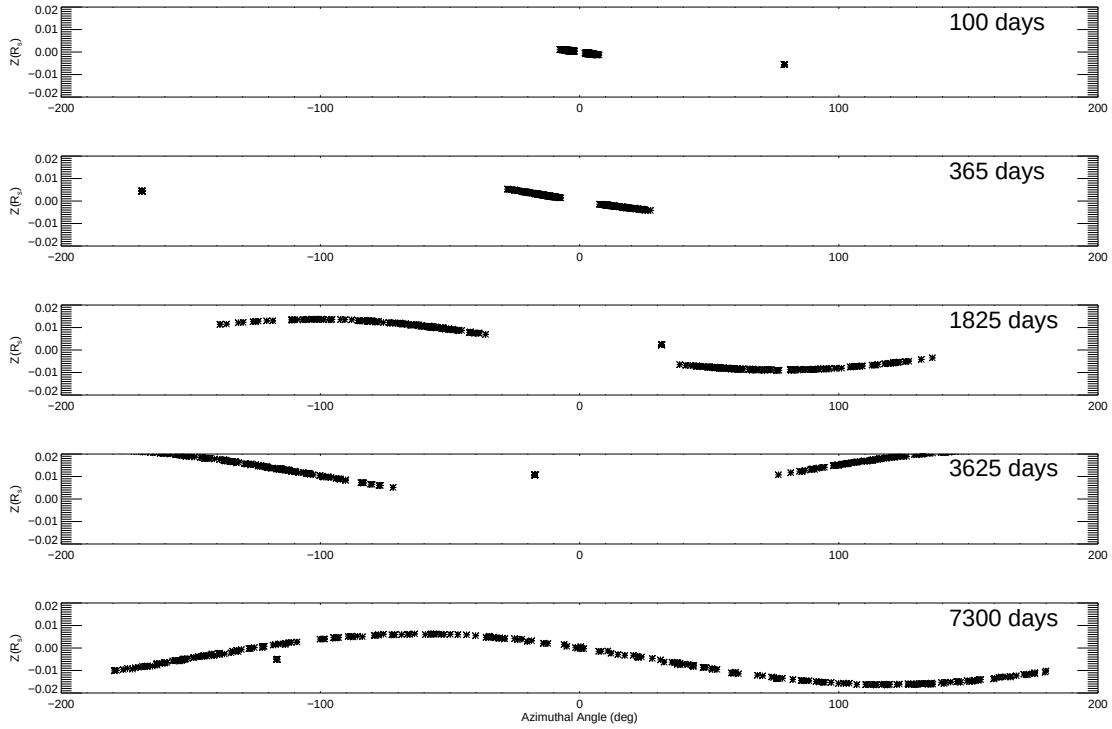

Figure 4.15: The vertical height vs azimuth of 324 particles near Pallene, which is located at (0,0), at subsequent times following launch from the surface. The sinusoidal shape reflects ring's inclination.

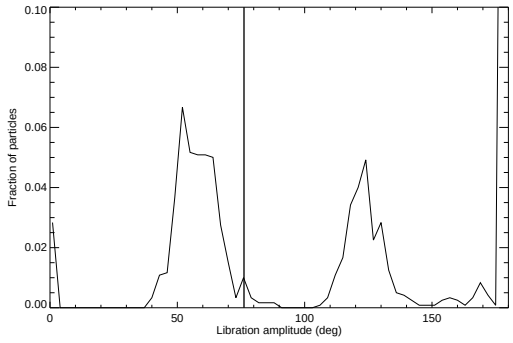

Figure 4.16: Distribution of the libration amplitudes of the resonance argument ($\phi = 11\lambda_{Par} - 10\lambda_{Mimas} - \varpi_{Mimas}$) of particles (subscript-Par) around Anthe after 23 years of integration. The vertical line locates Anthe's libration amplitude. About 50 percent of the $\sim$2600 particles launched get trapped in resonance. The rest collide with the moon.

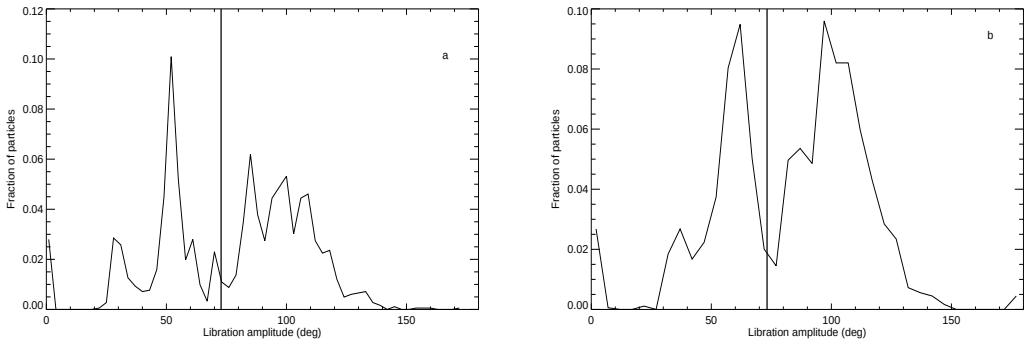

Figure 4.17: Distribution of the libration amplitudes of the resonance arguments (left: $\phi = 15\lambda_{Par} - 14\lambda_{Mimas} - \varpi_{Par}$, right: $\phi = 15\lambda_{par} - 14\lambda_{Mimas} - \varpi_{Mimas}$) of particles (subscript-Par) near Methone after 23 years of integration. The vertical line locates Methone's libration amplitude. About 70 percent of the $\sim$2600 particles launched get trapped in these resonances. The rest collide with the moon.

again with two peaks. Figure 4.17 (right) depicts the co-rotation resonance argument. This second possibility implies that most of the particles are constrained by the co-rotation resonance as well. We caution the reader to not infer much from the precise shapes of the distribution; as they may not be statistically significant. Nevertheless, our simulations demonstrate conclusively that the debris launched from Anthe and Methone are constrained by the same resonances that affect the dynamics of the moons.

We can explain the bimodal nature of these distributions. Since every particle is launched with some extra speed, its initial condition is slightly different from that of the moon's. So we see particles slightly away from the moon's amplitude. The two peaks correspond to the particles which start from the leading and trailing halves of the moon and hence undergo a slow-down and a speed-up, respectively while they escape the moon. Moreover, the double peaked nature is further facilitated by the fact that the moon removes particles from its path while librating, so particles with amplitude similar to that of the moon get swept up [Tiscareno and

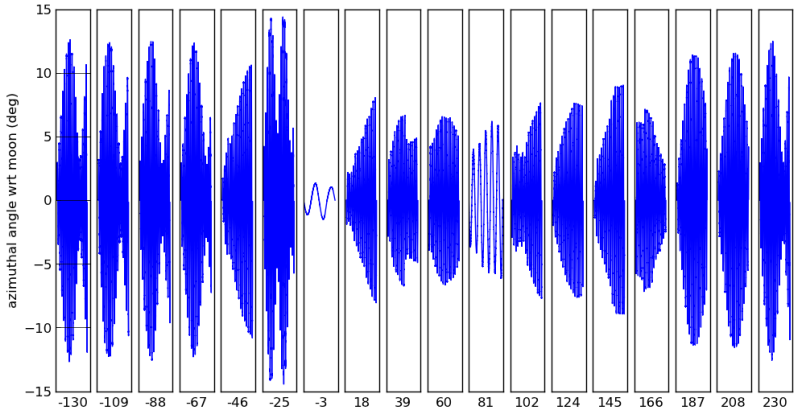

Figure 4.18: Effect of launches at different longitudes from Methone's surface: each box shows the variation of azimuthal positions of a particle (with respect to the moon) vs time (first few orbits) in the frame fixed at Methone. These particles are launched from near Methone's equator at different longitudes. The angles on the lower horizontal axis are in degrees and correspond to starting from the leading side of the moon if they lie between 0^o and 180^o, otherwise they start from the trailing side. The leading side loses energy and hence its amplitude is less than that of the trailing side particles.

Malhotra, 2009]. Figure 4.18 shows the different amplitudes for different launch longitudes. We see these corresponding groups as two peaks around the moon in Fig. 4.17. The story for Anthe is similar.

Figures 4.19 and 4.20 show the amplitudes of the resonance argument displayed vs the initial launch velocity with respect to the parent moon. Interestingly, Methone's resonance holds onto 70% of the particles while Anthe's resonance has only 50% of the particles constrained. Apart from the bimodal nature (as explained before), the amplitudes of the resonance arguments do not depend significantly on initial launch speed; this could be attributed to the loss of initial conditions which occur during the first few close encounters with the moon, because all particles start from the surface of the moon. Notice that particles near amplitude 180^0 are on the verge of circulation and they also do not show any dependence on the initial

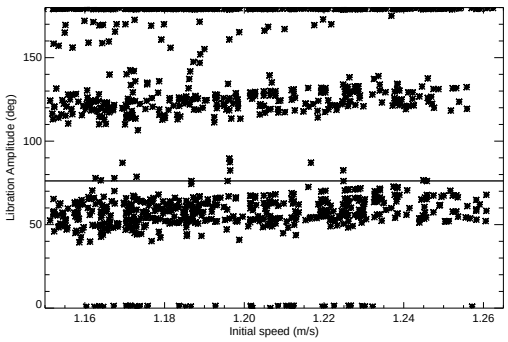

Figure 4.19: Distribution of the libration amplitude of the resonance arguments ($\phi = 11\lambda_{Par} - 10\lambda_{Mimas} - \varpi_{Mimas}$) of particles (subscript-Par) near Anthe vs initial launch speed relative to Anthe after 23 years of integration. The horizontal line shows Anthe's amplitude.

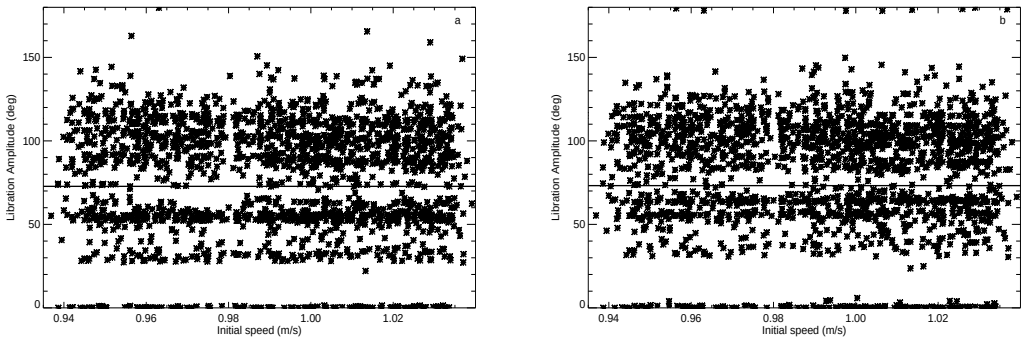

Figure 4.20: Distribution of the amplitude in the resonance argument ((a) $\phi = 15\lambda_{Par} - 14\lambda_{Mimas} - \varpi_{par}$ (b) $\phi = 15\lambda_{Par} - 14\lambda_{Mimas} - \varpi_{Mimas}$) of particles (subscript-Par) near Methone vs initial launch speed relative to Methone after 23 years of integration. The horizontal lines depict Methone's amplitude.

relative velocity. The energies set by the first close encounter with the moons fix their initial conditions; that later determines the particle's fate, unless the initial launch velocities are high enough as to be little perturbed by the moon.

Pallene's 'near'-resonance is third-order, and hence much weaker than the others which are first-order. In the absence of any resonant confinement, Pallene's ring will differentially precess by 360^o under Saturn's oblate gravity field and become axially symmetric. This will happen over an interval $t = \frac{2\pi}{\triangle\dot{\Omega}}$ (see Chapter 3) where

$$\frac{\triangle\dot{\Omega}}{\dot{\Omega}} = -\frac{7}{2}\frac{\triangle a_P}{a_P}, \tag{4.5}$$

which is $\sim$ 1000 yrs, using $\dot{\Omega} = 5.423$ rad/yr. Similarly, the re-collision time (time for a particle to collide with the moon) is 10^5 years [Hamilton and Burns, 1994, Bierhaus et al., 2012], using a calculation similar to that for the E-ring particles to collide with Enceladus (Ch. 2). These two times along with the fact that the ring is observed to be inclined could mean that the ring was generated recently. The very long time of collision and much smaller speeds rules out the possibility that the particles are getting replenished by self-collision to maintain an inclined ring [Hamilton and Burns, 1994]. The precessional shearing time of $\sim$ 1000 years, hence, suggests that the particles are most probably very young.

We can further show that inclination of Pallene's particles in its ring have little effect from the 'near'-resonance with Enceladus. Figure 4.21 shows the relative longitudes of nodes, $\Omega_{Particle} - \Omega_{Pallene}$, plotted versus time. The top of the plot shows the case in the presence of Enceladus and the lower without the moon. Though there is a drift in the lower figure, the relative drift of the particle-clowd is same in both the cases ($\sim 6^o$ in 23 years). Clearly, Enceladus 'near'-resonance has

little effect in restraining the ring from drifting and becoming radially symmetric (in short intervals). Note that the drift $\dot{\Omega}$ is $\sim 0.2^o/$ yr (as read from the top of Fig. 4.21). This would make the ring axially symmetric in 1200 years, which is similar to the rate Saturn's oblateness spreads the ring (calculated as ~ 1000 yr). Hence, the 'near'-resonance with Enceladus cannot keep the particles constrained near Pallene (unlike in the case of Anthe and Methone) and the ring probably is recently made. Recall that Anthe and Methone are fully librating in their respective resonances, while Pallene is not (Section 4.3). Since the arc and ring particles are in similar resonances, as shown, this explains why the Anthe and Methone ejecta remain constrained in arcs while Pallene's do not.

4.5.2 Strength of resonances

To further verify the existence of these resonances and to test the theory of the formation and confinement of arcs, in one simulation we started particles uniformly all along the orbits of Anthe and Methone. The particle velocities were close to the orbital velocity so that particles do not escape the resonant arcs immediately. They were given velocities uniformly varying between v_{esc} to $1.1v_{esc}$. Figures 4.22 and 4.23 show that the particles settle down and populate many lobes (as seen from frames rotating with the mean motions of the respective moons). This clearly shows the effect of resonance on particles lying in the moon's orbit. It also shows that particles in the current arcs of these two moons have energies similar to that of the parent moon and likely come from the parent moon itself. Notice that these arcs are not in equilibrium (instead they are librating) and hence show different

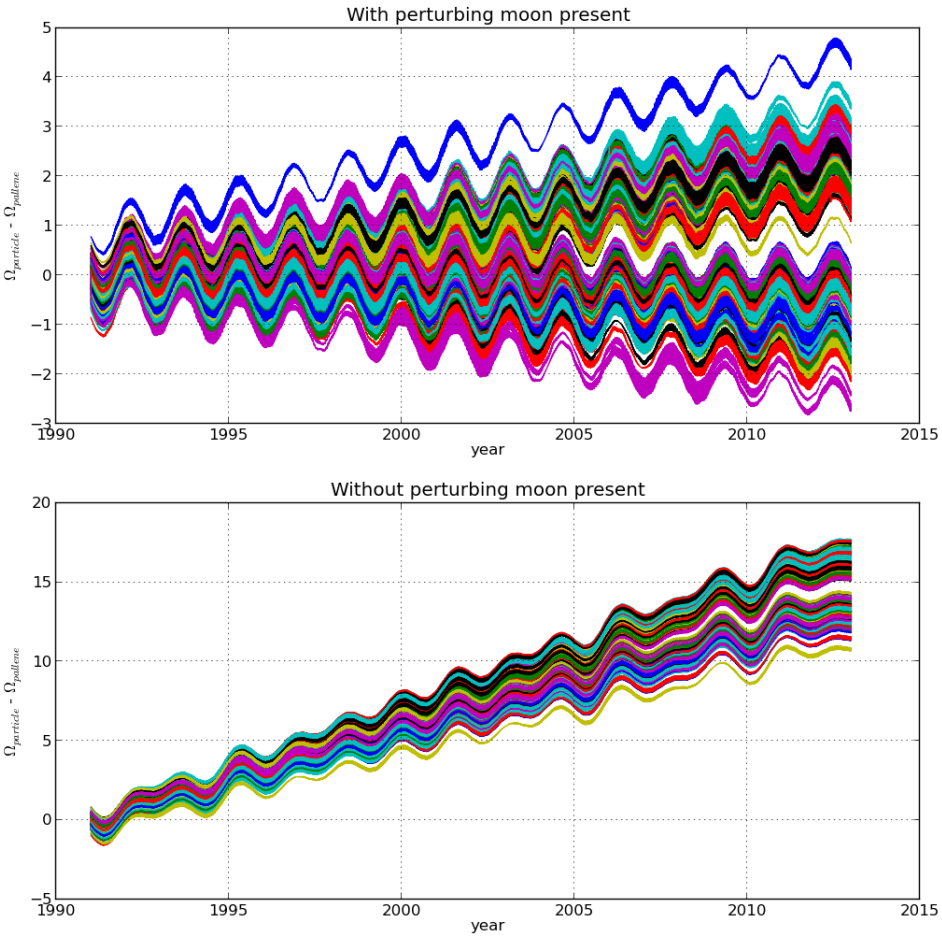

Figure 4.21: Top: with Enceladus' presence; Bottom: without Enceldaus' presence. The longitude of nodes of 324 Pallene's ring particles with respect to Pallene's orbit plotted versus time. The presence of Enceladus clearly limits the relative node drift.

sizes and concentrations. Also, since the moon is present in only one of these arcs, particles in other arcs do not get phase-mixed and hence show concentrations in a particular phase. We do not intend to discuss the dynamics of the particles in the different arcs in detail here, but this simple experiment shows that the resonance is stable and the arc in observations is indeed a result of the resonance.

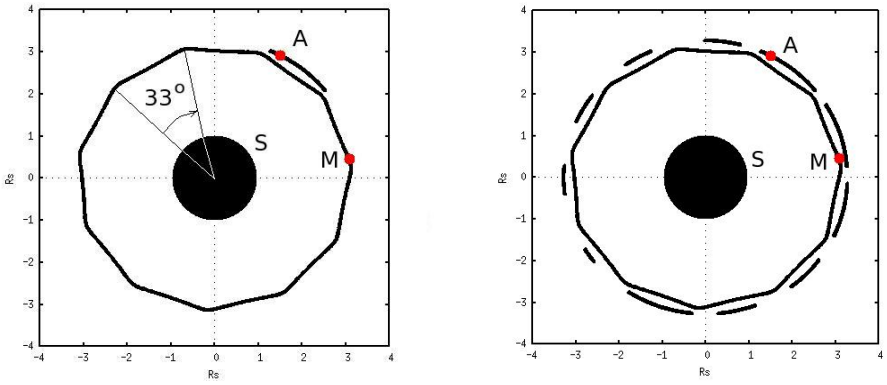

Figure 4.22: (a) A simulation (starting particles from Anthe's surface and then integrated for 23 yrs) shows particles that are trapped in one of the lobes of the 11:10 co-rotation resonances. (b) A simulation (starting particles all around the moon's orbit integrated for 23 yrs) shows that the particles are trapped in the different lobes of the 11:10 co-rotation resonance. These arcs are not in equilibrium (they are librating) and hence have variable lengths. The frames in both the cases rotate with an angular speed of 347.35 ^{o}/day, the mean motion of Anthe. M stands for Mimas, A identifies Anthe and S locates Saturn. The unit of length is R_S.

The longitudinal extent of Anthe's arc is consistent in terms of observations and calculations. A 11:10 resonance produces 11 evenly-spaced stable spots about which the material can be trapped (Fig. 4.22). Particles librating around these stable points therefore can form an arc having at most an extent of $360^o/11 = 33^o$. The arc associated with Anthe is observed to be 20^o long [Hedman et al., 2009a], and hence is within the limits. Our simulations also generated arcs of longitudinal length $\sim 10^o$ (Fig. 4.12), well within the theoretical limits. Similarly, the 15:14 co-rotational eccentricity resonance of Methone's arc particles with Mimas can be

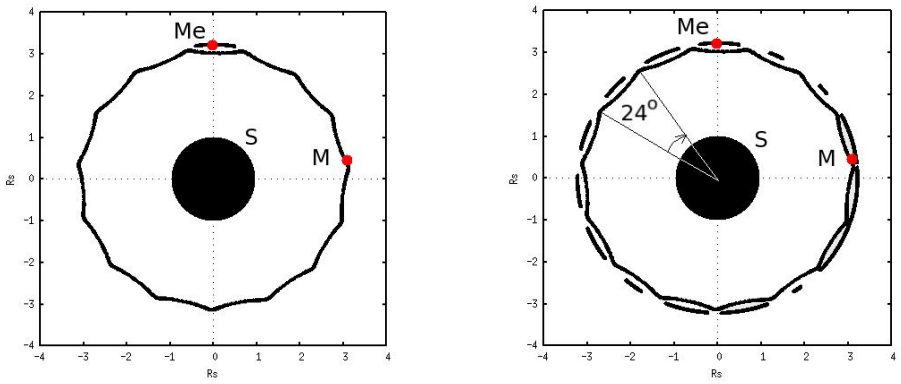

Figure 4.23: (a) A simulation (starting particles from Methone's surface integrated for 23 years) shows that particles are trapped in one of the lobes of the 15:14 co-rotation and Lindblad resonance. (b) A simulation (starting particles all around the moon's orbit and then integrated for 23 years) shows particles that are trapped in different lobes of the 15:14 co-rotation and Lindbad resonances. These arcs are not in equilibrium (librating instead) and hence have variable lengths. The frame in both the cases is rotating with an angular speed of 356.59 ^{o}/day, the mean motion of Methone. M stands for Mimas, Me identifies Methone and S locates Saturn. The unit of length is R_S.

explained. The longitudinal extent of the Methone-arc (Fig. 4.23) is observed to be 10^o [Hedman et al., 2009a], significantly lower than the maximum possible $360^o/15 = 24^o$. Our simulated numbers were also $\sim 10^o$ (Fig. 4.13).

To estimate the velocity required to escape from the resonance, we experimented by launching particles with various speeds from the moon's equator. We illustrate Anthe's case here: Figure 4.24 shows the resonance argument plotted versus time. With lower starting speeds (1-2 m/s), particles remain confined and librate around the stable center. If the velocity increases to 3 m/s, particles still oscillate but with much higher amplitudes and longer periods. Velocities above 3 m/s leave the stable lobe and circulate, being no longer confined within the original resonance lobe. This justifies the choice of our initial speed range of (1 - 1.1)v_{esc} as a reasonable value in which most of the particles would be retained near the moon.

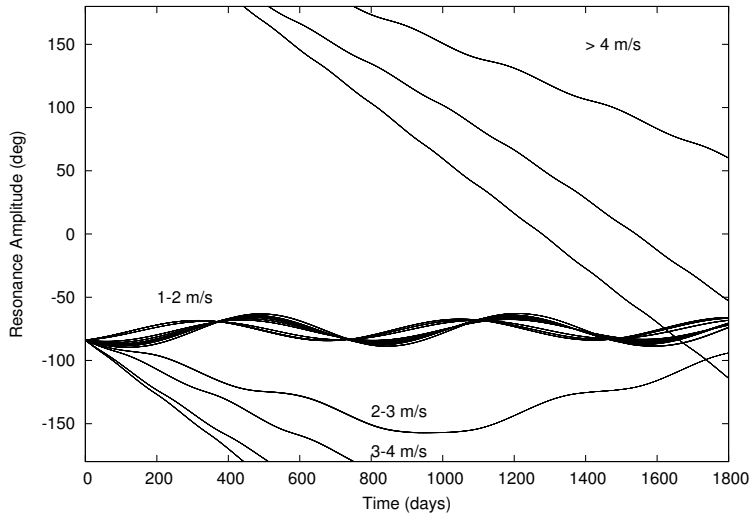

Figure 4.24: Particles in Anthe's arc remain trapped in resonances similar to those that trap Anthe. Some of those with higher relative velocities go into circulation. The plot shows the resonance amplitude of some of Anthe's particles versus time (in days). Particles with velocities 1-2 m/s remain confine around Anthe. The critical velocity of breaking out of resonance is of the order of $2 - 3$ m/s.

The pendulum approximation [Murray and Dermott, 1999], as described in the previous chapter, permits estimates for the libration frequencies and widths, which can be compared against the observed and numerically generated values. The observed libration period (as calculated from the orbits of moons obtained from kernels) of the co-rotation resonance of Methone-Mimas is 550 days while the calculated value is 460 days (Ch. 3). For the Lindblad resonance, again, the observed value is 550 days and the calculated one is 460 days (Ch. 3). Similarly the calculated libration period for Anthe's co-rotation resonance is $\sim$ 720 days against the observed period of $\sim$ 700 days. The libration width for Methone-Mimas resonances is 36 km for the co-rotation case and 2.5 km for the Lindblad case (Chapter 3). Clearly, the co-rotation resonance in Methone-Mimas case is more stable. The libration width for Anthe's co-rotation resonance was calculated to be $\sim$ 36 km.

We can also calculate of the time for the arcs to spread by 360^o due to their

differential precession. The observed radial extent is 50-200 km for Anthe's arc. Using the expressions similar to those of Pallene's, we get a spreading time of 1-4 years. We showed in the simulations that the arc is maintained for at least 23 years. This implies that the particles are constrained. Similarly, for Methone's case, the observed radial extent is 50-200 km and the calculated spreading time is 1-4 years (Ch. 3). Again the resonance is powerful enough to restrain the particles.

4.6 Comments on non-gravitational forces

Apart from gravity, radiation pressure and electromagnetic forces should play significant roles in the evolution of dust particles in Saturnian system. They become important for small (~ 1 μm) particles [Burns et al., 2001].

Table 4.4 shows the accelerations produced by different forces on a 1-micron-sized particle, to make a quick comparison. The table makes it clear that gravity is the prime-mover in the ring dynamics. Oblateness, electromagnetic and radiation forces (to a lesser extent) become important in any longer time-scale analysis. These forces strongly depend on the size of the particles. Tidal forces due to any nearby moons are negligible. The variation of acceleration produced with respect to the radius can be seen in Fig. 4.25. We will concentrate on the region from $3R_S$ to $4R_S$.

Let us now compare the effect of electromagnetic forces on the particles of micron size near the orbits of the three moons. Following Hamilton [1993] and Schaffer and Burns [1992] for the axisymmetric case, the effect of electromagnetic forces

Force Type	**Expression**	**acceleration (m/s^2)**
Point-mass gravity	$\frac{GM}{r^2}$	0.67
Oblateness	$\frac{GM}{r^2} J_2 \left(\frac{R_S}{r}\right)^2$	6.9×10^{-4}
Electromagnetic	$\frac{qB}{m}(v + r\omega)$	1.3×10^{-4}
Radiation	$\frac{3J_0 Q_{Pr}}{4\rho c d_s^2 r_g}$	1.8×10^{-5}
Tidal (due to Dione)	$\frac{2GM_{Dio}\triangle r}{R^3}$	2.6×10^{-7}

Table 4.4: Accelerations produced by different forces on a micron-sized particle in Saturn's rings at a radial distance of $4R_S$. q is the charge on particle ($\sim 5 \times 10^{-16}$ C, maximum possible charge on a 1-micron radius sphere using an electromagnetic potential of -5 Volts [Hamilton, 1993]), B is Saturn's magnetic field at a distance r (3.6×10^{-7} Tesla), m is the mass of a 1-micron radius spherical particle (10^{-14} kg), v is Enceladus' orbital velocity, ω is Saturn's spin ($\sim 10^{-4}$ rad/sec), J_0 is the solar radiation flux at 1 AU from sun(1.36×10^3 J/m^2/sec), Q_{P_r} is the non-dimensional radiation pressure coefficient (~ 1), ρ is the particle's density (assumed to be 1000 kg/m^3), c is the speed of light ($\sim 3 \times 10^8$ m/s), d_s is 9.6 (Saturn's distance in AU), r_g is the particle's radius (1 micron), M_{Dio} is Dione's mass, $\triangle r$ is the radial distance between Dione's and Enceladus' orbits (10^8 m) and R is the semi-major axis of Dione's orbit (3.77×10^8 m) . Notice that the electromagnetic and radiation forces strongly depend on the size of the particles. For references to the numbers, see Horanyi et al. [1992].

averaged over an orbit are

$$\left\langle \frac{da}{dt} \right\rangle = 0 \tag{4.6}$$

and

$$\left\langle \frac{de}{dt} \right\rangle = -\frac{n}{4} \frac{q g_{1,0} R_p^3 \Omega_p}{c \mu m_g} e\sqrt{1-e^2} sin^2 i \times sin(2\omega) \tag{4.7}$$

where the variables (in SI units) are, angular orbital speed n is $\frac{2\pi}{T \times 24 \times 3600}$ rad/sec, where T is particle's orbital period in days, charge on particle $q = 5 \times 10^{-16}$ C (maximum charge on a 1 micron sized particle using a electromagnetic potential of -5 Volts), $g_{1,0} = +0.2154 \times 10^{-4}$ magnetic field coefficient with units of gauss, $R_p = 6.0330 \times 10^7$ m is radius of Saturn, $\Omega_p = 1.69 \times 10^{-4}$ rad/sec is the spin of Saturn, $c = 3 \times 10^8$ m/s is speed of light, $\mu = 3.794 \times 10^{16} Nm^2/kg$ and

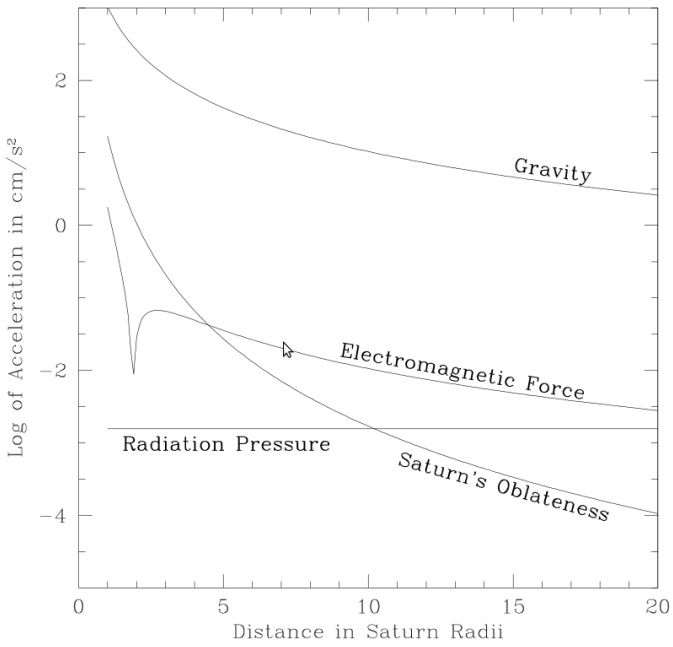

Figure 4.25: The strength of some perturbation forces around Saturn for a totally absorbing 1-μm dust grain charged to -5V. The electromagnetic force vanishes at synchronous orbit where the grain's velocity relative to the magnetic field is zero [Burns et al., 2001].

$m_g = 4.2 \times 10^{-15}$ kg is the mass of grain particle, assuming the particle to have radius 1 micron with density 1000 kg/m^3 [Hamilton, 1993].

Also the maximum radial distance, apocenter distance Q is (1+e)a, so the change of this maximum distance dQ is

$$dQ = (1 + e)da + ade = ade \tag{4.8}$$

Hence using the units given,

$$dQ = 7.78 \times 10^2 \times \frac{n}{4} \times ae\sqrt{1 - e^2}sin^2 i \times sin(2\omega)dt \tag{4.9}$$

Table 4.5 lists this distance (dQ) for the prescribed time period of evolution (t), where $sin(2\omega)$ is taken to be 1 for the maximum effect. Clearly, for small particles electromagnetic forces become important.

Moon	a (R_S)	e	i (deg)	T (days)	t	dQ (km)
Methone	3.22	0.0001	0.007	1.010	25 yr	2.15
Anthe	3.28	0.001	0.1	1.037	25 yr	4.36×10^3
Pallene	3.52	0.004	0.181	1.154	25 yr	5.51×10^4
Enceladus	3.95	0.0045	0.02	1.370	300 yr	8.55×10^4

Table 4.5: Orbital properties of moons and the maximum radial distance a charged particle moves due to electromagnetic forces.

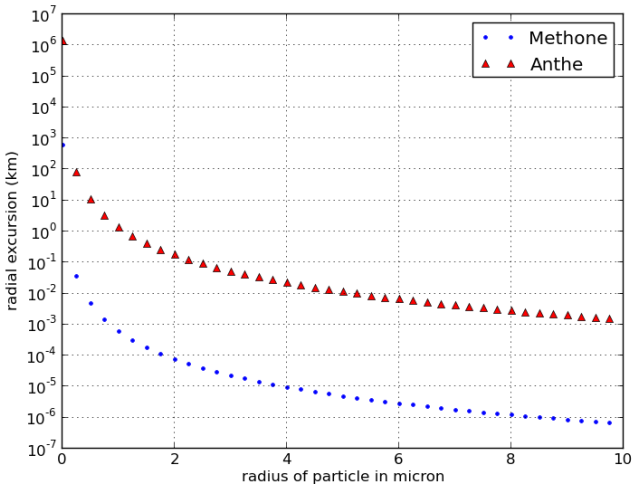

Figure 4.26: Maximum possible radial excursion of particles (dQ) for a given time period (t) near Methone's orbit with varying size. For reference to the numbers see table 4.3.

The primary effect of the electromagnetic force is to change the orbital precession rate of the particles [Horanyi et al., 1992]. For non-zero inclinations, it is a cyclic function of the argument of pericenter (ω), which should have a time average of zero for an orbiting particle. More importantly these effects are critically dependent on the particle's size (Fig. 4.26) as well as the charge and potential on the grains. We also notice from our simulations that gravitation alone results in the formation and confinement of the arcs. We, therefore, propose that the effect of non-gravitational forces is minimal in the formation of these arcs and ring. Also, notice that the effect of electromagnetic forces on radial excursions will be negligible for particles greater than 10 μm in radius.

4.7 Conclusions

Based on our numerical experiments,

1) Material leaving Methone and Anthe at low speeds ($<$ 1-2 m/s) remains confined in arcs surrounding the moons.

2) Anthe lies in the 11:10 first-order co-rotation resonance with Mimas [Cooper et al., 2008], and particles launched at low speeds from Anthe reside in the same resonance lobe (forming an arc), with varying amplitudes and libration periods of around 2 - 2.5 years, comparable to that of Anthe itself.

3) Methone resides in a 15:14 first-order co-rotation resonance [Spitale et al., 2006] as well as a Lindblad resonance with Mimas [Hedman et al., 2009a]. Particles launched at lower speeds from Methone are also trapped in both types of reso-

nances. The libration periods in this case are 1.5 - 2 years.

4) The third-order mixed resonance of Pallene particles with Enceladus is too weak to confine them in longitude so material from Pallene is free to spread out and form a complete ring. Particle lifetimes must be too short to allow sufficient time (1000 years) for the longitudes of node to spread out.

CHAPTER 5

FUTURE WORK

In this thesis we have investigated two topics related to the faint rings of Saturn: the spatial motion of particles in the E ring and the arcs/ring associated with Anthe, Methone and Pallene. Here are some possible extensions of this research to answer additional questions:

- *Further distinguish the role of different non-gravitational forces on the E-ring's structure*: Our analysis was focused on crediting gravitational forces as the primary reason for the double-layered structure of the E ring and the radial Gaussian halo (Ch. 2). However, there are non-gravitational forces like electromagnetic and radiation drag which play a crucial role in the evolution of this ring (where the radii of particles are smaller than 1-micron). These different forces have separate time scales for their dynamics and one can further explore their individual roles. In longer-term simulations of these rings, their role cannot be ignored and any long-term model need to include their influence. Understanding the role of each force separately in the structure and dynamics of the E-ring will be both interesting and useful to further our understanding of the E ring.
- *Consider other processes responsible for the loss of particles from the E ring*: The sole sink of particles in our simulations was collisions with the moon Enceladus itself. We removed any particles from the simulation that collided with the moon. In reality there will be losses out of the system due to various reasons. First of all, the particles can break up and change their character during their orbit [Hedman et al., 2011]. Moreover, in very long-term evolutions, various non-gravitational forces can probably make the particles diffuse

further away and leave the E-ring region. There can also be loss of particles by sputtering [Alvarellos et al., 2005]. Exploration of these possibilities can further enrich our E-ring model.

- *Further and longer-term analysis of the Anthe and Methone arcs and Pallene's ring*: Our simulations only evolve the arcs/rings for 23 years, the time for which the NASA orbital kernels were available. A longer-term analysis of this system can throw further light on the eventual fate and dynamics of these ultra-faint arcs and rings. Such an analysis is important if we are to consider whether our current, short-term study is relevant to the observed rings which presumably contain constituents that are older than twenty three years. It would also corroborate the resonances we have described in this thesis. In longer-term simulations, non-gravitational forces would have to be taken into account.

- *Answer why Pallene's ring is inclined in the first place*: In this thesis we have suggested how the inclination of Pallene's ring might be maintained. But it is a very curious fact that Pallene's orbit is inclined in first place. Understanding Pallene's inclination and hence its ring along through a longer integration can further throw light on this question.

- *Trace the origin of particles in faint arcs/rings*: We have proposed that the particles in the arcs/rings originate from their respective moons. We assumed them to have been started all over the surface of these moons. It would be interesting to further investigate the origin of these particles and if there is a directional bias according to their point of origin.

BIBLIOGRAPHY

C. H. Acton. Ancillary data services of NASA's Navigation and Ancillary Information Facility. *Planetary and Space Science*, 44:65–70, 1996.

M. Agarwal, S. Sarangi, and R. Bhattacharyya. Effect of Stress-softening on Dynamics of Loaded Rubber Shear Mountings. *Kharagpur Allied*, February:287–294, 2005.

Manish Agarwal. Effect of stress-softening on dynamics of a mass on rubber shear mountings. Master's thesis, Department of Mechanical Engineering, IIT Kharagpur, India, 2004.

Manish Agarwal and Soumitro Banerjee. Dynamics of a Mass on Moving Belt with Dry Friction. *National Conference on nonlinear systems and dynamics*, February:1–4, 2005.

J. L. Alvarellos, K. J. Zahnle, A. R. Dobrovolskis, and P. Hamill. Fates of satellite ejecta in the Saturn system. *Icarus*, 178:104–123, 2005.

W. A. Baum, T. Kreidl, J. A. Westphal, G. E. Danielson, P. K. Seidelmann, D. Pascu, and D. G. Currie. Saturn's E ring. I. CCD observations of March 1980. *Icarus*, 47:84–96, 1981.

K. Beurle, C. D. Murray, G. A. Williams, M. W. Evans, N. J. Cooper, and C. B. Agnor. Direct evidence for gravitational instability and moonlet formation in Saturn's rings. *The Astrophysical Journal*, 718, Issue 2:176–180, 2010.

E. B. Bierhaus, L. Dones, J. L. Alvarellos, and K. Zahnle. The role of ejecta in the small crater populations on the mid-sized saturnian satellites. *Icarus*, 218: 602–621, 2012.

N. Borderies and P. Goldreich. The variations in eccentricity and apse precession rate of a narrow ring perturbed by a close satellite. *Icarus*, 53, Issue 1:84–89, 1983.

R. H. Brown, R. N. Clark, B. J. Buratti, D. P. Cruikshank, J. W. Barnes, R. M. E. Mastrapa, J. Bauer, S. Newman, T. Momary, K. H. Baines, G. Bellucci, F. Capaccioni, P. Cerroni, M. Combes, A. Coradini, P. Drossart, V. Formisano, R. Jaumann, Y. Langevin, D. L. Matson, T. B. McCord, R. M. Nelson, P. D. Nicholson, B. Sicardy, and C. Sotin. Composition and physical properties of Enceladus' surface. *Science*, 311:1425–1428, 2006.

J. A. Burns. Elementary derivation of the perturbation equations of celestial mechanics. *American Journal of Physics*, 44:944–949, 1976.

J. A. Burns and B. J. Gladman. Dynamically depleted zones for Cassini's safe passage beyond Saturn's rings. *Planetary and Space Science*, 46, Issues 9-10: 1401–1407, 1998.

J. A. Burns, M. R. Showalter, J. N. Cuzzi, and J. B. Pollack. Physical processes in Jupiter's ring - clues to its origin by Jove. *Icarus*, 44:339–360, 1980.

J. A. Burns, M. R. Showalter, and G. E. Morfill. The ethereal rings of Jupiter and Saturn. In R. Greenberg and A. Brahic, editors, *IAU Colloq. 75: Planetary Rings*, pages 200–272, 1984.

J. A. Burns, D. P. Hamilton, F. Mignard, and S. Soter. The contamination of Iapetus by Phoebe dust. *IAU Colloq. 150: Physics, chemistry, and dynamics of interplanetary dust*, 104:179–182, 1996.

J. A. Burns, M. R. Showalter, D. P. Hamilton, P. D. Nicholson, I. de Pater, M. E.

Ockert-Bell, and P. C. Thomas. The Formation of Jupiter's Faint Rings. *Science*, 284:1146–1150, 1999.

J. A. Burns, D. P. Hamilton, and M. R. Showalter. Dusty rings and circumplanetary dust: Observations and simple physics. *Interplanetary Dust*, Springer-Verlag, Berlin:641–725, 2001.

N. Callegari. Resonant dynamics of small satellites in the inner system of Saturn. *AAS Division of Dynamical Astronomy meeting*, Paraty, Brazil, May:204.07, 2013.

S. Charnoz. Physical collisions of moonlets and clumps with the Saturn's F-ring core. *Icarus*, 201:191–197, 2009.

S. Charnoz, C. C. Porco, E. Déau, A. Brahic, J. N. Spitale, G. Bacques, and K. Baillie. Cassini discovers a kinematic spiral ring around Saturn. *Science*, 310:1300–1304, 2005.

J. E. Colwell, P. D. Nicholson, M. S. Tiscareno, C. D. Murray, R. G. French, and E. A. Marouf. The structure of Saturn's rings. *Saturn from Cassini-Huygens*, pages 375–412, 2009.

N. J. Cooper, C. D. Murray, M. W. Evans, K. Beurle, R. A. Jacobson, and C. C. Porco. Astrometry and dynamics of Anthe (S/2007 S 4), a new satellite of Saturn. *Icarus*, 195:765–777, 2008.

I. de Pater, S. G. Gibbard, E. Chiang, H. B. Hammel, B. Macintosh, F. Marchis, S. C. Martin, H. G. Roe, and M. Showalter. The dynamic neptunian ring arcs: Evidence for a gradual disappearance of Liberté and resonant jump of Courage. , 174:263–272, 2005.

S. F. Dermott. The 'braided' F-ring of Saturn. *Nature*, 290:454–457, 1981.

A. R. Dobrovolskis and J. A. Burns. Life near the Roche limit - Behavior of ejecta from satellites close to planets. *Icarus*, 42:422–441, 1980.

M. K. Dougherty, K. K. Khurana, F. M. Neubauer, C. T. Russell, J. Saur, J. S. Leisner, and M. E. Burton. Identification of a dynamic atmosphere at Enceladus with the Cassini magnetometer. *Science*, 311:1406–1409, 2006.

M. K. Dougherty, L. W. Esposito, and S. M. Krimigis. *Saturn from Cassini-Huygens*. 2009.

T. Gehrels, L. R. Baker, E. Beshore, C. Blenman, J. J. Burke, N. D. Castillo, B. Dacosta, J. Degewij, L. R. Doose, J. W. Fountain, J. Gotobed, C. E. Kenknight, R. Kingston, G. McLaughlin, R. McMillan, R. Murphy, P. H. Smith, C. P. Stoll, R. N. Strickland, M. G. Tomasko, M. P. Wijesinghe, D. L. Coffeen, and L. W. Esposito. Imaging photopolarimeter on Pioneer Saturn. *Science*, 207:434–439, 1980.

B. J. Gladman, J. A. Burns, M. Duncan, P. Lee, and H. F. Levison. The exchange of impact ejecta between terrestrial planets. *Science*, 271:1387–1392, 1996.

P. Goldreich, S. Tremaine, and N. Borderies. Towards a theory for Neptune's arc rings. *The Astronomical Journal*, 92:490–494, 1986.

D. P. Hamilton. Motion of dust in a planetary magnetosphere - Orbit-averaged equations for oblateness, electromagnetic, and radiation forces with application to Saturn's E ring. *Icarus*, 101 (no. 2):244–264, 1993.

D. P. Hamilton and J. A. Burns. Origin of Saturn's E ring: Self-sustained, naturally. *Science*, 264:550–553, 1994.

J. Hanninen and C. Porco. Collisional simulations of Neptune's ring arcs. *Icarus*, 126:1–27, 1997.

M. M. Hedman, J. A. Burns, M. R. Showalter, C. C. Porco, P. D. Nicholson, A. S. Bosh, M. S. Tiscareno, R. H. Brown, B. J. Buratti, K. H. Baines, and R. Clark. Saturn's dynamic D ring. *Icarus*, 188:89–107, 2007a.

M. M. Hedman, J. A. Burns, M. S. Tiscareno, C. C. Porco, G. H. Jones, E. Roussos, N. Krupp, C. Paranicas, and S. Kempf. The source of Saturn's G ring. *Science*, 317:653–656, 2007b.

M. M. Hedman, C. D. Murray, N. J. Cooper, M. S. Tiscareno, K. Beurle, M. W. Evans, and J. A. Burns. Three tenuous rings/arcs for three tiny moons. *Icarus*, 199:378–386, 2009a.

M. M. Hedman, P. D. Nicholson, M. R. Showalter, R. H. Brown, B. J. Buratti, and R. N. Clark. Spectral observations of the Enceladus plume with Cassini-VIMS. *The Astrophysical Journal*, 693:1749–1762, 2009b.

M. M. Hedman, N. J. Cooper, C. D. Murray, K. Beurle, M. W. Evans, M. S. Tiscareno, and J. A. Burns. Aegaeon (Saturn LIII), a G-ring object. *Icarus*, 207:433–447, 2010.

M. M. Hedman, J. A. Burns, M. W. Evans, M. S. Tiscareno, and C. C. Porco. Saturn's curiously corrugated C ring. *Science*, 332:708–711, 2011.

M. M. Hedman, J. A. Burns, D. P. Hamilton, and M. R. Showalter. The three-dimensional structure of Saturn's E ring. *Icarus*, 217:322–338, 2012.

M. Horanyi and C. C. Porco. Where exactly are the arcs of Neptune? *Icarus*, 106: 525–535, 1993.

M. Horanyi, J. A. Burns, and D. P. Hamilton. The dynamics of Saturn's E ring particles. *Icarus*, 97:248–259, 1992.

M. Horányi, A. Juhász, and G. E. Morfill. Large-scale structure of Saturn's E-ring. *Geophysical Research Letters*, 35:L04203, 5, 2008.

M. Horányi, J. A. Burns, M. M. Hedman, G. H. Jones, and S. Kempf. Saturn's diffuse rings. *Saturn from Cassini-Huygens*, Eds. M. Dougherty, L. Esposito, and T. Krimigis. Springer:511–536, 2009.

A. P. Ingersoll and S. P. Ewald. Total particulate mass in Enceladus plumes and mass of Saturn's E ring inferred from Cassini ISS images. *Icarus*, 216:492–506, 2011.

I. G. Izsak. Laplace Coefficients and Their Newcomb Derivatives. *SAO Special Report*, 129, July 1963.

R. A. Jacobson, P. G. Antreasian, J. J. Bordi, K. E. Criddle, R. Ionasescu, J. B. Jones, R. A. Mackenzie, M. C. Meek, D. Parcher, F. J. Pelletier, W. M. Owen, Jr., D. C. Roth, I. M. Roundhill, and J. R. Stauch. The gravity field of the Saturnian system from satellite observations and spacecraft tracking data. *The Astronomical Journal*, 132:2520–2526, 2006.

A. Juhász and M. Horányi. Saturn's E ring: A dynamical approach. *Journal of Geophysical Research (Space Physics)*, 107:1066–1076, 2002.

A. Juhász and M. Horányi. Seasonal variations in Saturn's E-ring. *Geophysical Research Letters*, 31:L19703,4, 2004.

J. E. Keeler. A spectroscopic proof of the meteoric constitution of Saturn's rings. *Astrophysical Journal*, 1:416–427, 1895.

S. Kempf, U. Beckmann, G. Moragas-Klostermeyer, F. Postberg, R. Srama, T. Economou, J. Schmidt, F. Spahn, and E. Grün. The E ring in the vicinity

of Enceladus. I. Spatial distribution and properties of the ring particles. *Icarus*, 193:420–437, 2008.

S. Kempf, U. Beckmann, and J. Schmidt. How the Enceladus dust plume feeds Saturn's E ring. *Icarus*, 206:446–457, 2010.

S. W. Kieffer, X. Lu, G. McFarquhar, and K. H. Wohletz. A redetermination of the ice/vapor ratio of Enceladus plumes: Implications for sublimation and the lack of a liquid water reservoir. *Icarus*, 203:238–241, 2009.

R. A. Kolvoord, J. A. Burns, and M. R. Showalter. Periodic features in Saturn's F ring - Evidence for nearby moonlets. *Nature*, 345:695–697, 1990.

S. M. Krimigis, D. G. Mitchell, D. C. Hamilton, N. Krupp, S. Livi, E. C. Roelof, J. Dandouras, T. P. Armstrong, B. H. Mauk, C. Paranicas, P. C. Brandt, S. Bolton, A. F. Cheng, T. Choo, G. Gloeckler, J. Hayes, K. C. Hsieh, W.-H. Ip, S. Jaskulek, E. P. Keath, E. Kirsch, M. Kusterer, A. Lagg, L. J. Lanzerotti, D. LaVallee, J. Manweiler, R. W. McEntire, W. Rasmuss, J. Saur, F. S. Turner, D. J. Williams, and J. Woch. Dynamics of Saturn's magnetosphere from MIMI during Cassini's orbital insertion. *Science*, 307:1270–1273, 2005.

W. S. Kurth, T. F. Averkamp, D. A. Gurnett, and Z. Wang. Cassini RPWS observations of dust in Saturn's E Ring. *Planetary and Space Sciene*, 54:988–998, 2006.

H. F. Levison and M. J. Duncan. The long-term dynamical behavior of short-period comets. *Icarus*, 108:18–36, 1994a.

H. F. Levison and M. J. Duncan. The long-term dynamical behavior of short-period comets. *Icarus*, 108:18–36, 1994b.

Yue Ma, Manish Agarwal, and Soumitro Banerjee. Border Collision Bifurcations in a Soft Impact System. *Physics Letters A*, 354 (No. 4):281–287, 2006.

J. C. Maxwell. On the stability of motions of Saturn's rings. *Monthly Notices of the Royal Astronomical Society*, 19:297–304, 1859.

C. D. Murray and S. F. Dermott. *Solar System Dynamics*. Cambridge University Press, New York, 1999.

C. D. Murray and S. M. Giuliatti-Winter. Periodic collisions between the moon Prometheus and Saturn's F ring. *Nature*, 380:139–141, 1996.

C. D. Murray, C. Chavez, K. Beurle, N. Cooper, M. W. Evans, J. A. Burns, and C. C. Porco. How Prometheus creates structure in Saturn's F ring. *Nature*, 437: 1326–1329, 2005.

C. D. Murray, K. Beurle, N. J. Cooper, M. W. Evans, G. A. Williams, and S. Charnoz. The determination of the structure of Saturn's F ring by nearby moonlets. *Nature*, 453:739–744, 2008.

F. Namouni and C. Porco. The confinement of Neptune's ring arcs by the moon Galatea. *Nature*, 417:45–47, 2002.

P. D. Nicholson, M. R. Showalter, L. Dones, R. G. French, S. M. Larson, J. J. Lissauer, C. A. McGhee, P. Seitzer, B. Sicardy, and G. E. Danielson. Observations of Saturn's ring-plane crossings in August and November 1995. *Science*, 272: 509–515, 1996.

M. E. Ockert-Bell, J. A. Burns, I. J. Daubar, P. C. Thomas, J. Veverka, M. J. S. Belton, and K. P. Klaasen. The Structure of Jupiter's Ring System as Revealed by the Galileo Imaging Experiment. , 138:188–213, April 1999.

C. C. Porco. An explanation for Neptune's ring arcs. *Science*, 253:995–1001, 1991.

C. C. Porco. S/2007 S 4. *IAU Circ. Edited by Green, D. W. E.*, 8857:2, 2007.

C. C. Porco, P. Helfenstein, P. C. Thomas, A. P. Ingersoll, J. Wisdom, R. West, G. Neukum, T. Denk, R. Wagner, T. Roatsch, S. Kieffer, E. Turtle, A. McEwen, T. V. Johnson, J. Rathbun, J. Veverka, D. Wilson, J. Perry, J. Spitale, A. Brahic, J. A. Burns, A. D. Del Genio, L. Dones, C. D. Murray, and S. Squyres. Cassini observes the active south pole of Enceladus. *Science*, 311:1393–1401, 2006.

F. Postberg, J. Schmidt, J. Hillier, S. Kempf, and R. Srama. A salt-water reservoir as the source of a compositionally stratified plume on Enceladus. *Nature*, 474: 620–622, 2011.

S. Renner and B. Sicardy. Use of the geometric elements in numerical simulations. *Celestial Mechanics and Dynamical Astronomy*, 94:237–248, 2006.

T. Roatsch, R. Jaumann, K. Stephan, and P. C. Thomas. *Cartographic mapping of the icy satellites using ISS and VIMS data*. 2009.

E. Roussos, G. H. Jones, N. Krupp, S. M. Krimigis, D. Mitchell, and C. Paranicas. R/2006 S 5. *IAU Circ. Edited by Green, D. W. E.*, 8773:3, 2006.

E. Roussos, G. H. Jones, N. Krupp, C. Paranicas, D. G. Mitchell, A. Lagg, J. Woch, U. Motschmann, S. M. Krimigis, and M. K. Dougherty. Electron microdiffusion in the Saturnian radiation belts: Cassini MIMI/LEMMS observations of energetic electron absorption by the icy moons. *Journal of Geophysical Research (Space Physics)*, 112(A11):A06214, 2007.

E. Roussos, G. H. Jones, N. Krupp, C. Paranicas, D. G. Mitchell, S. M. Krimigis, J. Woch, A. Lagg, and K. Khurana. Energetic electron signatures of Saturn's

smaller moons: Evidence of an arc of material at Methone. *Icarus*, 193:455–464, 2008.

L. Schaffer and J. A. Burns. Lorentz resonances and the vertical structure of dusty rings - Analytical and numerical results. , 96:65–84, 1992.

J. Schmidt, N. Brilliantov, F. Spahn, and S. Kempf. Slow dust in Enceladus' plume from condensation and wall collisions in tiger stripe fractures. *Nature*, 451:685–688, 2008.

M. R. Showalter. Saturn's D ring in the Voyager images. *Icarus*, 124:677–689, 1996.

M. R. Showalter and J. A. Burns. A numerical study of Saturn's F-ring. *Icarus*, 52:526–544, 1982.

M. R. Showalter, J. N. Cuzzi, and S. M. Larson. Structure and particle properties of Saturn's E ring. *Icarus*, 94:451–473, 1991.

B. Sicardy, F. Roddier, C. Roddier, E. Perozzi, J. E. Graves, O. Guyon, and M. J. Northcott. Images of Neptune's ring arcs obtained by a ground-based telescope. *Nature*, 400:731–733, 1999.

B. A. Smith, L. Soderblom, R. M. Batson, P. M. Bridges, J. L. Inge, H. Masursky, E. Shoemaker, R. F. Beebe, J. Boyce, G. Briggs, A. Bunker, S. A. Collins, C. Hansen, T. V. Johnson, J. L. Mitchell, R. J. Terrile, A. F. Cook, J. N. Cuzzi, J. B. Pollack, G. E. Danielson, A. P. Ingersoll, M. E. Davies, G. E. Hunt, D. Morrison, T. Owen, C. Sagan, J. Veverka, R. Strom, and V. E. Suomi. A new look at the Saturn system - The Voyager 2 images. *Science*, 215:504–537, 1982.

J. N. Spitale and C. C. Porco. Association of the jets of Enceladus with the warmest regions on its south-polar fractures. *Nature*, 449:695–697, 2007.

J. N. Spitale, R. A. Jacobson, C. C. Porco, and W. M. Owen, Jr. The orbits of Saturn's small satellites derived from combined historic and Cassini imaging observations. *Astronomical Journal*, 132:692–710, 2006.

D. Tamayo, J. A. Burns, D. P. Hamilton, and M. M. Hedman. Finding the trigger to Iapetus' odd global albedo pattern: Dynamics of dust from Saturn's irregular satellites. *Icarus*, 215:260–278, 2011.

M. F. Thomsen and J. A. van Allen. Motion of trapped electrons and protons in Saturn's inner magnetosphere. *Journal of Geophysical Research*, 85:5831–5834, 1980.

M. S. Tiscareno and R. Malhotra. Chaotic diffusion of resonant Kuiper Belt objects. *Astronomical Journal*, 138:827–837, 2009.

J. A. van Allen. Absorption of energetic protons by Saturn's ring G. *Journal of Geophysical Research (Space Pyhsics)*, 88:6911–6918, 1983.

J. A. van Allen. An upper limit on the sizes of shepherding satellites at Saturn's ring G. *Journal of Geophysical Research (Space Physics)*, 92:1153–1159, 1987.

A. J. Verbiscer, M. F. Skrutskie, and D. P. Hamilton. Saturn's largest ring. *Nature*, 461:1098–1100, 2009.

G. A. Williams and C. D. Murray. Stability of co-orbital ring material with applications to the Janus-Epimetheus system. *Icarus*, 212:275–293, 2011.